

# ELECTRICALLY CONDUCTIVE HOLLOW FIBER MEMBRANE DEVELOPMENT

ELECTRICALLY CONDUCTIVE HOLLOW FIBER  
MEMBRANE DEVELOPMENT: ADDRESSING THE  
SCALABILITY CHALLENGES AND PERFORMANCE LIMITS  
OF CONDUCTIVE MEMBRANE FABRICATION

By

**MELISSA J. LAROCQUE, *B. Eng. Biosci***

McMaster University

Department of Chemical Engineering

A thesis submitted to the School of Graduate Studies in partial fulfillment of the requirements of  
McMaster University for the degree of Master of Applied Science

McMaster University

© Melissa J. Larocque, November 2020

**Master of Applied Science (2020)**

McMaster University

**(Chemical Engineering)**

Hamilton, Ontario

**Title:**

ELECTRICALLY CONDUCTIVE HOLLOW FIBER  
MEMBRANE DEVELOPMENT: ADDRESSING  
THE SCALABILITY CHALLENGES AND  
PERFORMANCE LIMITS OF CONDUCTIVE  
MEMBRANE FABRICATION

**Author:**

Melissa J. Larocque

**Supervisors:**

Dr. David Latulippe  
Dr. Charles-François de Lannoy

**Number of Pages:**

xx, 150

## **Lay Abstract**

Membrane separation technologies are a common purification strategy in many fields due to their simplicity and low energy requirements. Membranes operate by rejecting particles from feed water based on their chemical or physical properties such as size or charge. Long-term membrane operations are limited by fouling, incurring large operating costs for frequent cleaning cycles and downtime. Furthermore, traditional membrane separations only physically remove particles, presenting a risk for contaminant re-introduction into the environment. Electrically conductive membranes are an emerging strategy for addressing these concerns due to their demonstrated antifouling, enhanced selectivity, and redox capabilities. To date, these membranes have almost exclusively been developed as flat sheets with limited research into other membrane formats. Hollow fiber membranes resemble thin tubes ~1 mm in diameter and up to ~1 m in length where filtration occurs through the tubular wall of the fiber; the small diameter allows for hundreds of fibers to pack into an individual module, thus maximizing throughput. In this thesis, several issues with hollow fiber conductive membrane fabrication are addressed to ensure consistent performance along the length of the fiber. A key trade-off between membrane surface conductivity and throughput was found to exist universally in the conductive membrane field. This knowledge can be used to select fabrication methods and parameters to target certain performance ranges.

## Abstract

Electrically conductive membranes (ECMs) are of significant research interest for their ability to mitigate fouling, enhance separation capacity, and induce electrochemical degradation of contaminants. Most ECM development has been in flat sheet format suitable for laboratory studies; in industrial applications, formats such as hollow fiber (HF) are preferred for their high packing density. While ECMs in HF format are emerging in research, these techniques typically employ the same methods proven for flat sheet, often involving direct deposition of conductive material onto a support membrane with no further investigation into how the deposition process affects ECM properties. This is a significant challenge for long (~1 m) HF membranes where coating uniformity is essential to ensure consistent performance. The goal of this project was to fabricate conductive HF membranes, ensuring uniform performance along the fiber. In this work, we have developed a “crossflow deposition” technique to deposit a uniform layer of single walled/double walled carbon nanotubes (SW/DWCNTs) onto the interior surface of commercial polyether sulfone HF membranes. In a design-of-experiments model, feed pressure and crossflow velocity were shown to directly impact composite membrane conductivity and permeability. The highest permeability (~2900 LMH/bar) and conductivity (~670 S/m) were both achieved at the high pressure (0.2 bar) and high crossflow velocity (1.06 cm/s) condition. An inverse relationship was identified between conductivity and permeability for 29 different HF membranes coated under various flow and particle loading conditions. Similar trends were evident in ECM literature when comparing 80 membranes across 38 papers, covering various conductive materials, separation types, configurations, and applications. Metallic-based ECMs outperformed graphitic nanomaterial or conductive polymer-based ECMs with conductivities three orders of magnitude higher. This review also revealed a wide variation in performance testing with 35 unique pollutants

in 63 total tests, indicating a need for standardization to accurately compare ECMs and a need for testing with more realistic feed sources. Finally, electrochemical degradation of methyl orange using the CNT-coated HF membranes was evaluated in batch and continuous removal experiments. Although no significant MO removal was detected in either configuration, these modules can be used for further optimization in terms of targeted conductivity, contact time, and electrochemical parameters such as applied voltage. This work highlights the existence of a conductivity/ permeability trade-off in ECM development and how manipulation of flow parameters during deposition can impact this trade-off in HF membrane development.

## Acknowledgements

First and foremost, I would like to thank my supervisors Dr. David Latulippe and Dr. Charles-François de Lannoy for your support, guidance, and encouragement throughout my graduate career at McMaster University. Thank you Dr. Latulippe for seeing my potential in my second year of undergrad and giving me the chance to work in your lab. Your insight and constructive feedback over these past five years has helped me hone my skills as a researcher, ultimately culminating in this thesis project, and I am proud of the work we have accomplished together. Although I have only known Dr. de Lannoy the past two years, his dedication to his students and passion for research has been instrumental in shaping my research outlook and professional growth. Both of you have taught me the importance of thinking critically, being curious, and constantly striving for improvement, and I hope to carry these ideals with me for the rest of my career. I would also like to thank my third committee member, Dr. Alex Adronov, for lending me your advice and expertise these past two years. Throughout my undergraduate career at McMaster, I have had the privilege of learning from many dedicated and knowledgeable teachers. I would especially like to thank Dr. Carlos Filipe, Dr. Jake Nease, and Dr. Li Xi for your advice, commitment to education, and for providing me with many opportunities for technical, professional, and personal growth. It is professors like you that give McMaster's department of Chemical Engineering such an excellent reputation.

From the Chemical Engineering department, I would like to thank the hard-working administrative team, Kristina Trollip, Michelle Whalen, and Linda Ellis, for your assistance and patience with me no matter how many administrative questions I had! I would also like to thank Paul Gatt, Mike Clarke, Tim Stephens, and Doug Keller for your technical expertise and support. Special thanks to Paul who fabricated all custom modules used in this thesis project.

I would like to thank the staff at the Canadian Center for Electron Microscopy, especially Jhoynner Martinez, Andy Duft, and Chris Butcher, for their training and assistance with my microscopy analysis. I would also like to thank Dr. Ayse Turak in the Engineering Physics department for allowing us to use their conductivity measurement equipment.

Financial support was provided by the Natural Sciences and Engineering Research Council of Canada (NSERC) through the Canadian Graduate Scholarship – Master’s program and by the Province of Ontario through the Ontario Graduate Scholarship program.

I would like to thank my fellow lab-mates and friends in the Latulippe Lab, de Lannoy Lab, and Chemical Engineering department for your support and friendship: Ryan, Abhishek, Karina, Patrick, Evan, Amin, Cassandra, Alex, Dan, Nan, Mohamed, Hyejin, Yichen, Logan, and Alexandra. Our conversations, trivia nights, hikes, and sushi lunches were sometimes the only things keeping me sane throughout this process. I wish you all the best of luck in your future careers and hope we stay in touch! I would also like to thank the undergraduate students who worked with me the past two summers – Jasmine Kurtz and Adi Gelb. Thank you both for your hard work and I know you have bright futures ahead of you.

Finally, I would like to thank my parents, Guy and Cathy, and my sister Heather for your endless love and support throughout my academic career. This accomplishment would not have been possible without your constant encouragement and faith in me. Thank you, dad, for instilling a love of science in me at a young age. My parents have always taught my sister and I that with hard work and perseverance, the world can be your oyster. It is thanks to this attitude and the strength of my support network that I have reached this milestone.

# Table of Contents

Lay Abstract.....	iii
Abstract.....	iv
Acknowledgements.....	vi
Table of Contents.....	viii
List of Figures.....	xi
List of Tables.....	xvii
Abbreviations & Symbols.....	xviii
Declaration of Academic Achievement.....	xx
Chapter 1: Introduction.....	1
1.1 Membrane Technologies.....	1
1.1.1 Terminology & Classification.....	1
1.1.2 Challenges & Limitations.....	6
1.1.3 Current Trends in Membrane Development.....	8
1.2 Electrically Conductive Membranes.....	11
1.2.1 Benefits & Applications for Conductive Membranes.....	11
1.2.2 Materials & Methods for Fabrication.....	13
1.2.3 Geometry & Scale-up.....	14
1.3 Conductivity/ Permeability Trade-off.....	16
1.3.1 Limitations in Dead-end Conductive Membrane Fabrication.....	16
1.3.2 Potential for Crossflow Filtration – Application to Particle Deposition Theory....	17
1.4 Motivation & Objectives.....	20
1.5 References.....	21
Chapter 2: Formation of electrically conductive hollow fiber membranes via crossflow deposition of carbon nanotubes – addressing the conductivity/ permeability trade-off.....	29
2.1 Preface.....	29
2.2 Abstract.....	30
2.3 Introduction.....	31
2.4 Experimental.....	36
2.4.1 Materials.....	36
2.4.2 Carbon Nanotube Suspension Preparation.....	36
2.4.3 Crossflow Deposition Experiments.....	37
2.4.4 Surface Conductivity Analysis.....	42
2.4.5 Scanning Electron Microscopy (SEM).....	42
2.5 Results & Discussion.....	43

2.5.1	Optimization of the Crossflow Conditions for Depositing CNTs onto HF Membranes	43
2.5.2	Feed Concentration Effects on CNT-coated HF Membranes .....	54
2.5.3	Examination of the Conductivity/ Permeability Trade-off for CNT-coated HF membranes via a Robeson-Like Plot .....	57
2.6	Conclusions .....	61
2.7	References .....	62
2.8	Supplementary Information.....	67
Chapter 3: A universal method for evaluating electrically conductive membrane performance: comparative review of the conductivity/ permeability trade-off .....		
		75
3.1	Preface.....	75
3.2	Abstract .....	76
3.3	Introduction .....	77
3.4	Literature Review & Methodology .....	80
3.5	Comparing Electrically Conductive Membrane (ECM) Properties, Materials and Applications .....	81
3.5.1	Establishing the conductivity/ permeability trade-off for various conductive materials.....	81
3.5.2	Assessing the Distribution of ECM Materials and Configurations .....	86
3.5.3	Assessing the Distribution of ECM Applications.....	88
3.6	Conclusions .....	92
3.7	References .....	93
3.8	Supplementary Information.....	97
	References.....	99
Chapter 4: Evaluating conductive hollow fiber membrane performance in redox and adsorptive removal of methyl orange .....		
		101
4.1	Abstract .....	101
4.2	Introduction .....	102
4.3	Experimental .....	104
4.3.1	Materials .....	104
4.3.2	Adsorption Kinetics & Isotherms .....	105
4.3.3	CNT-coated Hollow Fiber Membrane Preparation & Characterization .....	106
4.3.4	Electrochemical Batch Removal of Methyl Orange .....	107
4.3.5	Continuous Electrochemical Removal of Methyl Orange in Crossflow Filtration	109
4.4	Results & Discussion .....	111
4.4.1	SW/DWCNT Adsorptive Removal of Methyl Orange in a Batch System.....	111

4.4.2	Electrochemical Batch Removal of Methyl Orange .....	115
4.4.3	Continuous Removal.....	118
4.5	Conclusions .....	121
4.6	References .....	122
4.7	Supplementary Information.....	125
Chapter 5:	Conclusions & Future Work .....	127
5.1	Conclusions .....	127
5.2	Future Work .....	130
5.3	References .....	134
Appendix A:	Supporting Information.....	135
A.1	Impact of Membrane Support Material on Conductive Hollow Fiber Membrane Properties .....	135
A.1.1	Introduction.....	135
A.1.2	Experimental.....	135
A.1.3	Results & Discussion .....	138
A.1.4	Conclusions.....	140
A.2	Challenges with establishing a metric to quantify carbon nanotube deposition .....	141
A.2.1	Introduction.....	141
A.2.2	Total Organic Carbon .....	141
A.2.3	UV-Vis-NIR Spectroscopy .....	143
A.2.4	Thermogravimetric Analysis .....	145
A.2.5	Surface Conductivity Correlation .....	148
A.2.6	Conclusions.....	149
A.3	References .....	150

## List of Figures

- Figure 1.1.** The filtration spectrum illustrating pore size distributions for separation techniques along with particle sizes for common contaminants. Adapted from [5]..... 2
- Figure 1.2.** Scanning electron micrograph of an asymmetric polyether sulfone membrane. .... 3
- Figure 1.3.** Module configurations for **a)** flat sheet membranes in a plate-and-frame model, **b)** spiral wound membrane, **c)** tubular membrane and **d)** hollow fiber membrane. Panels a, c, d were adapted from Synder Filtration [11]. .... 5
- Figure 1.4.** Schematic of two flow paths in membrane filtration: **a)** dead-end and **b)** crossflow. 5
- Figure 1.5.** Schematic of anti-fouling mechanisms for electrically conductive membranes. .... 12
- Figure 1.6.** Free body diagram demonstrated the forces acting on **a)** a particle in flow and **b)** a deposited particle. Forces involved: lift ( $F_L$ ), drag due to permeate flow ( $F_{Dy}$ ), drag due to crossflow ( $F_{Dx}$ ), van der Waals attractive force ( $F_{vdW}$ ) and friction ( $F_F$ ). .... 19
- Figure 1.7.** Schematic illustrating the two components of the inertial lift force: **a)** wall effect lift force ( $F_{WE}$ ) with velocity streamlines shown and **b)** shear-gradient lift force ( $F_{SG}$ ) with fluid velocities shown relative to the particle velocity. .... 19
- Figure 2.1 a)** Schematic of the crossflow deposition system. The identified components include: (1) Feed reservoir; (2) Peristaltic pump; (3) Pressure transducer; (4) Aluminum crossflow filtration sub-module; (5) Retentate line needle valve; (6) Retentate line rotameter; (7) Digital balance; (8) HF membrane. Locations for the feed (F), retentate (R), and permeate (P) streams around the filtration sub-module are identified. **b)** Picture of the experimental set-up with three crossflow deposition experiments running in parallel. Numbered components correspond to the same equipment identified in Panel a. **c)** Sample preparation for CNT-coated HF analysis. The CNT-coated HF is removed from sub-module and sectioned into six segments. Each segment is cut in half and folded open to the interior surface for analysis via four-point probe conductivity measurement (shown) and scanning electron microscopy..... 38
- Figure 2.2.** Hydraulic permeability (panel a) and surface conductivity (panel b) results for the CNT-coated HF membranes; the x-axis categories for both panels (a, b, c, d, e, and f) correspond to the six membranes that were made at each of the four conditions of the  $2^2$  DOE study. The error bars in panel a correspond to the 95% confidence intervals from the linear regression of permeate flux (LMH) and applied pressure (bar) for each individual membrane. The error bars in panel b correspond to the standard deviation of the triplicate measurements made on the six segments excised from each individual membrane. .... 44
- Figure 2.3.** Boxplot comparison of the hydraulic permeability results for the CNT-coated HF membranes prepared at the four conditions of the  $2^2$  DOE study and two control conditions

involving no CNTs. The results from the DOE study are organized according to the feed pressure and crossflow velocity values. For each boxplot, the mid-line corresponds to the median, the upper and lower box bounds correspond to the interquartile range, and the whiskers correspond to the maximum and minimum values. .... 50

**Figure 2.4.** Full-factorial regression models for the 2<sup>2</sup> DOE study evaluating CNT-coated HF membrane **a)** permeability and **b)** conductivity in terms of crossflow velocity (cm/s) and pressure (bar). The multiple linear regression model for panels are as follows: a)  $Permeability = -480 + 3575 \times v$  b)  $Conductivity = 84.7 - 1384 \times P - 317.9 \times v + 5361 \times (P \times v)$ . Note that models are defined only within the range of conditions studied in the DOE: crossflow velocity of 0.32–1.06 cm/s and feed pressure of 0.1–0.2 bar. The filled circular symbols within each panel indicate the four experimental results from the 2<sup>2</sup> DOE study. .... 50

**Figure 2.5.** Representative SEM images of the interior surface of the HF membranes in both top-down orientations (left panels a, c, and e) and cross-sectional orientations (right panels b, d, and f). The top row (panels a and b) corresponds to the unmodified PES HF membrane. The middle row (panels c and d) corresponds to a CNT-coated HF membrane produced at a deposition feed pressure of 0.2 bar, crossflow velocity of 1.06 cm/s, and feed concentration of 7.5 mg/L CNTs. The bottom row (panels e and f) corresponds to a CNT-coated HF membrane produced at a deposition feed pressure of 0.1 bar, crossflow velocity of 0.32 cm/s, and feed concentration of 18.8 mg/L CNTs. .... 52

**Figure 2.6.** Boxplot comparison of effects of CNT feed concentration on hydraulic permeability (panel a) and surface conductivity (panel b) for CNT-coated HF membranes. For each boxplot, the mid-line corresponds to the median, the upper and lower box bounds correspond to the interquartile range, and the whiskers correspond to the maximum and minimum values. Statistical analysis in panel a) was based on permeability measurements for six HF membranes and three HF membranes formed with CNT feed concentrations of 7.5 mg/L and 18.8 mg/L, respectively. Statistical analysis in panel b) was based on conductivity measurements for six segments excised from each individual membrane (i.e. 36 measurements at 7.5 mg/L, 18 measurements at 18.8 mg/L). .... 55

**Figure 2.7.** Robeson-like plot comparing the conductivity and permeability values for the 29 CNT-coated HF membranes that were fabricated in this study. Horizontal error bars correspond to the 95% confidence intervals from the linear regression analysis of filtrate flux (LMH) versus TMP (bar). Vertical error bars correspond to the standard deviation for the six segments from a single CNT-coated HF. The three symbol colours correspond to the range of feed pressure values. The round symbols (●, ○) and square symbols (■) correspond to crossflow velocities of 0.32 and 1.06 cm/s, respectively. The filled symbols (●, ■) and empty symbols (○) correspond to CNT concentrations in the feed suspension of 7.5 and 18.8 mg/L respectively. The upper performance limit (black line) was established by fitting an exponential curve to select data and then adjusting the model parameters such that the residual values were negative for all of the fitted data points:  $C = 1.27 \times 10^{10} \cdot Lp^{-2.00}$ . .... 58

**Figure 2.S1.** Sample feed pressure profiles for one PES HF membrane coated at a crossflow velocity of 1.06 cm/s, feed pressure of 0.2 bar and feed CNT concentration of 7.5 mg/L. Feed pressure was measured every 3 seconds via USB transducer at each of the following preparation stages: 1) pressurization 2) pre-coating permeability measurement 3) crossflow CNT deposition

4) rewetting first with 50 vol% isopropanol then with DI water and 5) post-coating permeability measurement. .... 67

**Figure 2.S2.** Collection of all 62 hydraulic permeability measurements for the unmodified PES HF membranes throughout the experimental study. The minimum and maximum values are 1,204 and 11,039 LMH/bar. The thick black line corresponds to the average of all 61 measurements of 5,540 LMH/bar. .... 68

**Figure 2.S 3.** P-value statistics from a series of two sample T-tests comparing coating membrane **a)** permeabilities and **b)** conductivities with the null hypothesis that sample means are equal. Values are read by matching conditions along the horizontal and vertical axes. Only the lower matrix is included due to the symmetry of the full matrix. Points where the null hypothesis is rejected ( $p < 0.05$ ) are shaded to indicate a statistically significant difference between these measured values. Experiments included:  $2^2$  DOE test conditions and permeabilities for two controls: “heat” control testing the curing process with no prior crossflow deposition and “PVA & Heat” control testing both crossflow deposition and curing excluding CNTs from the feed suspension. .... 69

**Figure 2.S4.** Photos of the six HF membranes prepared at each of the crossflow velocity and pressure conditions studied in the  $2^2$  full factorial DOE. The cartoon on the left shows how each HF was cut into six segments, cut in half and folded open prior to imaging. The six segments are identified from inlet (i) to outlet (vi) on each of the HF images..... 70

**Figure 2.S5.** Scanning Electron Microscopy (SEM) images of the unmodified PES HF membranes shown in cross-section at low magnification (a) for context and high magnification (b) to illustrate the interior skin layer and bulk porous layer. .... 71

**Figure 2.S6.** Residual plots for the multiple linear regression models of a) permeability and b) conductivity from the  $2^2$  full factorial Design-of-Experiments model evaluating two flow parameters: feed pressure and crossflow velocity. .... 72

**Figure 2.S7.** Crossflow deposition pressure profiles at a crossflow velocity of 0.32 cm/s and feed pressure of 0.1 bar for two different feed concentrations: a) 7.5 mg/L CNTs b) 18.75 mg/L CNTs. .... 73

**Figure 2.S8.** High magnification Scanning Electron Microscopy (SEM) images of the interior surface of two CNT coated HF membranes shown in Fig. 2.5. Image A corresponds to the CNT-coated HF membrane produced at a deposition feed pressure of 0.2 bar, crossflow velocity of 1.06 cm/s, and feed concentration of 7.5 mg/L CNTs (shown in Fig. 2.5 c, d). Image B corresponds to the CNT-coated HF membrane produced at a deposition feed pressure of 0.1 bar, crossflow velocity of 0.32 cm/s, and feed concentration of 18.8 mg/L CNTs (shown in Fig. 2.5 e, f). ..... 74

**Figure 3.1.** Series of Robeson-like plots comparing the conductivity and permeability values for 80 different electrically conductive membranes developed in 38 different published journal articles. Each panel represents a different class of conductive material used for developing the membrane: **a)** graphitic nanomaterials; **b)** metals; **c)** conductive polymers. Legend entries identify

the exact conductive material used. Composite materials belonging to more than one class are shown in each applicable panel. The upper performance limit (black line) in each panel was established by fitting an exponential curve to select data and then adjusting the model parameters such that the residual values were negative for all the fitted data points: **a)**  $C = 8.79 \times 10^9 Lp^{-1.91}$ ; **b)**  $C = 9.07 \times 10^{21} Lp^{-3.88}$ ; **c)**  $C = 1.11 \times 10^8 Lp^{-1.35}$  and  $C = 1.29 \times 10^6 Lp^{-2.17}$  when composite materials were excluded. .... 85

**Figure 3.2.** Distribution of the 80 data points in Figure 3.1. classified by conductive material used (inner ring), separation type (middle ring), and membrane configuration (outer ring). The arc length of each ring segment is proportional to the number of data points that fit in the category. Ring segments are coloured first according to conductive material (maroon for graphitic nanomaterials, blue for metallic and grey for polymeric), then by separation type (darkest shade for UF, middle shade for MF and lightest for NF/RO/FO), and are patterned according to membrane configuration (dotted for flat sheet, lined for hollow fiber and wave pattern for tubular). .... 88

**Figure 3.3.** Distribution of the 63 conductive membrane performance tests conducted in the 38 papers reviewed classified by the general application (inner ring), specific test (middle ring), and specific pollutant (outer ring) used. The arc length of each ring segment is proportional to the number of tests that fit in the category. Ring segments are coloured according to the general application (maroon for antifouling, blue for enhanced separations and grey for redox). ..... 89

**Figure 3.S1.** Series of Robeson-like plots representing the same conductivity/ permeability data from Fig. 3.1 with the specific applications each membrane was design for identified in the legend entries. Panels correspond to: **a)** graphitic nanomaterials; **b)** metals; **c)** conductive polymers. Composite materials belonging to more than one class are shown in each applicable panel. The same upper performance limits (black line) are included from Fig. 3.1..... 97

**Figure 4.1.** Photograph of the electrochemical batch removal experimental set-up. Working Electrode (WE), Counter Electrode (CE) and Reference Electrode (Ag/AgCl) are identified in the inset. .... 108

**Figure 4.2.** **a)** Schematic of the continuous electrochemical removal experimental set-up. Numbered items include: (1) Feed reservoir and stir plate; (2) Peristaltic pump; (3) Pressure transducer; (4) Stainless steel conductive membrane module; (5) Needle valve; (6) Rotameter; (7) DC power supply; (8) Ammeter. Feed (F), Retentate (R) and Permeate (P) lines are identified along with the sample point (S) for the permeate line. **b)** Model of the conductive membrane module (Item (4) in (a)). Further identified components include: (9) Metal needle working electrode; (10) CNT-coated HF membrane; (11) Metal connection point to module (counter electrode). **c)** Photograph of the conductive membrane module (Item (4) in (a)). .... 110

**Fig. 4.3 a)** Normalized methyl orange (MO) concentration as a function of contact time with 1 mg of SW/DWCNTs at two concentration levels of MO: 0.025 mM and 0.15 mM. Error bars represent the standard deviation between triplicate experiments. **b)** Temkin adsorption isotherms for a fixed 0.025 mM solution of MO after 24 h contact time with varying masses of SW/DWCNTs (10, 5, 2.5, and 1 mg). Raw data is shown as the maroon circles while the average of duplicate experiments

at each SW/DWCNT mass is shown as the yellow diamonds. Error bars on the x-axis represent the standard deviation in equilibrium MO concentration and error bars on the y-axis represent the standard deviation in calculated amount of MO adsorbed for the duplicate experiments. **c)** Langmuir, Freundlich and Temkin adsorption isotherm models for the same adsorption data in **b)** Fitted models: Langmuir  $q_E = (-0.074 \times -77.3 \times C_E)/(1 + (-0.074) \times C_E$ , Freundlich  $q_E = 2.80 \times C_E^{1.75}$ , Temkin  $q_E = 277.25 \times \log(0.29) + 277.25 \times \log(C_E)$ ..... 114

**Figure 4.4.** Normalized bulk methyl orange (MO) concentrations over time for 500 mL batch tests with two types of working electrodes: CNT-coated HF (blue squares) and stainless steel needle control (maroon circles). Step changes in applied are reported in the bottom panel..... 117

**Figure 4.5.** Normalized permeate methyl orange (MO) concentration and permeate flow rate over time for crossflow continuous removal experiments with two CNT-coated HF membranes at a feed flow rate of 0.5 mL/min and crossflow rate of 0.1 mL/min under two recycle modes of operation: a) retentate recycle; b) permeate and retentate recycle. A potential of -5V was applied after 30 min. .... 119

**Figure 4.S1.** UV-Vis calibration curves relating methyl orange (MO) concentration to absorbance at 454 nm. **a)** Curve developed for use with 48-well plates, used for majority of experiments. **b)** Curve developed for use with 96-well plates, used for electrochemical batch removal test in vertical orientation with the CNT-coated HF membranes..... 125

**Figure 4.S2.** Raw adsorption data for a fixed 0.025 mM solution of MO after 24 h contact time with varying masses of SW/DWCNTs (10, 5, 2.5, 1, 0.5, 0.1 mg). Data at 0.5 and 0.1 mg CNTs shown in circles due to their erroneous behaviour..... 125

**Figure 4.S3. a)** Schematic and photographs of the 50 mL horizontal configuration for the electrochemical batch removal experiments with the working (WE) and counter electrodes (CE) identified. **b)** Normalized bulk methyl orange (MO) concentrations over time for the 50 mL batch tests in horizontal configuration with two types of electrode connections: copper (maroon circles) and stainless steel (blue squares) alligator clips. Step changes in applied are reported in the bottom panel..... 126

**Figure 4.S4.** Unmodified PES HF membrane control filtration experiments with the continuous removal experimental set-up. Tests a & b are identical, each with two different HF membranes (four membranes in total)..... 126

**Figure 5.1.** Proposed conductive hollow fiber membrane module designs for an a) inside-out and b) outside-in hollow fiber configuration. .... 133

**Figure A.1.** Schematics for dead-end CNT deposition coating experimental set-ups. **a)** Outside-in surface deposition via vacuum filtration **b)** Inside-out surface pressure deposition. .... 137

**Figure A.2.** Schematic of the four-probe conductivity test (left) and photo of the copper alligator clip probes in the experimental set-up (right). Clip spacing: 1 cm. .... 137

**Figure A.3.** Digital photographs of CNT-coated HF membranes with **a)** outside-in PVDF and **b)** inside-out PES support membranes. Uncoated PVDF membranes shown on the far sides in (a).  
..... 138

**Figure A.4.** Scanning Electron Microscopy (SEM) images of the CNT-coated PVDF HF membrane exterior surface (a) and in cross-section (c) and of the CNT-coated PES HF membrane interior surface (b) and in cross-section (d).  
..... 139

**Figure A.5.** Surface conductivity measurements for the **a)** exterior surface of CNT-coated PVDF HF membranes and **b)** interior surface of CNT-coated PES HF membranes.  
..... 140

**Figure A.6.** Calibration curve relating total organic carbon (TOC) reading to known carbon nanotube (CNT) concentrations. Same dilution series was created twice to generate two models.  
..... 143

**Figure A.7.** CNT concentrations measured via TOC measurement (calibration parameters from Model #2) for the initial, final and permeate samples collected during dead-end deposition onto the PVDF HF support membranes.  
..... 143

**Figure A.8.** UV-Vis-NIR spectra (top row) and calibration with CNT concentration at 260 nm (bottom row) for two types of CNT suspensions: **a)** CNTs and SDS dispersed in a 1:1.5 mass ratio in DI water; **b)** CNTs, SDS and PVA dispersed in a 1:1.5 CNT:SDS and 1:10 CNT:PVA mass ratio in DI water. Reported absorbances have been normalized by subtracting the absorbance of a sample of DI water.  
..... 144

**Figure A.9.** TGA thermographs for **a)** powdered CNT, PVA and SDS samples as well as the Repligen PES HF membrane and **b)** PES flat sheet membrane control and coated with PVA/SDS solution as well as three masses of CNTs: 1.5, 0.15, 0.015 mg. Inset shows weight percentages towards the end of the heating process. Photograph inset shows PES flat sheet membranes coated with the three masses of CNTs. .... 147

**Figure A.10.** **a)** Calibration curve relating surface conductivity measurements to known CNT masses deposited on the surface of PES flat sheet membranes. Error bars represent the standard deviation between two membrane samples. **b)** Photographs of the CNT-coated flat sheet membranes used to generation the calibration curve.  
..... 149

## List of Tables

<b>Table 1.1.</b> Literature conductivity and permeability values for carbon nanotube based electrically conductive hollow fiber membranes .....	15
<b>Table 2.S1.</b> Design-of-experiments multiple linear regression model coefficients, p-values and $R^2$ for two responses: permeability and conductivity. Coefficients were calculated for each input variable (pressure, crossflow velocity) and the interaction parameter (pressure $\times$ velocity).....	72
<b>Table 2.S2.</b> Measured CNT-coated HF membrane permeabilities and surface conductivities used to develop the upper limit line in the Robeson-like plot (Fig. 2.7). Model parameters (k, n) were determined by fitting an equation of the form $C = kLp^n$ to the data points below where C is the conductivity, and $Lp$ is the permeability. Parameters were then manually adjusted such that the residual values were negative for all the fitted data points. Conductivities predicted using the upper limit equation $C = 1.27 \times 10^{10} \cdot Lp^{-2.00}$ are included below along with their corresponding residuals....	73
<b>Table 3.1.</b> Recommended standard tests/ pollutants for evaluating common ECM applications. ....	91
<b>Table 3.S1.</b> Literature values for conductive membrane hydraulic permeability and surface conductivity used to develop the upper limit line for graphitic nanomaterials in the Robeson-like plot (Fig. 3.1a). Conductivities predicted using the upper limit equation $C = 8.79 \times 10^9 \cdot Lp^{-1.91}$ are included below along with their corresponding residuals.....	98
<b>Table 3.S2.</b> Literature values for conductive membrane hydraulic permeability and surface conductivity used to develop the upper limit line for metals in the Robeson-like plot (Fig. 3.1b). Conductivities predicted using the upper limit equation $C = 9.07 \times 10^{21} \cdot Lp^{-3.88}$ are included below along with their corresponding residuals. ....	98
<b>Table 3.S3.</b> Literature values for conductive membrane hydraulic permeability and surface conductivity used to develop the upper limit line for conductive polymers in the Robeson-like plot (Fig. 3.1c). Conductivities predicted using the upper limit equation $C = 1.11 \times 10^8 \cdot Lp^{-1.35}$ are included below along with their corresponding residuals.....	98
<b>Table 3.S4.</b> Literature values for conductive membrane hydraulic permeability and surface conductivity used to develop the upper limit line for conductive polymers excluding composite materials in the Robeson-like plot (Fig. 3.1c). Conductivities predicted using the upper limit equation $C = 1.29 \times 10^6 \cdot Lp^{-2.17}$ are included below along with their corresponding residuals. ....	99
<b>Table 4.1.</b> Isotherm parameters for adsorptive removal of MO by SW/DWCNTs.....	113
<b>Table 4.2.</b> Properties for the CNT-coated HF membranes used in the continuous removal experiments. Error ranges for surface conductivities represent the standard deviation between triplicate four-point probe measurements. Error ranges for permeabilities represent the 95% confidence intervals for the slopes of the flux/pressure curves. ....	119
<b>Table 5.1.</b> Carbon nanotube suppliers and purchasing options. The CNTs used in this study are included for reference. ....	131

## Abbreviations & Symbols

Ag/AgCl	Silver/ Silver chloride
B	Temkin isotherm model parameter
C	Conductivity
C <sub>0</sub>	Initial concentration
C <sub>E</sub>	Equilibrium concentration
CE	Counter Electrode
CNT	Carbon Nanotube
COC	Chlorinated Organic Compound
DC	Direct current
D <sub>H</sub>	Hydraulic diameter
DI	De-ionized
DOE	Design-of-experiments
ECM	Electrically Conductive Membrane
EPS	Extracellular polymeric substances
F	Feed
F <sub>Dx</sub>	Crossflow Drag Force
F <sub>Dy</sub>	Permeation Drag Force
F <sub>F</sub>	Friction Force
F <sub>L</sub>	Inertial Lift Force
FO	Forward Osmosis
F <sub>SG</sub>	Shear-gradient inertial lift force
F <sub>vdw</sub>	van der Waal Attractive Force
F <sub>WE</sub>	Wall-effect inertial lift force
HF	Hollow Fiber
ID	Inner diameter
J	Flux
k	Model parameter constant for “Robeson-like” plots
K <sub>t</sub>	Temkin isotherm model parameter
LMH	L/m <sup>2</sup> /h (flux units)
L <sub>p</sub>	Hydraulic permeability
m	Mass (of adsorbent)
MF	Microfiltration
MO	Methyl Orange
MW	Molecular Weight
MWCNT	Multi walled carbon nanotube
n	Model parameter exponent for “Robeson-like” plots
NF	Nanofiltration
Ni	Nickel
OD	Outer diameter
P	Permeate
PAN	Polyacrylonitrile
PANI	Polyaniline
PES	Polyether sulfone
PVA	Polyvinyl alcohol

PVDF	Polyvinylidene fluoride
$q_E$	Equilibrium adsorption capacity
R	Retentate; Sheet Resistance
Re	Reynolds number
RO	Reverse Osmosis
ROS	Reactive Oxygen Species
RPM	Rotations per minute
S	Sample point
S/m	Siemens/ meter (surface conductivity units)
SDS	Sodium dodecyl sulfate
SEM	Scanning Electron Microscopy
SS	Stainless steel
SW/DWCNT	Single walled/ double walled carbon nanotube
t	Thickness
TGA	Thermogravimetric analysis
TMP	Transmembrane Pressure
TOC	Total organic carbon
UF	Ultrafiltration
UV-Vis-NIR	Ultraviolet-visible-near infrared spectrum
V	Volume
v	Characteristic Velocity
WE	Working Electrode
$\Delta P$	Transmembrane pressure
$\sigma$	Surface conductivity
$\rho$	Density
$\mu$	Dynamic viscosity

## Declaration of Academic Achievement

This work has been written in the following format. There is some repetition in introduction and methods between chapters, however all results are unique.

- Chapter 2: M. J. Larocque, D. R. Latulippe, C. F. de Lannoy, Formation of electrically conductive hollow fiber membranes via crossflow deposition of carbon nanotubes – Addressing the conductivity/ permeability trade-off, *J. Memb. Sci.* (2020). Accepted for publication: <https://doi.org/10.1016/j.memsci.2020.118859>
- Chapter 3: M. J. Larocque, A. Gelb, D. R. Latulippe, C. F. de Lannoy, A universal method for evaluating electrically conductive membrane performance: comparative review of the conductivity/ permeability trade-off.
- Chapter 4: M. J. Larocque. Evaluating conductive hollow fiber membrane performance in redox and adsorptive removal of methyl orange.

The content in Chapter 2 and 3 has been reproduced from the accepted/ prepared publication with a preface connecting the work to the remaining chapters. Melissa Larocque is responsible for planning, performing, analyzing and writing the content in each chapter between May 2019 – November 2020 under co-supervision by Dr. David Latulippe and Dr. Charles-François de Lannoy who both contributed to project planning for all chapters, as well as writing, and revising chapters 2 and 3. The following undergraduate students have contributed to parts of this thesis:

- Jasmine Kurtz assisted with performing some of the experiments included in Appendix A in summer 2019
- Adi Gelb assisted with literature review and data analysis in Chapter 3 in summer 2020

# Chapter 1: Introduction

## 1.1 Membrane Technologies

### 1.1.1 Terminology & Classification

Membrane separation technologies are a prominent purification strategy in several fields due to their low energy requirements, simple design and operation, and high removal efficiency. Example applications include municipal and industrial wastewater treatment [1], drinking water and desalination [1], petrochemical purification [2], gas separations [3], and bioprocessing [4]. A membrane serves as a thin, selectively permeable barrier that separates particles based on a variety of properties, such as size, charge, or diffusivity. Size exclusion, where particles larger than the membrane pore size are rejected, is one of the more common separation mechanisms thus membranes are often classified by the size of their pores. These classes include: microfiltration (MF) for pore size  $\sim 0.1\text{-}10\ \mu\text{m}$ , ultrafiltration (UF)  $\sim 2\text{-}100\ \text{nm}$ , nanofiltration (NF)  $\sim 0.5\text{-}2\ \text{nm}$  and reverse osmosis (RO)  $< 0.5\ \text{nm}$  [1]. RO membranes are unique as they have a dense structure where separation is defined by solution-diffusivity affinity rather than size exclusion [1]. MF, UF, NF and RO membrane separations are all pressure-driven processes. In typical operation, a pressurized feed source is separated into two streams: 1) a clean permeate that has filtered through the membrane and 2) a retentate rejected by the membrane. Figure 1.1 illustrates the pore size distributions in the MF/UF/NF/RO filtration spectrum as well as the sizes of several common contaminants.

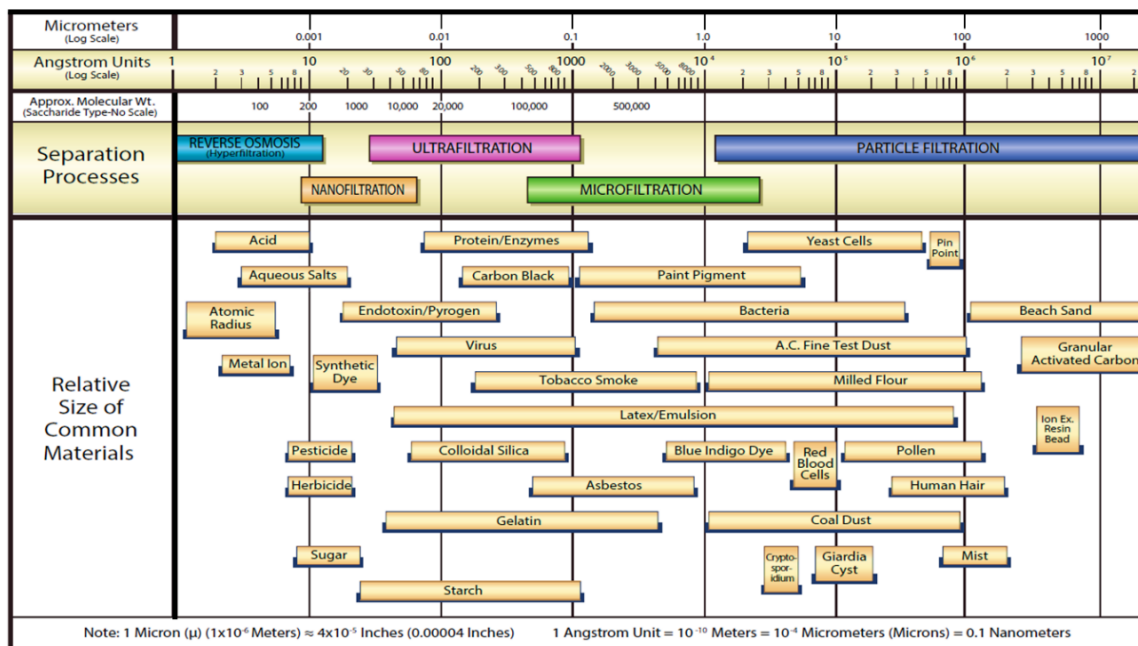


**Figure 1.1.** The filtration spectrum illustrating pore size distributions for separation techniques along with particle sizes for common contaminants. Adapted from [5].

Membranes can be further classified by the type of material used in fabrication which generally include polymers or inorganic materials. Membrane polymers include natural (e.g. cellulose, rubber) or synthetic (e.g. polyether sulfone, polyvinylidene fluoride, polyamide) materials [6]. Inorganic materials for membrane synthesis include ceramics, silica, or metals. These materials are useful for operation in extreme conditions that could compromise polymeric membranes, such as high temperatures ( $> 200^{\circ}\text{C}$ ), extreme pH values, or when filtering reactive chemicals. Polymeric membranes are generally preferred in most other applications due to their low cost and ease of manufacture [6,7].

Membrane structures can be symmetric, where pore size is constant throughout the matrix, or asymmetric, where a skin layer with a tight pore structure ( $\sim 0.1\text{-}1\ \mu\text{m}$  thick) is combined with a more porous support structure. The skin layer defines the pore size for separation while the support layer provides physical stability and reduces resistance to flow through the membrane [1,6,8]. A micrograph of an asymmetric polyether sulfone membrane is included in Fig. 1.2.

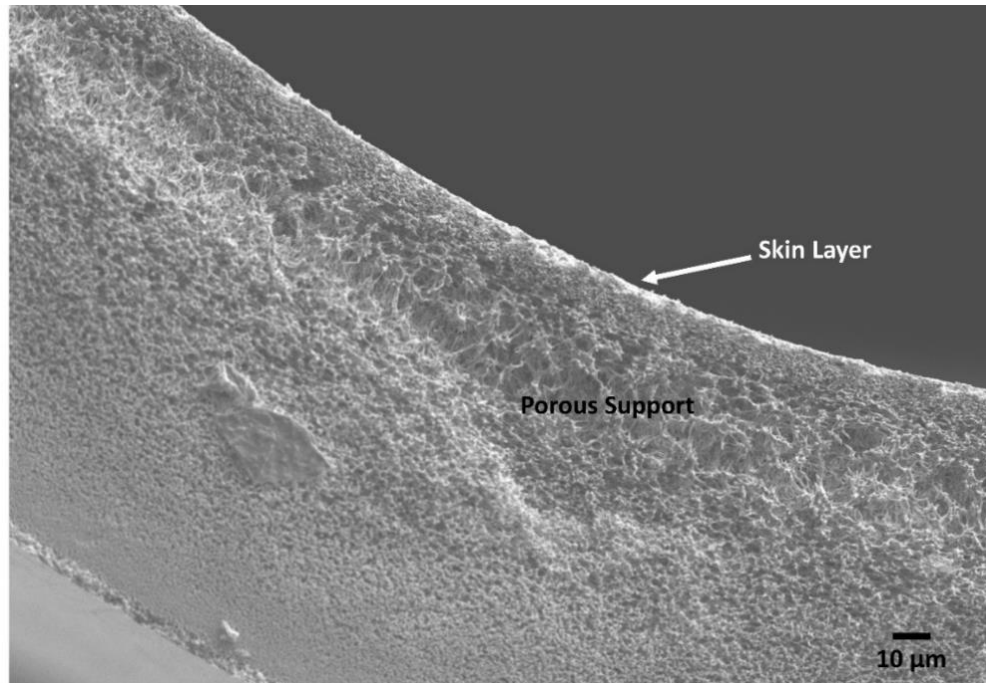


**Figure 1.2.** Scanning electron micrograph of an asymmetric polyether sulfone membrane.

Commercial membrane filtration modules are available in several configurations depending on the membrane geometry including flat sheet, spiral, tubular and hollow fiber membranes as illustrated in Fig. 1.3. Flat sheet membranes are common in lab-scale filtration experiments where a single membrane can be sealed in a pressurized cell. In industrial applications, multiple flat sheet membranes can be stacked in a plate-and-frame format, sandwiched between support plates where permeate is collected [8]. This format increases the membrane area available for separation, with a packing density of 30 to 500 m<sup>2</sup>/m<sup>3</sup> [6]. Spiral-wound modules consist of two flat sheet membranes separated by a spacer and rolled around a perforated collection tube. Feed flows axially while filtered permeate is directed inwards along the spacer towards the collection tube [8]. Spiral-wound modules generally have a higher packing density than plate-and-frame models around 200 to 800 m<sup>2</sup>/m<sup>3</sup> [6]. In a tubular membrane module, feed flows along the inner channel of a series of tubes ~12 mm in diameter and is filtered outwards towards the shell of the module. The tube itself typically contains an inner membrane layer and an outer porous support

so filtration occurs in an inside-out direction [6,8]. Due to the large diameter of the tubes, this format generally produces low packing densities  $\sim 30$  to  $200 \text{ m}^2/\text{m}^3$  [6]. Hollow fiber (HF) membrane modules are similar in appearance to tubular membranes apart from two major differences: 1) HF membrane diameters are much smaller  $\sim 1 \text{ mm}$  and 2) the membrane layer is commonly formed on either the inside or outside surface of the tube (i.e. filtration can occur in an inside-out or outside-in direction) [6,8]. The small diameters allow for hundreds to thousands of fibers to be packed in a single module, with packing densities of  $500$  to  $9,000 \text{ m}^2/\text{m}^3$  ( $\sim 20$  to  $300$  times higher than plate-and-frame modules) [6]. Given the small diameter however, HF membranes tend to be more susceptible to fouling than their counterparts [6,8].

There are generally two different flow paths during membrane operation: 1) dead-end and 2) crossflow filtration, shown in Fig. 1.4. In dead-end filtration, the feed flows normal to the membrane surface and is forced through the membrane into the permeate stream. Rejected particles deposit on the surface unless a re-mixing mechanism is incorporated into operation; there is no retentate stream. In crossflow filtration, the feed flows tangentially to the membrane surface where it can pass through the membrane into the permeate stream or continue along the membrane surface and exit the module in the retentate stream. The hydrodynamically induced lift or shear effects in crossflow operation are advantageous for preventing particle deposition and fouling thus preserving membrane longevity [9,10].

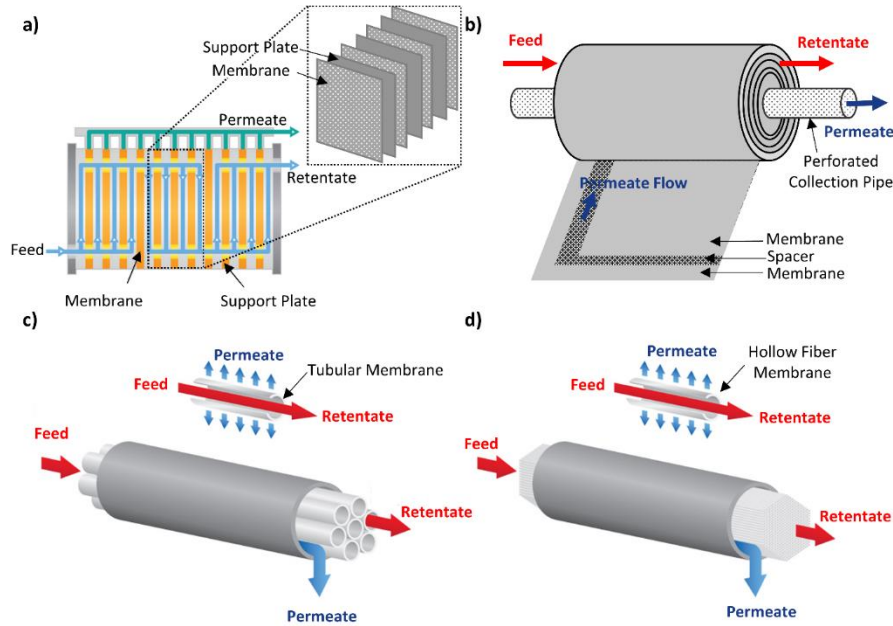


**Figure 1.3.** Module configurations for **a)** flat sheet membranes in a plate-and-frame model, **b)** spiral wound membrane, **c)** tubular membrane and **d)** hollow fiber membrane. Panels a, c, d were adapted from Synder Filtration [11].

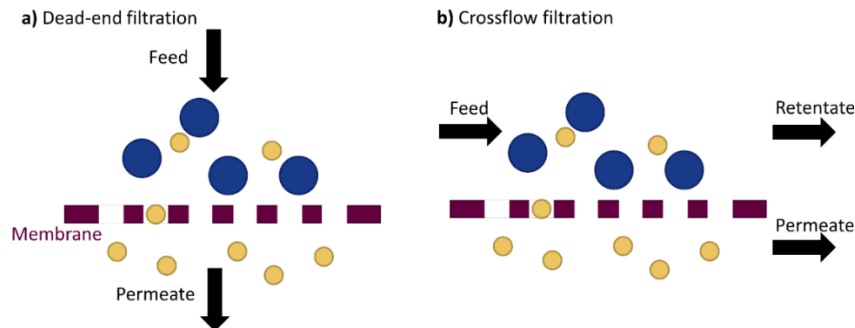


**Figure 1.4.** Schematic of two flow paths in membrane filtration: **a)** dead-end and **b)** crossflow.

A key limitation in membrane science is the trade-off between permeability and selectivity. Permeability is a measure of permeate flux, normalized by the pressure across the membrane (transmembrane pressure, TMP). Flux is expressed as permeate flow rate divided by available membrane area (e.g. units: L/m<sup>2</sup>h, LMH). Permeability is calculated using the following equation:

$$L_p = \frac{J}{\Delta P} \quad (1)$$

where  $L_p$  is the permeability (LMH/bar),  $J$  is the membrane flux (LMH) and  $\Delta P$  is the TMP (bar).

Selectivity is a metric for describing the affinity of the membrane separation for the desired product

over smaller impurities. For size exclusion membranes, the selectivity of certain compounds can be enhanced by decreasing pore size; however, this also decreases permeability by impeding flow through the pores. This inherent inverse relationship between permeability and selectivity was first identified by Robeson in the gas separation membrane field [12], but similar analyses have since been applied to desalination [13,14] and protein purification [15]. Overcoming the upper limits for these two metrics is a key goal of new membrane development.

### *1.1.2 Challenges & Limitations*

Despite the advantages and range of applications for membrane technologies, there are still several challenges to be addressed from an operational and functional standpoint. Long-term membrane operation is limited by fouling, incurring additional costs for frequent cleaning cycles and ultimate replacement of affected membranes. Functionally, membranes are limited by the selectivity/ permeability trade-off identified in Section 1.1.1. Many small, harmful contaminants cannot be removed by high flux membrane processes and must rely on dense membranes with much lower throughput. These issues are addressed further below.

Fouling is one of the most significant operating challenges for long-term membrane separation processes. Membrane fouling occurs when particles in the feed solution deposit or adsorb to the membrane surface or inside the pores, resulting in a decline in flux under constant TMP conditions, or an increase in TMP under constant flux conditions [16]. Some membrane performance can be recovered via physical (e.g. backwashing, scouring) or chemical cleaning methods; this is termed reversible fouling. Irreversible fouling cannot be recovered by these simple means and over time will require membrane replacement [6,16]

Fouling can be further classified as: biofouling, particulate/ colloidal fouling, organic fouling, and inorganic fouling, or scaling. Biofouling occurs when microorganisms such as

bacteria deposit on the membrane surface and form biofilms. Biofilm formation is a complicated process with many steps but generally involves: 1) bacteria adhesion and 2) bacterial excretion of extracellular polymeric substances (EPS) [17]. EPS make up a significant portion of biofilms (~50-90%) [18] and tend to make biofilms resistant to many common disinfectants such as biocides or chlorine [19]. Particulate/ colloidal foulants are inorganic or organic particles ~1 nm to 100  $\mu\text{m}$  in size that interact with the membrane surface via convective transport [16,20]. There are three main mechanisms for particulate/ colloidal fouling: 1) initial pore blockage; 2) cake layer formation; and 3) concentration polarization [16,20,21]. The first two mechanisms directly impede membrane flux by increasing membrane resistance due to pore blockage and adding another level of resistance in the cake layer. The presence of this cake layer can induce a concentration polarization effect due to the increased particle concentration at the membrane surface compared to the bulk, resulting in increased particle breakthrough into the permeate and increased osmotic pressure which can reduce permeation rate in NF/RO processes [16,20]. Organic foulants consist of dissolved components or colloids that adsorb to the membrane surface. Flux is impeded by initial pore blockage as well as subsequent formation of a gel layer on the membrane surface [16]. Inorganic foulants consist of dissolved components such as metals that precipitate on the membrane surface in a process known as scaling. This is a major issue for NF/RO processes with high salt concentrations where solubility limits may be exceeded [16,22]. One or more of these types of fouling can affect membrane surfaces depending on the chemical content of the feed source.

Pressure-driven MF/UF membrane processes are limited to separation based on a size exclusion mechanism and due to their large pore sizes, cannot remove small organic particles or other contaminants that can have detrimental health and environmental effects. For example, chlorinated organic compounds (COCs, found in pesticide run off and industrial effluents), azo

dyes (common in textile industry effluents), and heavy metals (found in mine tailings) accumulate or persist in the environment and have known toxic, mutagenic, and carcinogenic potential [23–26]. Although NF/RO membranes have been demonstrated to successfully remove COCs [27], azo dyes [28,29], and heavy metals [30], they are high-pressure, low flux, and energy intensive processes that often require pre-treatment to protect the membrane surface from damage due to particulates or chemicals (e.g. chlorinated disinfectants, oxidants) in the feed [1,28,31]. This presents an opportunity for process intensification if the combined pre-treatment and NF/RO process could be replaced by a single unit operation. Furthermore, in a conventional membrane process, these contaminants are only physically removed from the feed and not chemically degraded, therefore presenting a risk for re-introduction into the environment.

### *1.1.3 Current Trends in Membrane Development*

In the previous section, two major challenges for membrane processes were identified as fouling propensity and overcoming the selectivity/ permeability barrier for small toxic contaminants. Current strategies for fouling mitigation can generally be categorized as: 1) operational, 2) pre-treatment, or 3) material modifications. Strategies to improve separation efficiency and accomplish degradation of contaminants will also be discussed below.

Operational fouling mitigation strategies include controlling hydrodynamic conditions or incorporating cleaning cycles between filtrations. Use of crossflow filtration (see Fig. 1.4) is a simple, effective approach as the tangential flow induces shear effects that can prevent particle deposition and fouling [9,10]. Many commercial technologies have already taken advantage of this technique due to its simplicity (see Fig. 1.3). Air sparging, where air is injected with the feed water, is another strategy for inducing shear stress to remove deposited particles [32,33]. Depending on the relative gas and liquid velocities, air bubbles can be dispersed in the liquid phase

or present as large slugs that alternate with liquid flow [34]. Both configurations have been demonstrated to effectively remove external fouling (i.e. the cake layer) [33,34]. Internal fouling (i.e. in the membrane pores) is more challenging and can only be effectively removed in intermittent cleaning cycles. Typically, both internal and external fouling can be addressed via a simple backwashing process where clean water is fed in the opposite direction of the feed water (i.e. outside-in to inside-out) [32,33]. For more severe fouling, chemical cleaning may be required where the membranes are soaked in a cleaning agent such as an acid (e.g. nitric, hydrochloric), base (e.g. sodium hydroxide), oxidant (e.g. sodium hypochlorite), or surfactant (e.g. sodium dodecyl sulfate) to target particularly challenging organic and inorganic foulants [32]. In both backwash and chemical cleaning cycles however, the membrane must be taken offline, incurring additional costs for lost product. Other techniques for cleaning include mechanical methods such as rotating [35] or vibrating [36] membranes which use motion to induce shear effects, and ultrasonic cleaning where ultrasound waves are used to displace deposited particles [37]. These methods can be energy and maintenance intensive however due to wearing of mechanical parts.

Pre-treatment unit operations are often installed before membrane processes to remove foulants before contacting the membrane surface. This is especially useful for NF/RO processes as these dense membranes are susceptible to severe fouling and damage from particulates and chemicals in the feed. Conventional pre-treatment unit operations for NF/RO include MF/UF membranes, biological treatment, coagulation or flocculation, and adsorption [1][38]. Incorporation of an additional unit operation incurs large capital and operating expenses, making this is one of the most expensive techniques for mitigating fouling.

Development of antifouling membrane materials is a diverse field of research, however there are two main approaches that manipulate 1) surface interactions and 2) chemical reactivity.

Passive surface interactions between foulants and the membrane surface can be altered by controlling hydrophilicity. Increased surface hydrophilicity is generally desired as a method for reducing bacterial attachment [18]. Grafting of polyethylene glycol or zwitterionic polymer brushes onto the membrane surface has been shown to mitigate organic fouling through two primary mechanisms: 1) steric repulsion from the long polymer chains and 2) formation of a hydration layer between chains due to hydrogen bonding with water molecules [39,40]. Alternatively, hydrophobic surfaces with low surface energy can aid with the release of adhered foulant particles via hydrodynamic shear mechanisms. The hydrophobic surface, often based on silicon or fluorine chemistry, weakens the interfacial bond with foulants such as bacteria cells, facilitating removal [39,41]. Active surface modifications confer chemical reactivity to the otherwise inert membrane surface. For example, membrane coatings containing silver nanoparticles actively prevent biofouling due to release of silver ions and generation of reactive oxygen species (ROS, e.g. hydroxyl radicals), creating a toxic environment for bacteria growth [39]. Similar coatings have been developed using metallic oxides (e.g. copper, magnesium, titanium) to generate ROS through catalytic or photocatalytic mechanisms [42,43]. Membranes with an electrically conductive surface are unique in that they use both passive (i.e. electrostatic repulsion [44]) and active (i.e. ROS generation [45]) mechanisms for fouling prevention under an applied potential, as discussed further in Section 1.2.

Another major challenge for membrane operation is the limited ability for removal of small toxic contaminants such as COCs, azo dyes, and heavy metals with MF/UF processes. Only conventional NF/RO membrane processes can remove these contaminants; however, these membranes require high pressures and produce low throughput. Taking azo dyes as an example, other conventional removal techniques include advanced oxidation, adsorption, and

electrochemical methods. In advanced oxidation, azo dyes are degraded by strong oxidizing agents such as Fenton's reagent, ozone, or sodium hypochlorite. Both advanced oxidation and adsorption incur large operating costs due to consumption of expensive oxidizing agents and regeneration of adsorbent, respectively [46]. Electrochemical processes present a cost-effective alternative as oxidative degradation is accomplished through direct anodic oxidation and indirectly through generated ROS, without consuming additional chemicals [47]. Similar electrochemical processes have been used for reductive degradation of COCs [48] and physical removal of heavy metals [30]. Additional research has considered combining MF/UF membrane separations with these electrochemical processes. For example, electrically charged membrane surfaces have demonstrated successful degradation of surrogate azo dyes under an applied potential [49,50], with enhanced removal through incorporation of catalytic nanoparticles [51]. Similar membrane composites have been used to reduce heavy metals to inert forms (i.e. hexavalent chromium [52]), and oxidize various organic contaminants (i.e. phenol [45,53], tetracycline [53]). This approach is advantageous as it combines high throughput MF/UF processes with contaminant degradation or conversion to inert forms, eliminating any potential for re-introduction into the environment.

## **1.2 Electrically Conductive Membranes**

### *1.2.1 Benefits & Applications for Conductive Membranes*

Electrically conductive membranes (ECMs) are of significant research interest for their ability to address several of the concerns mentioned in Section 1.1, including fouling, and removal or degradation of small toxic contaminants. Applying an electric potential across a conductive membrane surface has been demonstrated to successfully mitigate fouling in biofouling [50,54–56], organic fouling [50,57,58], and scaling [59] applications. The following mechanisms have been proposed to explain the ECM anti-fouling effect: electrostatic repulsion [44], generation of

reactive oxygen species (ROS) via water splitting [45], and steric repulsion due to gas bubble generation [60]. These mechanisms are illustrated in schematic form in Fig. 1.5; it is likely a combination of these effects that defines ECM anti-fouling capability. Other factors, such as the magnitude and direction of applied potential, determine which effects are dominant. For example, gas bubble generation typically only occurs above a threshold potential [60]. ECMs have also been combined with electrical impedance spectroscopy as a method for detecting the onset of fouling [61,62]. This information would be valuable for optimizing cleaning cycle schedules to prevent irreversible fouling. Fouling mitigation and detection would help increase the longevity of membranes in long-term operations.

The charged membrane surface can enhance rejection in both MF/UF [63] and NF/RO [64] applications via electrostatic repulsion. Furthermore, redox reactions directly at the membrane surface or from generated sources (e.g. ROS) have been exploited for specialized contaminant removal (e.g. azo dyes and chlorinated compounds [51,65], hexavalent chromium [66], phenol [45,53], tetracycline [53]). Many of these contaminants have toxic or carcinogenic effects (e.g. azo dyes [24]) or detrimental environmental effects (e.g. chlorinated pesticides, such as atrazine which inhibits growth of photosynthetic plants [67]); by degrading these compounds or converting them to an inert form, ECMs eliminate the risk for re-introduction into the environment.

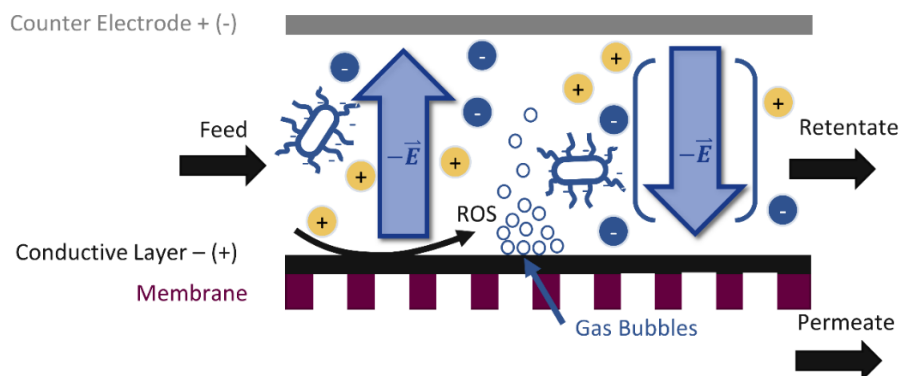


**Figure 1.5.** Schematic of anti-fouling mechanisms for electrically conductive membranes.

### 1.2.2 *Materials & Methods for Fabrication*

A variety of methods have been developed for fabricating ECMs but typically make use of the following classes of conductive materials: 1) metals (e.g. titanium oxide [68–70] gold [71], nickel [72], copper [73]), 2) conductive polymers (e.g. polypyrrole [74], polyaniline [75,76]), and 3) graphitic nanomaterials (e.g. carbon nanotubes [56,58,77], graphene [53]). Metals have been incorporated into surface coatings on traditional membrane materials with good uniformity and low thickness [72]. However, current fabrication processes have several limitations including energy intensive metallic sintering and reduction steps [68,73], use of hazardous reducing agents [72], or incorporation of specialized equipment and protocols, such as electrospraying [70], sputter coating [71], or atomic layer deposition [69]. Conductive polymers have been surface localized onto a support membrane via polymerization at the membrane surface [74–76] or casting directly onto the surface via phase inversion [76] to combat their relatively poor physical stability. These polymers are traditionally difficult to cast due to their poor solubility in common solvents [78]. To date, graphitic nanomaterials are used in most ECM fabrication protocols.

Within the class of graphitic nanomaterials, carbon nanotubes (CNTs) have shown significant promise due to their high conductivity and wide range of chemical functionalizations. CNTs are 3D tubular nanomaterials consisting of a network of  $sp^2$  hybridized carbon atoms which allow for propagation of an electric current. Single-walled CNTs (SWCNT) consist of one of these tubes; multi-walled CNTs (MWCNTs) consist of multiple layers wrapped around the smallest tube. CNTs have a characteristically high aspect ratio (length:diameter > 1000:1) and a semi-flexible structure [79] that allows formation of porous networks. Additional benefits of CNTs for ECM applications include their ability to facilitate redox reactions [66], high adsorptive capacity [80], and high chlorine tolerance [81].

CNT-based ECMs have been fabricated both as self-supporting CNT networks and in composites with traditional membrane materials. Self-supporting CNT networks have been especially useful for small-scale biomolecule purification and drug-delivery as these membranes allow for highly specific, controlled transport through the CNTs themselves with high resulting flux [82]. However, the limited pore control and large quantities of expensive conductive material required limit the applicability of this technique in large-scale treatment applications. CNTs can also be cast directly into membrane structures, either with traditional membrane polymers to create a composite material [57], or directly into a porous self-supported CNT network [63]. More commonly, CNT-based ECMs have been fabricated via direct vacuum or pressure deposition of dispersed CNTs onto the surface of a support membrane [58,59,64,77,83]. We have previously studied similar deposition techniques for various graphitic nanomaterial based ECMs, including SW/DWCNTs, MWCNTs, and carbon nanofibers (CNFs), however significantly higher surface conductivities were achieved with SW/DWCNTs. Furthermore, functionalized CNTs (e.g. carboxyl groups) are more easily dispersed in water [84], allowing for formation of more homogeneous deposited layers and improved stability due to the ability to form chemical cross-links [85]. Carboxyl functionalized SW/DWCNTs were selected as the primary conductive material in this work for their high conductivity and ease of dispersibility.

### *1.2.3 Geometry & Scale-up*

To date, most ECM development has been limited to the flat sheet membrane format. As mentioned in Section 1.1, other membrane formats offer higher packing densities which can maximize throughput in large industrial processes. Hollow fiber (HF) membranes are particularly advantageous due to their high packing density and robust, self-supporting design. However, due to their small diameter, HF membranes are more susceptible to fouling [6,8]. Fabricating ECMs in

a HF format could improve HF operation due to ECM antifouling potential and would easily allow for ECM scale-up to full-scale treatment in industrial applications.

Recent progress has been made towards ECM fabrication in a HF format using metals [68,72,73], conductive polymers [74], and graphitic nanomaterials [63,86–88]. Among these conductive materials, carbon nanotubes (CNTs) show significant promise due to their high conductivity and ability to form porous, thin film structures as outlined in Section 1.2.2. CNT-based conductive HF membranes have been developed using two major techniques: direct casting and surface deposition onto a support membrane. Using a wet-spinning technique, multi-walled CNTs (MWCNTs) were cast directly into a porous HF membrane structure with a pore size of ~100 nm [63]. Although these membranes demonstrated good anti-fouling behaviour in a subsequent membrane bioreactor study [74], this fabrication process has limited pore control and has yielded low surface conductivities (1.2 S/m) compared to the deposition approach. A vacuum or pressure deposition approach has been used more commonly for a variety of polymeric supports. In a forward osmosis application, MWCNTs were vacuum deposited onto the surface of poly(amide-imide) membranes to enhance water permeability and salt flux [86]. Wei et al. extended the vacuum deposition technique to two layers of nanomaterials on a polyacrylonitrile (PAN) support: ~48 nm layer of reduced graphene oxide followed by ~30  $\mu\text{m}$  layer of MWCNTs to improve physical stability [87]. Although the excess deposition of nanomaterials gave the membrane surface good conductivity (280 S/m), it also resulted in poor flux. A better balance between flux and conductivity was achieved by Du et al. where the PAN support was fabricated via electrospinning prior to vacuum deposition of a thin MWCNT layer (~1.5  $\mu\text{m}$ ) [88]; however, the limited scalability of electrospinning presents a major challenge. The surface conductivity and hydraulic permeability values from these studies are summarized in Table 1.1 and illustrate a major

performance limitation in the ECM field that we have termed the “conductivity/ permeability trade-off.” Although not unique to HF membranes alone, these studies illustrate the need for optimization of existing fabrication protocols to achieve both high conductivity and permeability necessary for processing large volumes of water (hundreds to thousands of ML/d).

**Table 1.1.** Literature conductivity and permeability values for carbon nanotube based electrically conductive hollow fiber membranes

Reference	Support Membrane	Filtration Type	Conductivity (S/m)	Permeability (LMH/bar)
[63]	N/A	MF	1.2	12,000
[87]	PAN	UF	280	7.2
[88]	PAN (Electro spun)	MF	39	5,800

### 1.3 Conductivity/ Permeability Trade-off

#### 1.3.1 Limitations in Dead-end Conductive Membrane Fabrication

As mentioned in Section 1.2, vacuum and pressure deposition are the most common techniques for ECM fabrication. These techniques are usually conducted in dead-end filtration mode without a true understanding of how the filtration process affects particle deposition patterns. The key challenges with this approach are avoiding excess deposition of conductive material, and ensuring the deposited layer is uniform along the membrane surface. As an example, in the coatings developed by Wei et al., CNTs were deposited in a thick layer (~30  $\mu\text{m}$ ) producing relatively high conductivity and low permeability compared to the work by Du et al. with CNT layer thickness ~1.5  $\mu\text{m}$  (see Table 1.1) [87,88]. The triple order of magnitude difference in permeability between these two works is likely a factor of both this substantial difference in coating thickness as well as the separation type (MF vs UF). A further complication is the coating uniformity along a longer HF membrane. The short membrane samples (i.e. ~ 15 cm [88]) prepared in previous works are not true representations of industrial modules where HFs can be over a meter in length [6]. It is unclear if the same conductivity would be observed at all points along the fiber when scaled up. Crossflow filtration is generally preferred over dead-end in most membrane

filtration processes due to induced shear effects that prevent excess particle deposition [9,10]. We hypothesize this shear effect could be optimized to ensure uniform deposition of CNTs.

### 1.3.2 Potential for Crossflow Filtration – Application to Particle Deposition Theory

Fluid velocity profiles determine the trajectories followed by particles in flow and can be classified as laminar or turbulent depending on the ratio of inertial (due to fluid momentum) to viscous (due to fluid friction) forces. In fluid mechanics, the relative contributions of these forces can be quantified using the Reynolds number ( $Re$ ):

$$Re = \frac{\rho v D_H}{\mu} \quad (2)$$

where  $\rho$  is the solution density,  $v$  is the characteristic velocity,  $D_H$  is the hydraulic diameter and  $\mu$  is the dynamic viscosity. Using this metric, flow can be categorized as laminar ( $Re < 2300$ ), turbulent ( $Re > 4000$ ), or transitional ( $Re = 2300 - 4000$ ) [89]. In laminar flow, velocity streamlines follow a smooth, regular path whereas in turbulent flow, streamlines are mixed due to random velocity fluctuations and eddy currents. A simple system of fully developed internal laminar flow has a parabolic velocity profile with maximum velocity in the center of flow. In fully developed internal turbulent flow, velocity profiles have a blunt shape due to fluid mixing [89]. Laminar flow is the most likely profile for internal crossflow through a HF membrane given their small diameter; therefore, the following force analysis assumes laminar flow.

A particle travelling in bounded laminar crossflow along a membrane surface experiences three major forces: an inertial lift force away from the membrane wall ( $F_L$ ), a drag force in the direction of permeate flow ( $F_{D_y}$ ), and a second drag force in the direction of crossflow ( $F_{D_x}$ ) as shown in Fig 1.6a. The balance of forces in the vertical direction ( $F_L$  and  $F_{D_y}$ ) determine whether particle deposition will occur [9,10]. Once deposited, the particle experiences two further effects:

a van der Waals attractive force encouraging sustained particle attachment ( $F_{vdW}$ ) and a friction force opposing the crossflow ( $F_F$ ) as shown in Fig 1.6b. Particles will detach from the membrane surface if  $F_L$  is greater than the combined magnitude of  $F_{D_y}$  and  $F_{vdW}$  [9,10]. The initial deposition step is most significant for developing conductive HF membranes via a deposition-based process; we therefore seek a method to controllably tune inertial lift ( $F_L$ ) and permeation drag ( $F_{D_y}$ ) forces.

Permeation drag and inertial lift are both dependent on flow properties. The permeation drag force ( $F_{D_y}$ ) is directly proportional to the rate of permeation, and numerical evidence suggests that increasing permeation rate directly leads to an increase in the rate and extent of deposition [9][10]. In simple bounded flow with impermeable walls, inertial lift ( $F_L$ ) consists of two components, the net of which determines its effect on particle deposition: 1) wall-effect lift ( $F_{WE}$ ) opposing deposition and 2) shear-gradient lift ( $F_{SG}$ ) encouraging deposition [90,91]. Wall-effect lift is induced due to velocity streamline asymmetry. In unbounded flow, the velocity streamlines around a particle are symmetrical; the presence of a boundary disrupts the symmetry and diverts streamlines away from the wall. The increased velocity and resulting drop in pressure on the opposite side of the particle drives movement away from the wall, thus opposing deposition (see Fig. 1.7a) [90,91]. Shear-gradient lift is a result of the parabolic velocity profile in laminar flow which causes the magnitude of fluid velocity relative to particle velocity to differ on either side of the particle (see Fig. 1.7b). The shear-gradient induced force therefore causes the particle to move towards the side with a higher velocity magnitude and corresponding lower pressure, typically towards the wall [91–93]. The relative magnitude of wall-effect and shear-gradient lift is determined by the lateral or crossflow velocity, as well as other system parameters including viscosity, particle diameter, and hydraulic diameter [90].

Experimentally, selection of permeation rate and crossflow velocity, which directly relate to permeation drag and inertial lift, have been shown to significantly impact particle deposition patterns. Increasing permeation rate has led to an increase in the rate and extent of latex bead deposition in a forward osmosis [94] and patterned MF membrane study [95]. Uniformity in the deposited layer along the membrane surface also improved with increasing permeation rate [94,95]. The impacts of crossflow velocity in these two studies were not consistent however where in one case, increasing crossflow velocity improved the extent and uniformity of the deposited layer [95] and had the opposite effect in the other [94]. Radu et al. have speculated that increasing crossflow velocity induces two contrasting effects: 1) increased shear, which encourages particle detachment and 2) increased particle loading, which improves deposition probability [96]. These results suggest there may be an optimal combination of crossflow velocity and permeation rate where particle loading and shear can be balanced to produce a uniform, dense deposited layer.

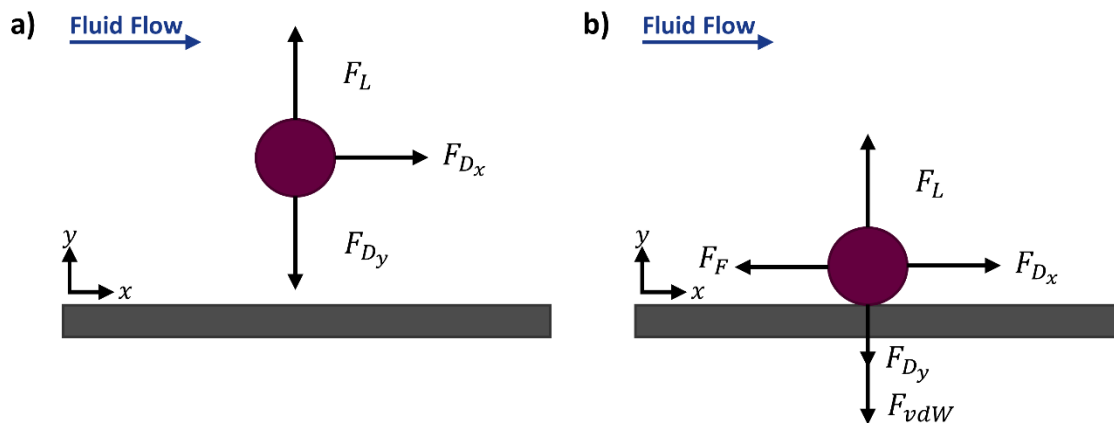


**Figure 1.6.** Free body diagram demonstrated the forces acting on **a)** a particle in flow and **b)** a deposited particle. Forces involved: lift ( $F_L$ ), drag due to permeate flow ( $F_{Dy}$ ), drag due to crossflow ( $F_{Dx}$ ), van der Waals attractive force ( $F_{vdW}$ ) and friction ( $F_F$ ).

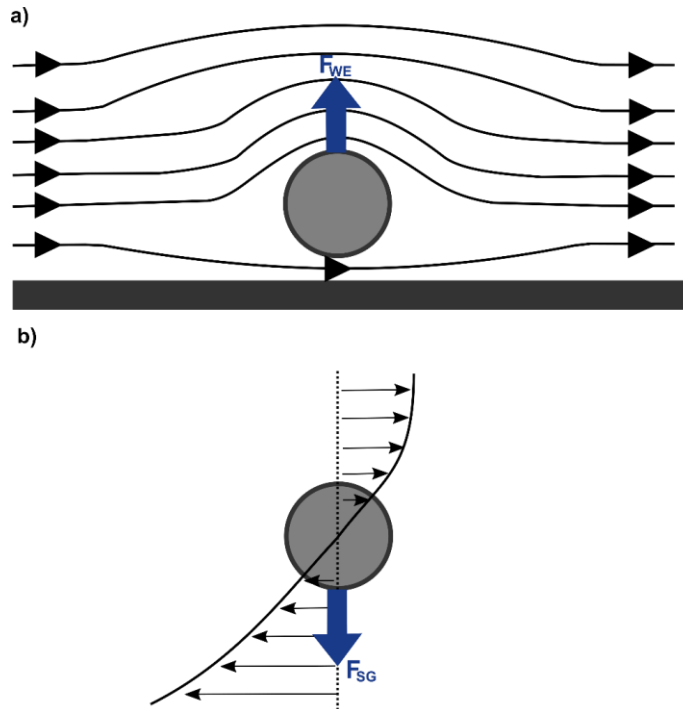


**Figure 1.7.** Schematic illustrating the two components of the inertial lift force: **a)** wall effect lift force ( $F_{WE}$ ) with velocity streamlines shown and **b)** shear-gradient lift force ( $F_{SG}$ ) with fluid velocities shown relative to the particle velocity.

#### 1.4 Motivation & Objectives

This work was motivated by the opportunity for developing conductive membranes in an industrially relevant hollow fiber (HF) format and to improve understanding of the impacts of flow parameters in deposition-based synthesis methods. The main goal of this project was to develop a method for fabricating conductive HF membranes to ensure uniform conductivity and performance along the entire fiber length. Commercial polyether sulfone hollow fiber membranes and carboxyl functionalized single walled/ double walled carbon nanotubes were used to develop these conductive HF membranes. Specific goals of the project included:

- Evaluating the validity of a “crossflow deposition” technique for fabricating uniformly conductive HF membranes and studying the impact of flow parameters on coating uniformity and membrane throughput.

- Establishing the inherent conductivity/ permeability trade-off in conductive membrane literature and comparing performance limits across the following parameters: conductive materials used in fabrication, filtration spectrum, separation configurations, and electro-functional applications.
- Demonstrating the electro-functional capability of the CNT coated HF membranes via electrochemical degradation of a model azo dye contaminant under an applied voltage in crossflow filtration.

## 1.5 References

- [1] B. Van Der Bruggen, C. Vandecasteele, T. Van Gestel, W. Doyen, R. Leysen, A review of pressure-driven membrane processes in wastewater treatment and drinking water production, *Environ. Prog.* 22 (2003) 46–56. <https://doi.org/10.1002/ep.670220116>.
- [2] M. Takht Ravanchi, T. Kaghazchi, A. Kargari, Application of membrane separation processes in petrochemical industry: a review, *Desalination*. 235 (2009) 199–244. <https://doi.org/10.1016/j.desal.2007.10.042>.
- [3] C.F. De Lannoy, D. Jassby, K. Gloe, A.D. Gordon, M.R. Wiesner, Aquatic biofouling prevention by electrically charged nanocomposite polymer thin film membranes, *Environ. Sci. Technol.* (2013) 1304–1319.
- [4] R. Van Reis, A. Zydney, Membrane separations in biotechnology, *Curr. Opin. Biotechnol.* 12 (2001) 208–211. [https://doi.org/10.1016/S0958-1669\(00\)00201-9](https://doi.org/10.1016/S0958-1669(00)00201-9).
- [5] Safe Water Technologies Inc., Filtration & Separation Spectrum, (2014). <https://www.swtwater.com/catalog/pdf/1406 - Filtration & Separation Spectrum.pdf> (accessed November 4, 2020).
- [6] J.D. Seader, E.J. Henley, D.K. Roper, *Separation Process Principles*, 3rd ed., John Wiley & Sons, Inc., 2011.
- [7] H. Verweij, Inorganic membranes, *Curr. Opin. Chem. Eng.* 1 (2012) 156–162. <https://doi.org/10.1016/j.coche.2012.03.006>.
- [8] T. Matsuura, *Synthetic Membranes and Membrane Separation Processes*, in: *Synth. Membr. Membr. Sep. Process.*, CRC Press, Inc., Boca Raton, 1994: pp. 305–341.
- [9] J. Altmann, S. Ripperger, Particle deposition and layer formation at the crossflow microfiltration, *J. Memb. Sci.* 124 (1997) 119–128. [https://doi.org/10.1016/S0376-7388\(96\)00235-9](https://doi.org/10.1016/S0376-7388(96)00235-9).
- [10] L. Song, M. Elimelech, Particle deposition onto a permeable surface in laminar flow, *J. Colloid Interface Sci.* 173 (1995) 165–180. <https://doi.org/10.1006/jcis.1995.1310>.

- [11] Synder Filtration, Module Configuration & Processes, (2020). <https://synderfiltration.com/learning-center/articles/module-configurations-process/> (accessed October 25, 2020).
- [12] L.M. Robeson, Correlation of separation factor versus permeability for polymeric membranes, *J. Memb. Sci.* 62 (1991) 165–185. [https://doi.org/10.1016/0376-7388\(91\)80060-J](https://doi.org/10.1016/0376-7388(91)80060-J).
- [13] C. Buelke, A. Alshami, J. Casler, Y. Lin, M. Hickner, I.H. Aljundi, Evaluating graphene oxide and holey graphene oxide membrane performance for water purification, *J. Memb. Sci.* 588 (2019) 117195. <https://doi.org/10.1016/j.memsci.2019.117195>.
- [14] G.M. Geise, H.B. Park, A.C. Sagle, B.D. Freeman, J.E. McGrath, Water permeability and water/salt selectivity tradeoff in polymers for desalination, *J. Memb. Sci.* 369 (2011) 130–138. <https://doi.org/10.1016/j.memsci.2010.11.054>.
- [15] A. Mehta, A.L. Zydney, Permeability and selectivity analysis for ultrafiltration membranes, *J. Memb. Sci.* 249 (2005) 245–249. <https://doi.org/10.1016/j.memsci.2004.09.040>.
- [16] W. Guo, H.H. Ngo, J. Li, A mini-review on membrane fouling, *Bioresour. Technol.* 122 (2012) 27–34. <https://doi.org/10.1016/j.biortech.2012.04.089>.
- [17] P. Watnick, R. Kolter, Biofilm, city of microbes, *J. Bacteriol.* 182 (2000) 2675–2679. <https://doi.org/10.1128/JB.182.10.2675-2679.2000>.
- [18] R.M. Donlan, Biofilms: Microbial Life on Surfaces, *Emerg. Infect. Dis.* 8 (2002) 881–890.
- [19] J.S. Baker, L.Y. Dudley, Biofouling in membrane systems - A review, *Desalination.* 118 (1998) 81–90.
- [20] C.Y. Tang, T.H. Chong, A.G. Fane, Colloidal interactions and fouling of NF and RO membranes: A review, *Adv. Colloid Interface Sci.* 164 (2011) 126–143. <https://doi.org/10.1016/j.cis.2010.10.007>.
- [21] N. Hilal, O.O. Ogunbiyi, N.J. Miles, R. Nigmatullin, N. Hilal, O.O. Ogunbiyi, N.J. Miles, R. Nigmatullin, Methods Employed for Control of Fouling in MF and UF Membranes : A Comprehensive Review, 6395 (2007). <https://doi.org/10.1081/SS-200068409>.
- [22] A. Antony, J.H. Low, S. Gray, A.E. Childress, P. Le-Clech, G. Leslie, Scale formation and control in high pressure membrane water treatment systems: A review, *J. Memb. Sci.* 383 (2011) 1–16. <https://doi.org/10.1016/j.memsci.2011.08.054>.
- [23] D. Henschler, Toxicity of Chlorinated Organic Compounds: Effects of the Introduction of Chlorine in Organic Molecules, *Angew. Chemie Int. Ed. English.* 33 (1994) 1920–1935. <https://doi.org/10.1002/anie.199419201>.
- [24] H. Ben Mansour, R. Mosrati, D. Corroler, K. Ghedira, D. Barillier, L. Chekir, In vitro mutagenicity of Acid Violet 7 and its degradation products by *Pseudomonas putida* mt-2: Correlation with chemical structures, *Environ. Toxicol. Pharmacol.* 27 (2009) 231–236. <https://doi.org/10.1016/j.etap.2008.10.008>.
- [25] G.L. Baughman, T.A. Perenich, Fate of dyes in aquatic systems: I. Solubility and

- partitioning of some hydrophobic dyes and related compounds, *Environ. Toxicol. Chem.* 7 (1988) 183–199. <https://doi.org/10.1002/etc.5620070302>.
- [26] C.B. Murphy, S.J. Spiegel, Bioaccumulation and toxicity of heavy metals and related trace elements, *J. Water Pollut. Control Fed.* 55 (1983) 816–822.
- [27] E.S.K. Chian, W.N. Bruce, H.H.P. Fang, Removal of Pesticides by Reverse Osmosis, *Environ. Sci. Technol.* 9 (1975) 52–59. <https://doi.org/10.1021/es60099a009>.
- [28] D. De Jager, M.S. Sheldon, W. Edwards, Colour removal from textile wastewater using a pilot-scale dual-stage MBR and subsequent RO system, *Sep. Purif. Technol.* 135 (2014) 135–144. <https://doi.org/10.1016/j.seppur.2014.08.008>.
- [29] N. Al-Bastaki, Removal of methyl orange dye and Na<sub>2</sub>SO<sub>4</sub> salt from synthetic waste water using reverse osmosis, *Chem. Eng. Process. Process Intensif.* 43 (2004) 1561–1567. <https://doi.org/10.1016/j.cep.2004.03.001>.
- [30] F. Fu, Q. Wang, Removal of heavy metal ions from wastewaters: A review, *J. Environ. Manage.* 92 (2011) 407–418. <https://doi.org/10.1016/j.jenvman.2010.11.011>.
- [31] S. Surawanvijit, A. Rahardianto, Y. Cohen, An Integrated approach for characterization of polyamide reverse osmosis membrane degradation due to exposure to free chlorine, *J. Memb. Sci.* 510 (2016) 164–173. <https://doi.org/10.1016/j.memsci.2016.02.044>.
- [32] M. Bagheri, S.A. Mirbagheri, Critical review of fouling mitigation strategies in membrane bioreactors treating water and wastewater, *Bioresour. Technol.* 258 (2018) 318–334. <https://doi.org/10.1016/j.biortech.2018.03.026>.
- [33] C. Psoch, S. Schiewer, Anti-fouling application of air sparging and backflushing for MBR, *J. Memb. Sci.* 283 (2006) 273–280. <https://doi.org/10.1016/j.memsci.2006.06.042>.
- [34] C. Cabassud, S. Laborie, L. Durand-Bourlier, J.M. Lainé, Air sparging in ultrafiltration hollow fibers: Relationship between flux enhancement, cake characteristics and hydrodynamic parameters, *J. Memb. Sci.* 181 (2001) 57–69. [https://doi.org/10.1016/S0376-7388\(00\)00538-X](https://doi.org/10.1016/S0376-7388(00)00538-X).
- [35] T. Jiang, H. Zhang, D. Gao, F. Dong, J. Gao, F. Yang, Fouling characteristics of a novel rotating tubular membrane bioreactor, *Chem. Eng. Process. Process Intensif.* 62 (2012) 39–46. <https://doi.org/10.1016/j.cep.2012.09.012>.
- [36] M.R. Bilad, G. Mezohegyi, P. Declerck, I.F.J. Vankelecom, Novel magnetically induced membrane vibration (MMV) for fouling control in membrane bioreactors, *Water Res.* 46 (2012) 63–72. <https://doi.org/10.1016/j.watres.2011.10.026>.
- [37] M. Xu, X. Wen, X. Huang, Z. Yu, M. Zhu, Mechanisms of membrane fouling controlled by online ultrasound in an anaerobic membrane bioreactor for digestion of waste activated sludge, *J. Memb. Sci.* 445 (2013) 119–126. <https://doi.org/10.1016/j.memsci.2013.06.006>.
- [38] H.K. Shon, S. Vigneswaran, J. Cho, Comparison of physico-chemical pretreatment methods to seawater reverse osmosis: Detailed analyses of molecular weight distribution of organic matter in initial stage, *J. Memb. Sci.* 320 (2008) 151–158. <https://doi.org/10.1016/j.memsci.2008.03.063>.

- [39] R. Zhang, Y. Liu, M. He, Y. Su, X. Zhao, M. Elimelech, Z. Jiang, Antifouling membranes for sustainable water purification: Strategies and mechanisms, *Chem. Soc. Rev.* 45 (2016) 5888–5924. <https://doi.org/10.1039/c5cs00579e>.
- [40] B.D. McCloskey, H.B. Park, H. Ju, B.W. Rowe, D.J. Miller, B.D. Freeman, A bioinspired fouling-resistant surface modification for water purification membranes, *J. Memb. Sci.* 413–414 (2012) 82–90. <https://doi.org/10.1016/j.memsci.2012.04.021>.
- [41] S. Sommer, A. Ekin, D.C. Webster, S.J. Stafslie, J. Daniels, L.J. VanderWal, S.E.M. Thompson, M.E. Callow, J.A. Callow, A preliminary study on the properties and fouling-release performance of siloxane-polyurethane coatings prepared from poly(dimethylsiloxane) (PDMS) macromers., *Biofouling*. 26 (2010) 961–972. <https://doi.org/10.1080/08927014.2010.531272>.
- [42] R. Guha, B. Xiong, M. Geitner, T. Moore, T.K. Wood, D. Velegol, M. Kumar, Reactive micromixing eliminates fouling and concentration polarization in reverse osmosis membranes, *J. Memb. Sci.* 542 (2017) 8–17. <https://doi.org/10.1016/j.memsci.2017.07.044>.
- [43] S.H. Kim, S.Y. Kwak, B.H. Sohn, T.H. Park, Design of TiO<sub>2</sub> nanoparticle self-assembled aromatic polyamide thin-film-composite (TFC) membrane as an approach to solve biofouling problem, *J. Memb. Sci.* 211 (2003) 157–165. [https://doi.org/10.1016/S0376-7388\(02\)00418-0](https://doi.org/10.1016/S0376-7388(02)00418-0).
- [44] J. Huang, Z. Wang, J. Zhang, X. Zhang, J. Ma, Z. Wu, A novel composite conductive microfiltration membrane and its anti-fouling performance with an external electric field in membrane bioreactors, *Sci. Rep.* 5 (2015) 1–8. <https://doi.org/10.1038/srep09268>.
- [45] S.Y. Yang, C.D. Vecitis, H. Park, Electrocatalytic water treatment using carbon nanotube filters modified with metal oxides, *Environ. Sci. Pollut. Res.* 26 (2019) 1036–1043. <https://doi.org/10.1007/s11356-017-8495-6>.
- [46] T. Robinson, G. McMullan, R. Marchant, P. Nigam, Remediation of dyes in textile effluent: a critical review on current treatment technologies with a proposed alternative, *Bioresour. Technol.* (2001) 247–255. <https://doi.org/10.1504/IJEP.2004.004190>.
- [47] C.A. Martínez-Huitle, E. Brillas, Decontamination of wastewaters containing synthetic organic dyes by electrochemical methods: A general review, *Appl. Catal. B Environ.* 87 (2009) 105–145. <https://doi.org/10.1016/j.apcatb.2008.09.017>.
- [48] C. Lei, F. Liang, J. Li, W. Chen, B. Huang, Electrochemical reductive dechlorination of chlorinated volatile organic compounds (Cl-VOCs): Effects of molecular structure on the dehalogenation reactivity and mechanisms, *Chem. Eng. J.* 358 (2019) 1054–1064. <https://doi.org/10.1016/j.cej.2018.10.105>.
- [49] C.D. Vecitis, G. Gao, H. Liu, Electrochemical carbon nanotube filter for adsorption, desorption, and oxidation of aqueous dyes and anions, *J. Phys. Chem. C.* 115 (2011) 3621–3629. <https://doi.org/10.1021/jp111844j>.
- [50] F.R. Omi, M.R. Choudhury, N. Anwar, A.R. Bakr, M.S. Rahaman, Highly Conductive Ultrafiltration Membrane via Vacuum Filtration Assisted Layer-by-Layer Deposition of Functionalized Carbon Nanotubes, *Ind. Eng. Chem. Res.* 56 (2017) 8474–8484.

<https://doi.org/10.1021/acs.iecr.7b00847>.

- [51] A.J. Sutherland, M.X. Ruiz-Caldas, C.F. de Lannoy, Electro-catalytic microfiltration membranes electrochemically degrade azo dyes in solution, *J. Memb. Sci.* 611 (2020) 118335. <https://doi.org/10.1016/j.memsci.2020.118335>.
- [52] W. Duan, G. Chen, C. Chen, R. Sanghvi, A. Iddya, S. Walker, H. Liu, A. Ronen, D. Jassby, Electrochemical removal of hexavalent chromium using electrically conducting carbon nanotube/polymer composite ultrafiltration membranes, *J. Memb. Sci.* 531 (2017) 160–171. <https://doi.org/10.1016/j.memsci.2017.02.050>.
- [53] Y. Liu, J.H. Dustin Lee, Q. Xia, Y. Ma, Y. Yu, L.Y. Lanry Yung, J. Xie, C.N. Ong, C.D. Vecitis, Z. Zhou, A graphene-based electrochemical filter for water purification, *J. Mater. Chem. A* 2 (2014) 16554–16562. <https://doi.org/10.1039/c4ta04006f>.
- [54] C.F. de Lannoy, D. Jassby, K. Gloe, A.D. Gordon, M.R. Wiesner, Aquatic biofouling prevention by electrically charged nanocomposite polymer thin film membranes, *Environ. Sci. Technol.* 47 (2013) 2760–2768. <https://doi.org/10.1021/es3045168>.
- [55] A. Ronen, W. Duan, I. Wheeldon, S. Walker, D. Jassby, Microbial Attachment Inhibition through Low-Voltage Electrochemical Reactions on Electrically Conducting Membranes, *Environ. Sci. Technol.* 49 (2015) 12741–12750. <https://doi.org/10.1021/acs.est.5b01281>.
- [56] B.S. Lalia, F.E. Ahmed, T. Shah, N. Hilal, R. Hashaikeh, Electrically conductive membranes based on carbon nanostructures for self-cleaning of biofouling, *Desalination* 360 (2015) 8–12. <https://doi.org/10.1016/j.desal.2015.01.006>.
- [57] Q. Zhang, C.D. Vecitis, Conductive CNT-PVDF membrane for capacitive organic fouling reduction, *J. Memb. Sci.* 459 (2014) 143–156. <https://doi.org/10.1016/j.memsci.2014.02.017>.
- [58] A. V. Dudchenko, J. Rolf, K. Russell, W. Duan, D. Jassby, Organic fouling inhibition on electrically conducting carbon nanotube-polyvinyl alcohol composite ultrafiltration membranes, *J. Memb. Sci.* 468 (2014) 1–10. <https://doi.org/10.1016/j.memsci.2014.05.041>.
- [59] W. Duan, A. Dudchenko, E. Mende, C. Flyer, X. Zhu, D. Jassby, Electrochemical Mineral Scale Prevention and Removal on Electrically Conducting Carbon Nanotube - Polyamide Reverse Osmosis Membranes, *Environ. Sci. Process. Impacts* 16 (2014) 1300–1308. <https://doi.org/10.31729/jnma.1240>.
- [60] L. Zhang, Y. Zhang, X. Zhang, Z. Li, G. Shen, M. Ye, C. Fan, H. Fang, J. Hu, Electrochemically controlled formation and growth of hydrogen nanobubbles, *Langmuir* 22 (2006) 8109–8113. <https://doi.org/10.1021/la060859f>.
- [61] N. Zhang, M.A. Halali, C.F. de Lannoy, Detection of fouling on electrically conductive membranes by electrical impedance spectroscopy, *Sep. Purif. Technol.* 242 (2020) 116823. <https://doi.org/10.1016/j.seppur.2020.116823>.
- [62] F.E. Ahmed, N. Hilal, R. Hashaikeh, Electrically conductive membranes for in situ fouling detection in membrane distillation using impedance spectroscopy, *J. Memb. Sci.* 556 (2018) 66–72. <https://doi.org/10.1016/j.memsci.2018.03.069>.

- [63] G. Wei, S. Chen, X. Fan, X. Quan, H. Yu, Carbon nanotube hollow fiber membranes: High-throughput fabrication, structural control and electrochemically improved selectivity, *J. Memb. Sci.* 493 (2015) 97–105. <https://doi.org/10.1016/j.memsci.2015.05.073>.
- [64] H. Zhang, X. Quan, X. Fan, G. Yi, S. Chen, H. Yu, Y. Chen, Improving Ion Rejection of Conductive Nanofiltration Membrane through Electrically Enhanced Surface Charge Density, *Environ. Sci. Technol.* 53 (2019) 868–877. <https://doi.org/10.1021/acs.est.8b04268>.
- [65] P. Gayen, C. Chen, J.T. Abiade, B.P. Chaplin, Electrochemical Oxidation of Atrazine and Clothianidin on Bi-doped SnO<sub>2</sub>-TiO<sub>2</sub>n-1 Electrocatalytic Reactive Electrochemical Membranes, *Environ. Sci. Technol.* 52 (2018) 12675–12684. <https://doi.org/10.1021/acs.est.8b04103>.
- [66] W. Duan, G. Chen, C. Chen, R. Sanghvi, A. Iddya, S. Walker, H. Liu, A. Ronen, D. Jassby, Electrochemical removal of hexavalent chromium using electrically conducting carbon nanotube/polymer composite ultrafiltration membranes, *J. Memb. Sci.* 531 (2017) 160–171. <https://doi.org/10.1016/j.memsci.2017.02.050>.
- [67] M. Graymore, F. Stagnitti, G. Allinson, Impacts of atrazine in aquatic ecosystems, *Environ. Int.* 26 (2001) 483–495. [https://doi.org/10.1016/S0160-4120\(01\)00031-9](https://doi.org/10.1016/S0160-4120(01)00031-9).
- [68] L. Guo, Y. Jing, B.P. Chaplin, Development and Characterization of Ultrafiltration TiO<sub>2</sub> Magnéli Phase Reactive Electrochemical Membranes, *Environ. Sci. Technol.* 50 (2016) 1428–1436. <https://doi.org/10.1021/acs.est.5b04366>.
- [69] W. Yang, M. Son, R. Rossi, J.S. Vrouwenvelder, B.E. Logan, Adapting Aluminum-Doped Zinc Oxide for Electrically Conductive Membranes Fabricated by Atomic Layer Deposition, *ACS Appl. Mater. Interfaces.* 12 (2020) 963–969. <https://doi.org/10.1021/acsami.9b20385>.
- [70] M.C. Santos, Y.A. Elabd, Y. Jing, B.P. Chaplin, L. Fang, Highly Porous TiO<sub>2</sub> Reactive Electrochemical Water Filtration Membranes Fabricated via Electrospinning/Electrospraying, *AIChE J.* 62 (2015) 508–524. <https://doi.org/10.1002/aic>.
- [71] T. Mantel, P. Benne, S. Parsin, M. Ernst, Electro-conductive composite gold-polyethersulfone-ultrafiltration-membrane: Characterization of membrane and natural organic matter (NOM) filtration performance at different in-situ applied surface potentials, *Membranes (Basel)*. 8 (2018). <https://doi.org/10.3390/membranes8030064>.
- [72] D. Bell, R. Sengpiel, M. Wessling, Metallized hollow fiber membranes for electrochemical fouling control, *J. Memb. Sci.* 594 (2020) 117397. <https://doi.org/10.1016/j.memsci.2019.117397>.
- [73] D. Liu, X. Chen, B. Bian, Z. Lai, Y. Situ, Dual-Function Conductive Copper Hollow Fibers for Microfiltration and Anti-biofouling in Electrochemical Membrane Bioreactors, *Front. Chem.* 6 (2018) 1–10. <https://doi.org/10.3389/fchem.2018.00445>.
- [74] J. Liu, C. Tian, J. Xiong, B. Gao, S. Dong, L. Wang, Polypyrrole vapor phase polymerization on PVDF membrane surface for conductive membrane preparation and fouling mitigation, *J. Chem. Technol. Biotechnol.* 93 (2018) 683–689.

<https://doi.org/10.1002/jctb.5416>.

- [75] W. Duan, A. Ronen, S. Walker, D. Jassby, Polyaniline-Coated Carbon Nanotube Ultrafiltration Membranes: Enhanced Anodic Stability for in Situ Cleaning and Electro-Oxidation Processes, *ACS Appl. Mater. Interfaces*. 8 (2016) 22574–22584. <https://doi.org/10.1021/acsami.6b07196>.
- [76] R. Rohani, I.I. Yusoff, Towards electrically tunable nanofiltration membranes: polyaniline-coated polyvinylidene fluoride membranes with tunable permeation properties, *Iran. Polym. J. (English Ed)*. 28 (2019) 789–800. <https://doi.org/10.1007/s13726-019-00744-0>.
- [77] C.F. de Lannoy, D. Jassby, D.D. Davis, M.R. Wiesner, A highly electrically conductive polymer-multiwalled carbon nanotube nanocomposite membrane, *J. Memb. Sci.* 415–416 (2012) 718–724. <https://doi.org/10.1016/j.memsci.2012.05.061>.
- [78] H. Farrokhzad, T. Van Gerven, B. Van Der Bruggen, Preparation and characterization of a conductive polyaniline/polysulfone film and evaluation of the effect of co-solvent, *Eur. Polym. J.* 49 (2013) 3234–3243. <https://doi.org/10.1016/j.eurpolymj.2013.06.027>.
- [79] N. Fakhri, D.A. Tsyboulski, L. Cognet, R. Bruce Weisman, M. Pasquali, Diameter-dependent bending dynamics of single-walled carbon nanotubes in liquids, *Proc. Natl. Acad. Sci. U. S. A.* 106 (2009) 14219–14223. <https://doi.org/10.1073/pnas.0904148106>.
- [80] H. Kim, Y.S. Hwang, V.K. Sharma, Adsorption of antibiotics and iopromide onto single-walled and multi-walled carbon nanotubes, *Chem. Eng. J.* 255 (2014) 23–27. <https://doi.org/10.1016/j.cej.2014.06.035>.
- [81] P. Xie, C.F. de Lannoy, J. Ma, Z. Wang, S. Wang, J. Li, M.R. Wiesner, Improved chlorine tolerance of a polyvinyl pyrrolidone-polysulfone membrane enabled by carboxylated carbon nanotubes, *Water Res.* 104 (2016) 497–506. <https://doi.org/10.1016/j.watres.2016.08.029>.
- [82] B. Hinds, Dramatic transport properties of carbon nanotube membranes for a robust protein channel mimetic platform, *Curr. Opin. Solid State Mater. Sci.* 16 (2012) 1–9. <https://doi.org/10.1016/j.cossms.2011.05.003>.
- [83] A. Ronen, W. Duan, I. Wheeldon, S. Walker, D. Jassby, Microbial Attachment Inhibition through Low-Voltage Electrochemical Reactions on Electrically Conducting Membranes, *Environ. Sci. Technol.* 49 (2015) 12741–12750. <https://doi.org/10.1021/acs.est.5b01281>.
- [84] K.G. Dassios, P. Alafogianni, S.K. Antiohos, C. Leptokaridis, N.M. Barkoula, T.E. Matikas, Optimization of sonication parameters for homogeneous surfactant assisted dispersion of multiwalled carbon nanotubes in aqueous solutions, *J. Phys. Chem. C*. 119 (2015) 7506–7516. <https://doi.org/10.1021/acs.jpcc.5b01349>.
- [85] M.A. Halali, C.F. De Lannoy, The Effect of Cross-Linkers on the Permeability of Electrically Conductive Membranes, *Ind. Eng. Chem. Res.* 58 (2019) 3832–3844. <https://doi.org/10.1021/acs.iecr.8b05691>.
- [86] K. Goh, L. Setiawan, L. Wei, W. Jiang, R. Wang, Y. Chen, Fabrication of novel functionalized multi-walled carbon nanotube immobilized hollow fiber membranes for enhanced performance in forward osmosis process, *J. Memb. Sci.* 446 (2013) 244–254.

- <https://doi.org/10.1016/j.memsci.2013.06.022>.
- [87] G. Wei, J. Dong, J. Bai, Y. Zhao, Y. Li, Structurally Stable, Antifouling, and Easily Renewable Reduced Graphene Oxide Membrane with a Carbon Nanotube Protective Layer, *Environ. Sci. Technol.* 53 (2019) 11896–11903. <https://doi.org/10.1021/acs.est.9b03129>.
- [88] L. Du, X. Quan, X. Fan, G. Wei, S. Chen, Conductive CNT/nanofiber composite hollow fiber membranes with electrospun support layer for water purification, *J. Memb. Sci.* 596 (2020) 117613. <https://doi.org/10.1016/j.memsci.2019.117613>.
- [89] P.J. Pritchard, J.W. Mitchell, Fox and McDonald's Introduction to Fluid Mechanics, 9th ed., John Wiley & Sons, Inc., 2015.
- [90] D. Di Carlo, Inertial microfluidics, *Lab Chip.* 9 (2009) 3038–3046. <https://doi.org/10.1039/b912547g>.
- [91] J.M. Martel, M. Toner, Inertial Focusing in Microfluidics, *Annu. Rev. Biomed. Eng.* 16 (2014) 371–396. <https://doi.org/10.1146/annurev-bioeng-121813-120704>.
- [92] Y. Gou, Y. Jia, P. Wang, C. Sun, Progress of inertial microfluidics in principle and application, *Sensors (Switzerland)*. 18 (2018). <https://doi.org/10.3390/s18061762>.
- [93] J. Zhang, S. Yan, D. Yuan, G. Alici, N.T. Nguyen, M. Ebrahimi Warkiani, W. Li, Fundamentals and applications of inertial microfluidics: A review, *Lab Chip.* 16 (2016) 10–34. <https://doi.org/10.1039/c5lc01159k>.
- [94] A. Bogler, A. Kastl, M. Spinnler, T. Sattelmayer, A. Be'er, E. Bar-Zeev, Where, when and why? Quantifying the relation of particle deposition to crossflow velocity and permeate water flux in forward osmosis, *J. Memb. Sci.* 604 (2020) 118055. <https://doi.org/10.1016/j.memsci.2020.118055>.
- [95] D.C. Choi, S.Y. Jung, Y.J. Won, J.H. Jang, J. Lee, H.R. Chae, K.H. Ahn, S. Lee, P.K. Park, C.H. Lee, Three-dimensional hydraulic modeling of particle deposition on the patterned isopore membrane in crossflow microfiltration, *J. Memb. Sci.* 492 (2015) 156–163. <https://doi.org/10.1016/j.memsci.2015.05.054>.
- [96] A.I. Radu, M.S.H. van Steen, J.S. Vrouwenvelder, M.C.M. van Loosdrecht, C. Picioreanu, Spacer geometry and particle deposition in spiral wound membrane feed channels, *Water Res.* 64 (2014) 160–176. <https://doi.org/10.1016/j.watres.2014.06.040>.

## **Chapter 2: Formation of electrically conductive hollow fiber membranes via crossflow deposition of carbon nanotubes – addressing the conductivity/ permeability trade-off**

Authors: Melissa J. Larocque, David R. Latulippe, Charles-François de Lannoy

Copyright 2020 Elsevier B. V.

Accepted for Publication, Journal of Membrane Science

<https://doi.org/10.1016/j.memsci.2020.118859>

### **2.1 Preface**

In this chapter, a “crossflow deposition” technique was developed for fabricating electrically conductive membranes (ECMs) in a hollow fiber (HF) format. As outlined in Chapter 1, previous ECM research has been largely limited to flat sheet format, suitable for lab-scale studies, while other formats such as HF are preferred in industry for their high packing density. Furthermore, deposition-based synthesis methods typically employ dead-end filtration without considering the impact of flow parameters on deposition patterns. The “crossflow deposition” technique developed in this chapter allowed for manipulation of flow parameters, such as feed pressure and crossflow velocity, to control deposition behaviour. Single walled/ double walled carbon nanotubes (SW/DWCNTs) were filtered in crossflow along the interior, active surface of polyether sulfone (PES) HF membranes to create a uniformly deposited CNT layer. The effects of feed pressure and crossflow velocity on composite membrane performance in terms of surface conductivity and hydraulic permeability were studied in a design-of-experiments model. The results in this chapter clearly show: 1) the usefulness of the “crossflow deposition” approach for controlling conductive membrane properties; 2) flow parameters (feed pressure, crossflow velocity) as well as particle loading (i.e. CNT concentration) significantly impacted composite membrane performance; 3) a

trade-off exists between surface conductivity and permeability across the various coating conditions studied. This conductivity/ permeability trade-off is further explored in Chapter 3, extending the analysis to the entire field of ECMs across various conductive materials, separation types, configurations, and applications. The electro-functional capability of the CNT-coated HF membranes developed in this chapter is evaluated further in Chapter 4 for their ability to electrochemically degrade a model contaminant under an applied potential.

A dead-end deposition technique was employed prior to the work in this chapter for two membrane materials: PES and polyvinylidene fluoride (PVDF). In these preliminary studies, a non-constant surface conductivity along the length of the fibers was noted, as well as the poor physical stability of coatings developed for the PVDF membranes (see Appendix A.1). This motivated the use of a crossflow technique to improve coating uniformity as well as selection of the PES HF membranes for use in this chapter. One limitation of the crossflow technique is that the theoretical deposited mass of CNTs could not be calculated since it is possible that not all CNTs present in the feed solution are deposited. Several techniques for estimating CNT concentration in solution (i.e. total organic carbon, UV-Vis-NIR absorbance) and for estimating CNT mass directly (i.e. thermogravimetric analysis) or through surrogate techniques (i.e. correlation with surface conductivity) were investigated in Appendix A.2. None of these quantification techniques were applicable for our purpose however due to the low concentrations of SW/DWCNTs and confounding effects due to presence of impurities in the samples.

## **2.2 Abstract**

Electrically conductive membranes (ECMs) have significant potential for enhanced membrane separations. While most of the existing studies on ECMs have focused on flat sheet membranes, it is the hollow fiber membrane format that is the preferred format for large-scale

treatment applications. While ECMs in hollow fiber format are emerging, existing approaches tend towards extremes of membrane conductivity or permeability without considering the trade-off between these metrics. We aim to understand and optimize this trade-off by studying the effect of the normal (pressure, lift) and tangential (shear) forces associated with conductive coating deposition. A suspension of functionalized single walled/double walled carbon nanotubes (SW/DWCNTs) in solution containing sodium dodecyl sulfate and polyvinyl alcohol was pressure deposited in crossflow along the active lumen surface of polyether sulfone microfiltration membranes. The impact of the crossflow deposition parameters affecting surface forces (feed pressure, crossflow velocity) were quantified according to both membrane permeability and conductivity in a  $2^2$  design-of-experiments study. Unexpectedly, the highest membrane permeability (~2900 LMH/bar) and conductivity (~670 S/m) and were obtained at the high feed pressure and high crossflow velocity condition. A Robeson-like plot was generated that demonstrates a trade-off between composite membrane permeability and conductivity for 29 CNT-coated HF membranes fabricated at various SW/DWCNT concentrations, crossflow velocities, and applied pressures. Measured conductivities (up to 2500 S/m) and permeabilities (up to 6000 LMH/bar) for the CNT-coated HF membranes were several orders of magnitude higher than previous conductive hollow fibers, indicating the substantial benefits of crossflow deposition. The electrically conductive hollow fiber membrane fabrication technique developed herein will be useful in a variety of conductive membrane applications including fouling prevention, enhanced removal of charged particles, and integrated membrane sensing capabilities.

### **2.3 Introduction**

Electrically conductive membranes (ECMs) have significant potential for enhancing membrane separation capability [1], coupling reactions and catalysis with separations [2], limiting

surface fouling [3], and providing surface sensing capabilities [4]. Membrane separations traditionally based on size exclusion (e.g. microfiltration (MF) or ultrafiltration (UF) membranes) can benefit from enhanced charged particle separation with electrostatic repulsive effects. The conducting surface also creates potential for redox reactions that can be exploited for specialized contaminant removal or degradation (e.g. azo dyes and chlorinated organic compounds [2], hexavalent chromium [5], phenol [6] [7], tetracycline [7]). ECMs have also been shown to mitigate the degree of fouling in applications involving biofouling [8–11], organic fouling [3,11,12], and scaling [13]. Several mechanisms have been proposed to explain this anti-fouling effect including the generation of reactive oxygen species (e.g. hydroxyl radicals) via water splitting [6], electrostatic repulsion from the charged surface [14], and steric repulsion due to the generation of gas bubbles [15]. A recent study demonstrated the usefulness of combining ECMs with electrical impedance spectroscopy to identify the onset of membrane surface fouling [4].

A major limitation of current ECM development is its nearly exclusive focus on flat sheet membranes. Other membrane formats are often preferred in industrial applications to maximize packing density and separation capacity. Hollow fiber (HF) membranes offer a significant improvement in packing density over flat sheet membranes; however, their small (~ 1 mm) diameter increases susceptibility to pore blockage and fouling [16,17]. Therefore, there is significant industrial opportunity for antifouling ECMs in a HF format.

To this end, conductive HF membranes have previously been developed with a range of conductive materials including metals (titanium oxide [18], platinum [19], nickel [20,21], copper [22]), nanomaterials (CNTs [1,23–27], graphene [28]) and polymers (polypyrrole [29,30]). Metal coatings have been recently studied due to their deposition uniformity and low thickness, however current fabrication processes have several limitations including energy intensive metallic sintering

and reduction steps at high temperature ( $>500$  °C) [18,21,22], use of hazardous reducing agents (e.g. sodium borohydride [20]) or use of specialized equipment such as atomic layer deposition [19]. Conductive polymers such as polypyrrole [29,30] or polyaniline [31] have been studied however they are difficult to cast, requiring vapour phase polymerization [29,30] or use of co-solvents [31] to overcome their poor solubility. To date the most common electrically conductive coatings are formed from graphitic nanomaterials. Carbon nanotubes (CNTs) are a promising candidate for the formation of ECMs due mostly to their high conductivity and wide range of chemical functionalizations; additional benefits to using CNTs include their capability for facilitating electrochemical redox reactions [5], high capacity for contaminant adsorption [32], and high chlorine tolerance [33].

CNT-based membranes in flat sheet format have been fabricated using two major approaches: 1) self-supporting CNT networks; 2) CNT-based composites with traditional membrane materials. Self-supporting CNT membranes offer enhanced flux and rejection for small-scale separations such as for biomolecule purification; however, these membranes are not yet practical for large-scale treatment applications due to limited pore control and high costs associated with large quantities of nanomaterials [34]. Composite materials have been developed via surface deposition of conductive nanomaterials including CNTs [12,35] and graphene [7,36] onto a support membrane. Use of a traditional membrane polymer as a support is advantageous as these materials have established large-scale fabrication protocols and methods for pore control. Combining single walled/double walled CNTs with chemical cross-linkers, direct vacuum deposition can be used to deposit a porous, cross-linked CNT network onto polymeric support membranes that achieves high surface conductivity and preserves membrane flux [37].

There has been some recent progress towards the development of CNT-based conductive HF membranes. Wei et al., [1] developed an alternative fabrication approach based on multi-walled CNTs (MWCNTs) cast directly into a HF structure via a wet-spinning technique. The reported pore size of these membranes was approximately 100 nm. These same membranes were used in a subsequent membrane bioreactor study for municipal wastewater and shown to have good anti-fouling properties with complete flux recovery after 1 h of electrochemical cleaning [24]. While highly effective for specific charged particle separations, these direct-cast CNT membranes offer limited pore control that may hinder their size exclusion separation capabilities, and have thus far yielded conductivities 1-2 orders of magnitude lower ( $\sim 1.2$  S/m [1]) than those achievable with a deposition approach. The majority of previous studies have used the simpler technique of depositing CNTs onto the surface of prefabricated HF membranes. Goh et al., [23] used a vacuum deposition approach to adhere a thin layer of MWCNTs to the exterior surface of a poly(amide-imide) HF support that was then chemically crosslinked with polyethyleneimine. These composite HF membranes were developed for forward osmosis processes. The presence of MWCNTs greatly enhanced pure water permeability and magnesium chloride salt flux; however, only these passive properties were evaluated. Further characterization of this material is required to determine potential benefits from electrochemical effects, such as enhanced charged particle removal, under an applied potential. Wei et al. [25] extended the vacuum deposition approach to two layers of nanomaterials to enhance the physical stability of the ECMs. Using a thin reduced graphene oxide layer (48 nm) followed by a thicker MWCNT layer ( $\sim 30$   $\mu\text{m}$ ) on the exterior surface of polyacrylonitrile (PAN) HF membranes proved to withstand the electrochemically assisted backwash conditions to enhance flux recovery with humic acid and methyl blue dye as model contaminants. However, the excess deposition of conductive material in this work resulted in poor

overall flux and does not consider the trade-off between membrane conductivity and permeability. Du et al. [26] achieved similar anti-fouling effects with three orders of magnitude greater flux than Wei et al. [25] in a surface water application by depositing MWCNTs onto an electrospun PAN support layer. The electrospinning process created a PAN support with low tortuosity and high porosity, enabling a high flux in comparison to membranes fabricated by phase inversion; however, the scalability of electrospinning is a significant challenge that needs to be overcome. Additionally, the reported conductivities of these HF membranes prepared both by vacuum deposition and direct wet-spinning are several orders of magnitude lower than that which has been achieved to date with flat-sheet membrane geometries. Thus, there is a clear need to revise and optimize the fabrication protocols used for conductive HF membranes to achieve the required conductivity and permeability properties that are needed to process industrially relevant volumes of water on the order of hundreds to thousands ML/day.

To optimize the trade-off between ECM conductivity and permeability, we propose the use of a “crossflow deposition” process to control the amount of CNTs on the HF membrane surface. Based on both simulation studies [38,39] and experimental studies [40,41], it is well known that crossflow filtration is an efficient method for controlling particle deposition on a membrane surface. We hypothesize that by adjusting these flow parameters, we can precisely control the deposition of dispersed CNTs to form a conductive layer onto a HF membrane surface and that this controlled deposition approach will enable optimization of the membrane performance. In this work, we used a design-of-experiments study to evaluate the effects of applied pressure and crossflow velocity on membrane permeability and conductivity. Additionally, we studied a range of parameters to identify the limits in the permeability-conductivity trade-off and generated a Robeson-like plot to identify the upper bound for ECM performance.

## 2.4 Experimental

### 2.4.1 Materials

Polyether sulfone (PES) MF membranes with a nominal pore size of 0.2  $\mu\text{m}$  were purchased from Repligen; the inner and outer diameters were measured to be approximately 1 and 1.1 mm respectively via scanning electron microscopy (SEM). Carboxyl functionalized single walled/double walled CNTs (SW/DW-CNTs) were purchased from Cheap Tubes; the properties reported by the manufacturer include the following: outer diameter of 1–4 nm, length of 5–30  $\mu\text{m}$ , purity greater than 90% (by weight), functional content of 2.73% (by weight), and ash content less than 1.5% (by weight). Sodium dodecyl sulfate (SDS, MW: 288.38 Da) was purchased from Anachemia and polyvinyl alcohol (PVA, MW: 13–23 kDa, 98-99% hydrolyzed) was purchased from Sigma Aldrich. In one of our previous studies [37], a higher MW of PVA was used in a similar recipe to create flat-sheet ECMs; the lower MW PVA was selected for this study to facilitate its dissolution in water.

### 2.4.2 Carbon Nanotube Suspension Preparation

SW/DWCNT suspensions were prepared according to a similar protocol that was developed for the fabrication of flat sheet ECMs [37]. Briefly, a suspension of SW/DWCNTs in de-ionized (DI) water was stirred for 10 minutes (600 RPM) and then ultrasonicated (QSonica Model Q500 with a ¼" microtip and 80  $\mu\text{m}$  amplitude) for 30 minutes with intervals of 2 seconds on and 2 seconds off (i.e. an effective time of 15 minutes). Excessive heating was limited by placing the suspension in an ice bath during sonication. A solution of SDS in DI water was prepared by stirring for 30 minutes (600 RPM). The SDS solution was mixed and stirred with the sonicated SW/DWCNT suspension for 15 minutes (600 RPM) then ultrasonicated for an effective time of 30 minutes with the same sonication settings and time intervals as above. A solution of PVA in DI

water was prepared by stirring for 30 minutes (600 RPM, 90°C). The mass ratios of SW/DWCNT to SDS and to PVA were maintained constant at 1:1.5 and 1:10, respectively. The PVA solution was cooled to room temperature, mixed with the SW/DWCNT-SDS suspension and ultrasonicated for an effective time of 15 minutes with the same sonication settings and time intervals as above. SW/DWCNT suspensions were used for deposition within 1–2 h after preparation and remained stable and well-dispersed in this time. Experiments were completed with two SW/DWCNT-SDS-PVA suspension concentrations: 1) 7.5 mg/L SW/DWCNTs, 11.3 mg/L SDS, 75 mg/L PVA; 2) 18.8 mg/L SW/DWCNTs, 28.1 mg/L SDS, 188 mg/L PVA. A control suspension without CNTs was also prepared with 131 mg/L PVA and 19.7 mg/L SDS.

#### 2.4.3 *Crossflow Deposition Experiments*

SW/DWCNTs were deposited in crossflow along the interior, active surface of the PES HF membranes. Crossflow deposition experiments were conducted using three custom-made modules arranged in parallel to allow for three HF membranes, each sealed within a separate module, to be made and tested with the same feed suspension (Fig. 2.1a). The module consisted of an aluminum reservoir with ports for feed, retentate and permeate lines. Crossflow deposition was conducted in an inside-out flow path due to the asymmetry of the support HF membranes. CNTs have exhibited antifouling properties both in their inherent (uncharged) form [42] and when charged in a surface coating [3], provided the CNTs are accessible to the feed. Given the inside-out asymmetry of the PES membranes, the active (interior) surface must be conductive to exhibit the strongest potential for electro-functional effects as this surface is exposed to the feed. To accommodate the inside-out configuration, feed and retentate ports were located at opposite ends of the membrane, and the permeate port was located inside the module wall. PES HF membranes were sealed in the crossflow module at the feed and retentate ports using epoxy resin (LePage Speed Set Epoxy) in a

short piece (~2 cm) of plastic tubing that was dried for 1 h at ambient temperature until it was set. The total membrane length used for sealing was 20 cm; however, the effective membrane length available for separation was approximately 16 cm, with the remaining 4 cm sealed in epoxy resin. Modules were then filled with DI water to condition the PES HF membranes overnight (12–24 h). A peristaltic pump (Masterflex Model 7523-20) was used to supply the feed, with feed pressure measured and recorded every 3 seconds via a USB transducer (Omega PX409). A needle valve on the retentate line was used to throttle crossflow velocity which was further verified via a rotameter (Omega FL3635G, 65 mm). By closing the needle valve, the system could be operated in dead-end mode. Three-way stopcock valves were used to redirect flow on the retentate lines such that the crossflow velocity for each HF could be verified independently via the rotameter. The permeate for one of the three HF membranes was collected onto a digital scale where mass was recorded every 30 seconds via a serial-USB connection to a computer to measure flow rate. Permeate flow rates for the other two HF membranes were manually collected every 15 minutes and weighed to verify that the flow rate was identical across all three membranes.

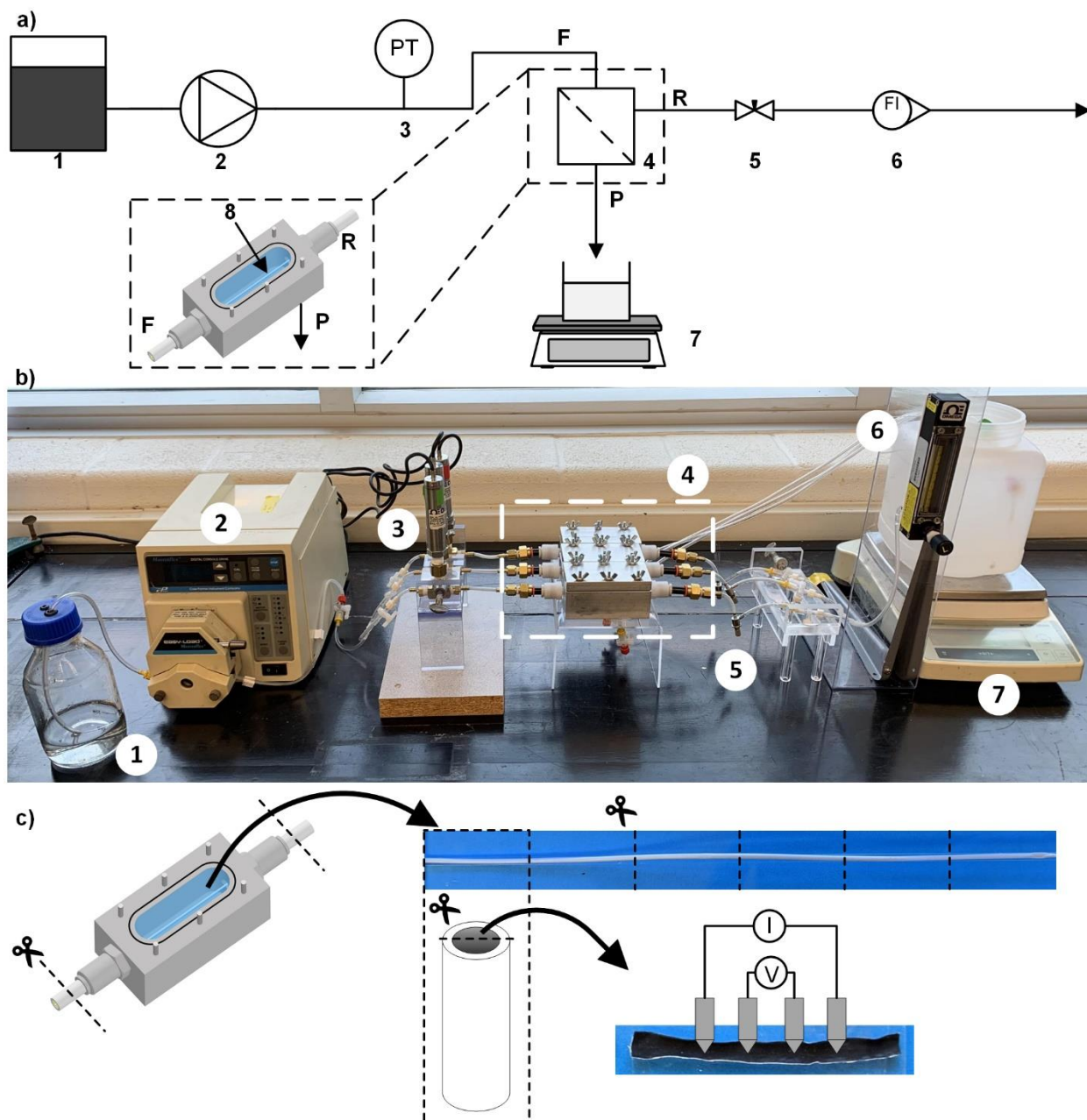


**Figure 2.1** a) Schematic of the crossflow deposition system. The identified components include: (1) Feed reservoir; (2) Peristaltic pump; (3) Pressure transducer; (4) Aluminum crossflow filtration sub-module; (5) Retentate line needle valve; (6) Retentate line rotameter; (7) Digital balance; (8) HF membrane. Locations for the feed (F), retentate (R), and permeate (P) streams around the filtration sub-module are identified. b) Picture of the experimental set-up with three crossflow deposition experiments running in parallel. Numbered components correspond to the same equipment identified in Panel a. c) Sample preparation for CNT-coated HF analysis. The CNT-coated HF is removed from sub-module and sectioned into six segments. Each segment is cut in half and folded open to the interior surface for analysis via four-point probe conductivity measurement (shown) and scanning electron microscopy.

CNT deposition experiments consisted of six sequential steps:

- i) Membranes were wetted via dead-end filtration of DI water for a maximum of 1 h or until a constant pressure ( $\pm 5\%$ ) was maintained for 10 minutes. The flow rate was set between 7.5–12 mL/min per HF to achieve an initial pressure of at least 0.2 bar.
- ii) Pure water permeability was measured in dead-end mode with DI water as the feed source. Using the peristaltic pump, the feed flow rate was set to 4–6 different values between 0.5–6 mL/min (per HF). Hydraulic permeability ( $L_p$ ) was calculated according to Eq. 1:

$$L_p = \frac{J}{\Delta P} \quad (1)$$

where  $J$  is the permeate flux ( $L/m^2h$ , LMH) and  $\Delta P$  is the average transmembrane pressure (TMP, bar) recorded by the pressure transducer. Permeate flux was calculated as flow rate divided by the effective HF membrane area ( $5.03 \times 10^{-4} m^2$ ). A set of typical TMP and flux curves are included in Fig. 2.S1. On average, the unmodified PES HF membranes had a pure water permeability of 5,540 LMH/bar, with values ranging from ~1,200–11,000 LMH/bar (Fig. 2.S2). A previous study also reported a considerable variation in the permeability of HF PVDF membranes [43].

- iii) The system was then operated in crossflow filtration mode. Using DI water as the feed, the pump flow rate and retentate needle valves were simultaneously and manually adjusted to obtain the desired feed pressure and crossflow velocity, verified via a pressure transducer and retentate line rotameter. The feed source was then replaced with the SW/DWCNT-SDS-PVA suspension for deposition. Crossflow velocity was manually verified every 2 minutes for each HF via the rotameter. Crossflow deposition proceeded until a permeate volume of 60 mL was collected from each HF membrane allowing total deposition time to vary depending on the permeation rate at each combination of feed pressure and crossflow velocity.

- iv) The modules were drained completely and removed from the set-up. The entire module was cured in an oven at 100°C for 1 h. After curing, the module was cooled to room temperature and filled with DI water to condition the CNT-coated HF membranes overnight (12–24 h).
- v) CNT-coated HF membranes were re-wetted via dead-end filtration of a 50 vol% isopropanol/DI water solution for 30 minutes, with flow rates and pressures maintained under the same conditions as the initial membrane wetting step (Step (i)). CNT-coated HF membranes were then rinsed with DI water under dead-end filtration for 30 minutes. After which, the modules were drained and rinsed three times with DI water to remove remaining isopropanol.
- vi) Pure water permeability for the CNT-coated HF membranes was measured following the same protocol as the initial permeability measurement (Step (ii)).

To optimize the CNT-coated HF membrane performance, a two-level, two-factor (feed pressure and crossflow velocity), full factorial (i.e.  $2^2 = 4$  conditions) design-of-experiments (DOE) study was established. The high and low conditions for feed pressure were 0.2 and 0.1 bar; the high and low conditions for crossflow velocity were 1.06 and 0.32 cm/s (corresponding to volumetric flow rates of 0.5 and 0.15 mL/min). These values were selected to cover a wide range of permeation driving forces (pressures) and shear rates (crossflow velocities) to study the effects of these parameters on CNT deposition patterns. CNT-coated HF membrane performance at each of these conditions was evaluated in terms of pure water permeability and surface conductivity. For each condition, two runs were completed with the parallelized set-up resulting in six different coated HF membranes (3 HF membranes per run). Two control experiments were also conducted using this protocol. The first one was based on the same preparation and curing process, but the crossflow deposition step was excluded (i.e. “Heat” control). The second one was based on the

same preparation, crossflow deposition (crossflow velocity of 0.21 cm/s and feed pressure of 0.06 bar) and curing process but the feed suspension did not contain SW/DWCNTs (i.e. “PVA & Heat” control). In these experiments, each condition was repeated for six HF membranes, with the exception of the “Heat” control which was repeated for five membranes. Although this work focused on an inside-out configuration, this approach of optimizing flow patterns could also be adopted for an outside-in hollow fiber support by changing the location of the feed, permeate and retentate ports.

#### 2.4.4 *Surface Conductivity Analysis*

The CNT-coated HF membranes were removed from the module as illustrated in Fig. 2.1c then stored in a glass Pyrex tube and dried at room temperature for at least 24 h. The dried membranes were cut into six segments, four of which were 3 cm in length and two were 2 cm. Each segment was cut in half along the cross-section, folded open, and mounted onto a glass microscope slide using double-sided Scotch tape. Surface conductivity was measured using a four-point probe conductivity meter (Ossila T2001A3). Each segment was measured three times resulting in 18 conductivity measurements (6 segments  $\times$  3 measurements per segment) for each HF membrane. Geometric correction factors were verified by manual calculation using the thin, rectangular slice approximation [44].

#### 2.4.5 *Scanning Electron Microscopy (SEM)*

A JEOL JSM-7000F scanning electron microscope was used to capture micrograph images of the CNT-coated HF and unmodified PES HF membranes. Membrane samples were first dried following the same protocol used for the conductivity measurements. Cross-sectional images were obtained by immersing the HF membrane in liquid nitrogen and manually fracturing it along the cross-section to preserve the pore structure. All the membrane samples were sputter coated with 5

nm of platinum prior to imaging. For image capture, a working distance of 10 mm, accelerating voltage of 5.0 kV and probe current between 2–5 pA were maintained.

## 2.5 Results & Discussion

SW/DWCNTs were deposited on the lumen side of inside-out hollow fiber (HF) membranes (i.e. the inside walls of the HF) during crossflow filtration to form electrically conductive membranes (ECMs). The effects of applied pressure, crossflow velocity, and feed concentration on membrane permeability and surface conductivity were investigated.

### 2.5.1 Optimization of the Crossflow Conditions for Depositing CNTs onto HF Membranes

The effects of feed pressure and crossflow velocity on HF membrane permeability and conductivity are displayed in the top and bottom panels respectively of Fig. 2.2. The four figures within each panel are displayed in a manner consistent with the  $2^2$  DOE study conditions. For example, the figure in the top right corner of each panel corresponds to the high crossflow velocity (1.06 cm/s) and high feed pressure (0.2 bar) condition, while the figure in the bottom left corner of each panel corresponds to the low crossflow velocity (0.32 cm/s) and low feed pressure (0.1 bar) condition. A total of 6 CNT-coated HF membranes (identified as “a” through “f” on the x-axes) were prepared at each DOE study condition; thus, the results for 24 membranes from the  $2^2$  DOE study are displayed in each panel.

For the permeability results in panel a of Fig. 2.2, the error bar for each membrane corresponds to the 95% confidence interval from the linear regression analysis of permeate flux (LMH) versus applied pressure (bar). It is evident that at the high crossflow velocity condition, there was fairly good agreement in the permeability values for all 6 membranes. For example, at the high crossflow velocity and low feed pressure condition, hydraulic permeabilities for the CNT-coated HF membranes ranged from 2700–6900 LMH/bar. The permeability range narrowed further to 3000–

3600 LMH/bar at the high crossflow velocity and high feed pressure condition, excluding membrane “a” with 500 LMH/bar. This is a significant outcome given the variation we observed in the permeability of the unmodified PES HF membrane (see Fig. 2.S2) upon which the CNT coating was deposited and the known challenges in achieving homogeneous dispersions of CNTs [45]. However, at the low crossflow velocity condition there was much greater variation in the permeability values across the 6 membranes. Our hypotheses for why this occurred are discussed below. Despite this variability, statistically significant trends were evident for the effect of crossflow velocity on CNT-coated HF membrane permeability. While maintaining constant pressure, permeabilities were significantly higher (two-sample t-test p-value < 0.05; see Fig. 2.S3) at the high crossflow velocity condition at both 0.1 and 0.2 bar. However, there was no significant difference in permeability between the high- and low-pressure conditions at constant crossflow velocities (two-sample t-test p-value > 0.05; see Fig. 2.S3).

As shown in panel c of Fig. 2.2, each CNT-coated HF membrane was sectioned into six segments to determine the surface conductivity profile along the membrane. The results from that analysis are presented in panel b of Fig. 2.2 with the error bar for each segment corresponding to the standard deviation from triplicate measurements using the four-point probe conductivity meter. In a similar way to the membrane permeability results discussed above, the high crossflow velocity condition of the DOE study produced membranes with low variation in the conductivity values, both within the length of an individual HF membrane and between different HF membranes. For example, at the high crossflow velocity and high feed pressure condition, the conductivity measurements ranged from 220 S/m–2500 S/m (one order of magnitude difference). This contrasts with the low crossflow velocity condition, in which a wide variation in conductivity values was

observed. For example, at the low crossflow velocity and low feed pressure condition, conductivities ranged from 0.01 to 140 S/m (five orders of magnitude difference).

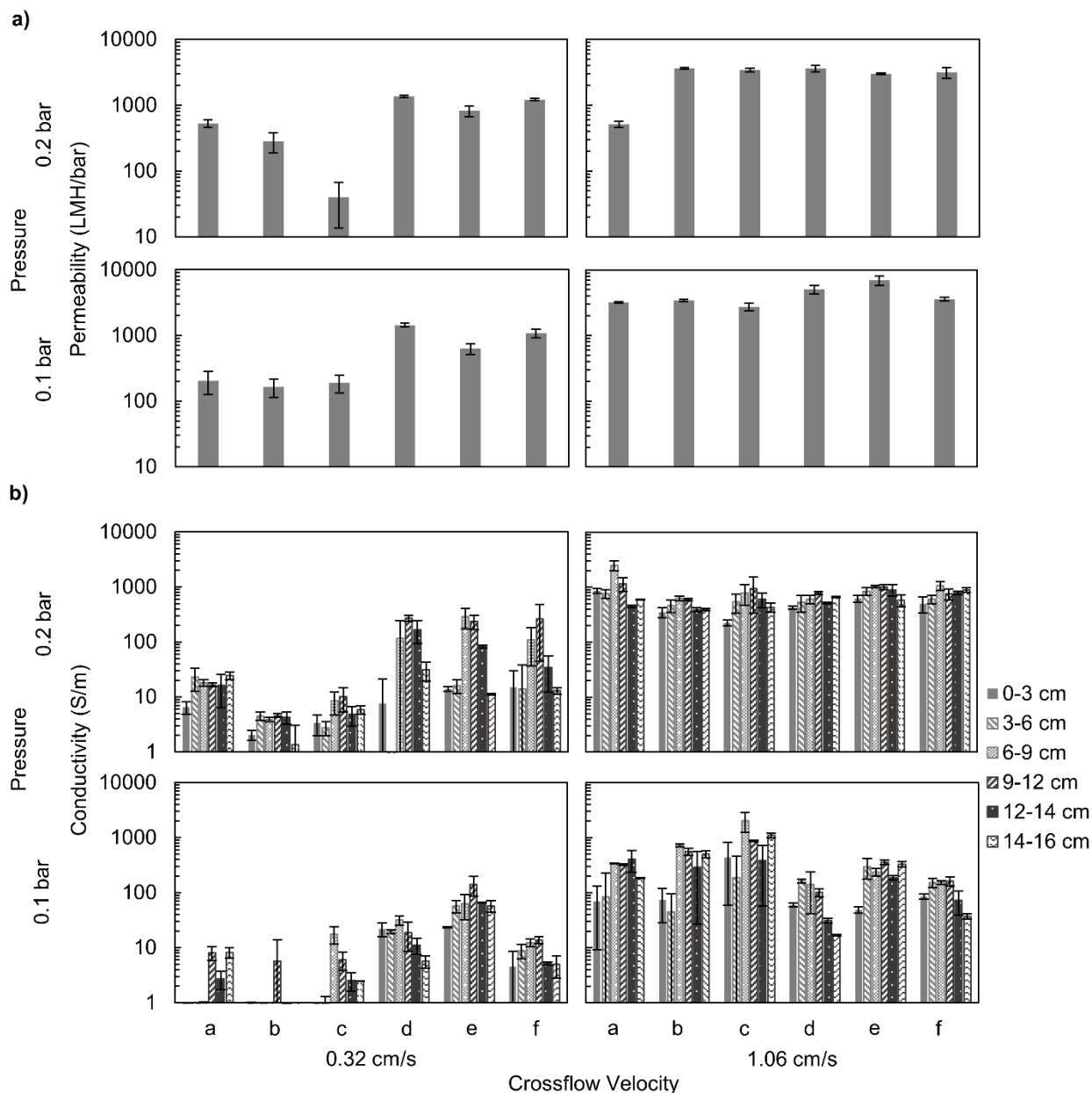


**Figure 2.2.** Hydraulic permeability (panel a) and surface conductivity (panel b) results for the CNT-coated HF membranes; the x-axis categories for both panels (a, b, c, d, e, and f) correspond to the six membranes that were made at each of the four conditions of the  $2^2$  DOE study. The error bars in panel a correspond to the 95% confidence intervals from the linear regression of permeate flux (LMH) and applied pressure (bar) for each individual membrane. The error bars in panel b correspond to the standard deviation of the triplicate measurements made on the six segments excised from each individual membrane.

Membranes coated at the low crossflow velocity condition were measured to have a large variation in the measured conductivity values both between different HF membranes coated at the same conditions as well as along the length an individual HF membrane. A few membranes had considerable variation in the conductivity values for the short segments that were cut from the same HF membrane. For example, membrane “d” at the low crossflow velocity and high feed pressure condition was uncoated between segments i and ii where CNTs were deposited well near the inlet (beginning of segment i) then did not deposit again until the end of segment ii (see Fig. 2.S4). Similar patches of non-coated areas also formed in random positions along membrane “f” at the same coating condition and for membranes “a,” “b,” and “c” at the high crossflow velocity, low pressure condition. Due to the random nature of these patches, it is our hypothesis that they are due to some particular physico-chemical property (e.g. hydrophobicity) of the PES MF membrane itself upon which the CNTs are deposited; this phenomenon will be the subject of a forthcoming study.

Conductivity showed a statistically significant dependence on both crossflow velocity and feed pressure. Measured conductivities were significantly higher when increasing crossflow velocity under constant pressure at both 0.1 and 0.2 bar, and when increasing pressure under constant crossflow velocity at both 0.32 and 1.06 cm/s ( $p < 0.05$ , see Fig. 2.S3).

Interestingly, it was found that the highest membrane permeability and conductivity were obtained at the same condition of high pressure and high crossflow velocity. Both the measured increase in conductivity (panel b of Fig. 2.2) and the visually darker coatings (see Fig. 2.S4) suggest that SW/DWCNTs had deposited to a greater extent and with greater uniformity at the high-pressure conditions. Increasing crossflow velocity leads to two contrasting effects: 1) increased shear, which can encourage particle detachment; 2) increased particle loading, which

increases deposition probability [46]. Previous works demonstrate evidence for both of these effects, where extent of deposition can be increased with increasing crossflow velocity if particle loading is dominant [41], and decreased if shear is dominant [40]. Increased pressure or permeation flow has consistently been shown numerically [38,39] and experimentally [40,41] to increase both the rate and extent of particle deposition. Therefore, previous evidence suggests that both increased crossflow velocity and increased pressure can lead to greater particle deposition which is consistent with our observations. We attempted to quantify the residual amount of SW/DWCNTs in solution using a variety of analytical techniques (e.g. total organic carbon, thermogravimetric analysis, UV-Vis spectroscopy), however it proved to be extremely difficult due to the low concentration of SW/DWCNTs used in this work as well as confounding effects due to the presence of PVA and small amounts of impurities from the SW/DWCNT source (e.g. ash) [47].

The observed increase in both conductivity and permeability (see Fig. 2.2) within the DOE parameter space is an interesting finding that cannot be explained by the extent of SW/DWCNT deposition alone given the following two arguments: 1) for a constant mass of SW/DWCNTs, a denser coating would be required to achieve a higher conductivity which would subsequently result in a lower permeability; 2) for a non-constant mass of SW/DWCNTs, a higher conductivity may suggest more SW/DWCNTs were deposited, which would also lead to lower permeability by pore blocking. We hypothesize that coating uniformity played a greater role than coating density in optimizing these performance metrics. The visual observations suggest SW/DWCNT coatings were more uniform at the high crossflow, high pressure condition (see Fig. 2.S4), which corresponded to the highest conductivity and permeability in the DOE (see Fig. 2.2). This is consistent with related particle deposition research where increased crossflow velocity and permeation rate lead to greater uniformity of deposited foulants along a membrane [41]. As

described below, particle deposition theory can be used to explain why the extent of CNT deposition increased with both feed pressure and crossflow velocity. In crossflow filtration, the balance between permeation drag and inertial lift forces determines if particle deposition will occur [39]. Permeate flow induces a drag force that drives particles towards the membrane wall [38][39], which is evident in this work as increasing the driving force for permeation resulted in a greater extent of CNT deposition. However, the crossflow velocity condition induces an inertial lift effect that has been shown to have two components: 1) “wall-effect” lift that opposes deposition; 2) “shear-gradient” lift that encourages deposition [48-50]. Our results indicate a greater extent of SW/DWCNT deposition under high crossflow velocity, which suggests that within the crossflow velocity range of the DOE, the “shear-gradient” inertial lift component was dominant.

To evaluate the potential effects of the other membrane processing steps, two control experiments were conducted. The first experiment studied the effect of the curing process alone without a prior crossflow deposition procedure (i.e. “Heat” control). The second experiment studied the effect of the filtration (crossflow velocity of 0.21 cm/s and feed pressure of 0.06 bar) and curing process in the absence of SW/DWCNTs in the feed solution (i.e. “PVA & Heat” control). Permeability measurements obtained at both control conditions as well as the four points from the DOE are shown as a boxplot in Fig. 2.3, along with the equivalent statistics from the permeability results in Fig. 2.2. The average permeability for the unmodified PES HF membranes was 5540 LMH/bar and is included in the plot as a reference line. Compared to this reference, heat treatment of the PES HF membranes resulted in a final permeability ~21% of its initial value, while with prior coating of PVA solution this was increased to ~51% of its initial value. Two statistically significant groups formed when comparing membrane permeabilities from the control tests with those from the CNT-coated HF membranes in the DOE. Permeabilities for the CNT-coated HF

membranes fabricated at the low crossflow velocity condition (shaded, hashed boxes) were statistically similar to the heat-treated membranes, whereas CNT-coated HF membranes at the high crossflow velocity condition (shaded, solid boxes) were statistically similar to the membranes first coated with PVA solution ( $p < 0.05$ ; see Fig. 2.S3).

We hypothesize that poorly coated membranes suffered extreme permeability loss during the post-deposition heat treatment step (100°C for 1 hour). Moreover, we propose that the uniform deposition of CNTs on the underlying PES MF membrane protects it during the heat treatment step. As such, greater amounts and more uniform coatings of CNTs prevent permeability loss, while providing greater surface conductivity. It has been shown that exposing PES HF UF membranes to temperatures in the range of 120 to 180°C for just short periods of time (i.e. 5 to 15 minutes) results in an approximate 40% drop in membrane permeability [51]. By increasing the exposure time to 1 h, our PES HF membranes exhibited an even greater permeability loss in the heat-treated control, as well as in the CNT-coated HF membranes at the low crossflow velocity condition. At these conditions, the HF membrane surface was poorly coated with CNTs, as indicated by the light grey surface in the membrane photos (see Fig. 2.S4), which left the PES surface exposed in the heat treatment step. In contrast, at high crossflow velocity, the CNT-coated HF membranes were more uniformly coated which likely protected the internal pore structure from drying out, resulting in a lower permeability loss. Protection against thermally induced permeability loss was likewise demonstrated in the “PVA & Heat” control membranes, in which PVA coatings protected the PES HF membranes from drying out. PVA coated membranes can improve surface hydrophilicity resulting in increased permeability [52] and have therefore been exploited to preserve permeability when heat treating membrane surfaces for chemical cross-linking [53,54]. The impact of heat treatment rather than pore blockage was the most statistically

significant effect for determining final membrane permeability which explains the increase in both conductivity and permeability observed in the  $2^2$  DOE. This further supports our claim that coating uniformity is critical to conductive HF membrane optimization.

A multiple linear regression analysis was conducted using Minitab software to quantify the impact of the crossflow deposition flow parameters studied in the  $2^2$  full factorial DOE on the CNT-coated HF membrane performance. Two quantitative responses were assessed: CNT-coated HF membrane permeability with 6 measurements at each DOE point, and conductivity with 36 measurements (6 measurements  $\times$  6 HF membranes). The resulting regression models are shown as surface plots in Fig. 2.4 and the residual plots for these models are provided in Fig. 2.S6. Membrane permeability exhibited a strong positive relationship with crossflow velocity but showed no statistically significant trend with pressure ( $p > 0.05$ , see Table S1), while conductivity exhibited a strong positive relationship with both crossflow velocity and pressure ( $p < 0.05$ , see Table S1). The interaction between crossflow velocity and pressure was only significant for the conductivity model ( $p < 0.05$ , see Table S1) which is consistent with Fig. 2.2 as the combination of high pressure and crossflow velocity resulted in the highest conductivity. Fig. 2.4 clearly shows that crossflow deposition flow parameters have a significant impact on final membrane performance. Note that the linear regression models are defined only within the bounds of the DOE. Intercept terms have no physical meaning and are provided only to improve model fit. Further optimization of these flow parameters is required to identify the ideal combination resulting in both high conductivity and high permeability.

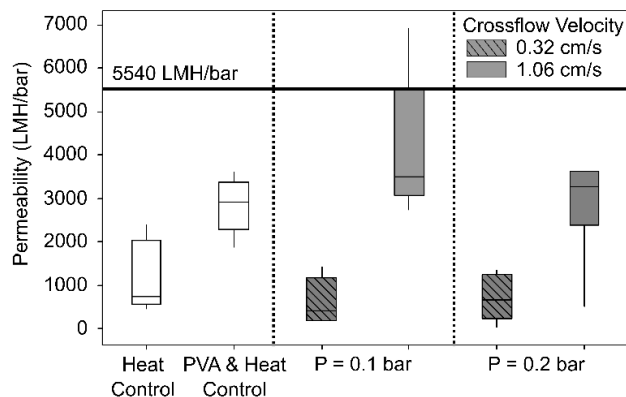


**Figure 2.3.** Boxplot comparison of the hydraulic permeability results for the CNT-coated HF membranes prepared at the four conditions of the  $2^2$  DOE study and two control conditions involving no CNTs. The results from the DOE study are organized according to the feed pressure and crossflow velocity values. For each boxplot, the mid-line corresponds to the median, the upper and lower box bounds correspond to the interquartile range, and the whiskers correspond to the maximum and minimum values.

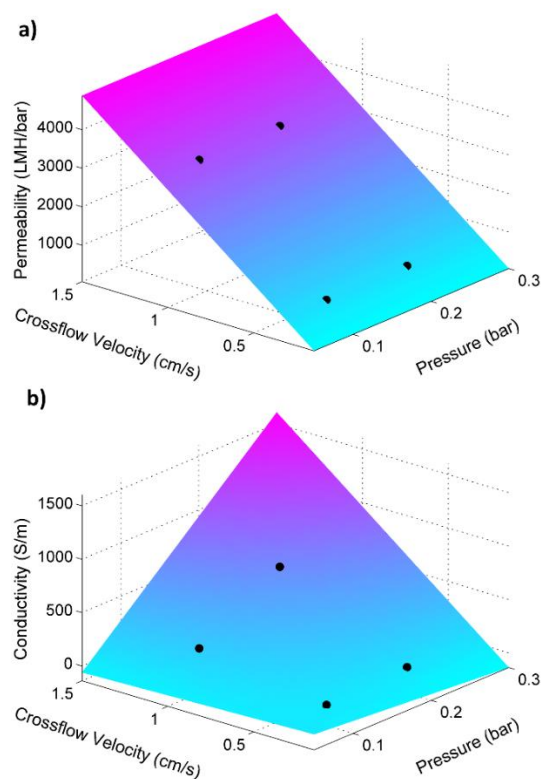


**Figure 2.4.** Full-factorial regression models for the  $2^2$  DOE study evaluating CNT-coated HF membrane **a)** permeability and **b)** conductivity in terms of crossflow velocity (cm/s) and pressure (bar). The multiple linear regression model for panels are as follows: a)  $Permeability = -480 + 3575 \times v$  b)  $Conductivity = 84.7 - 1384 \times P - 317.9 \times v + 5361 \times (P \times v)$ . Note that models are defined only within the range of conditions studied in the DOE: crossflow velocity of 0.32–1.06 cm/s and feed pressure of 0.1–0.2 bar. The filled circular symbols within each panel indicate the four experimental results from the  $2^2$  DOE study.

To relate the membrane performance results reported above to the physical properties of the composite HF membrane, scanning electron microscopy (SEM) images were obtained in both top-down and cross-sectional orientations. Representative images are shown in Fig. 2.5 for the unmodified PES HF membrane and two CNT-coated HF membranes. The porous interior surface of the unmodified PES HF membrane is visible in Fig. 2.5 with a pore size on the order as expected from the manufacturer (0.2  $\mu\text{m}$ ). The asymmetry of the PES membrane is apparent in Fig. 2.5 in which the low magnification cross-sectional images illustrate the skin layer present on the interior membrane surface. Note that while these SEM images only show a few hundred  $\mu\text{m}^2$  surface area chosen randomly along the length of the HF, they are representative of the entire HF. A clear morphological change between the unmodified PES HF membrane (Fig. 2.5a) and the CNT-coated HF membrane surface (Fig. 2.5c) can be identified in the top-down SEM images, indicating that the PES surface was well coated with SW/DWCNTs. Individual SW/DWCNTs and fiber bundles are identifiable as the fibrous structures on the membrane surface.

The approximate thickness of the CNT layer was measured at multiple points along the length of the HF membrane to be in the range of 0.4 to 1.4  $\mu\text{m}$  via analyzing the cross-section SEM images using ImageJ software. This coating thickness is 1–2 orders of magnitude thinner than composite CNT HF membranes from Wei et al. [32]. This substantial difference in coating thickness had significant impacts on the membrane permeability: 7.2 LMH/bar in [32] compared to 2900 LMH/bar for the CNT-coated HF membrane in Fig. 2.5 c, d. The thinner, more permeable coating also achieved higher conductivity: 280 S/m in [32] compared to an average of 670 S/m for the CNT-coated HF membrane in Fig. 2.5 c, d. Using the crossflow deposition method, we achieved a thin film coating of SW/DWCNTs with a coating thickness comparable to that reported in previous works on the formation of CNT-coated flat sheet membranes [5,8,12].

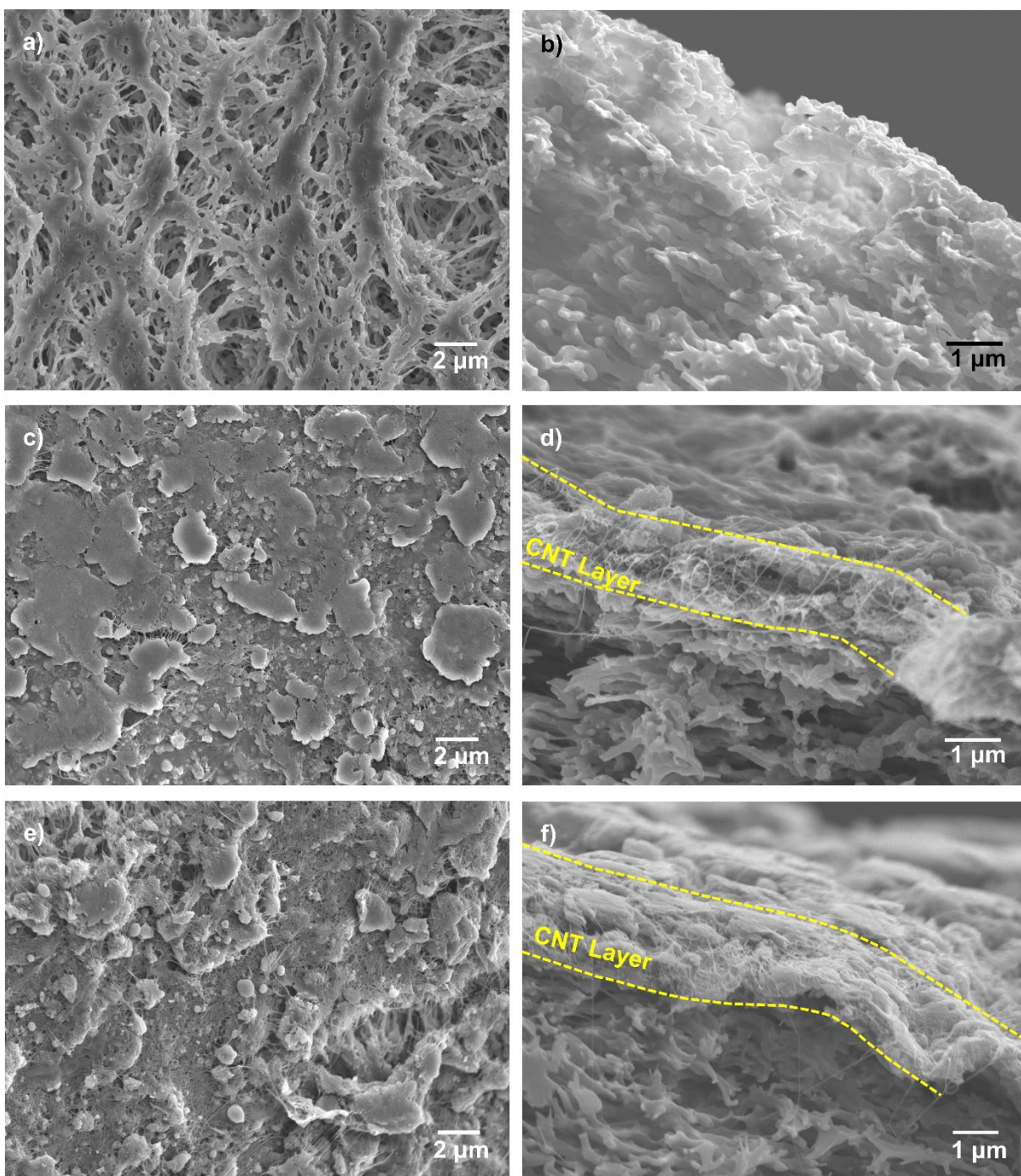


**Figure 2.5.** Representative SEM images of the interior surface of the HF membranes in both top-down orientations (left panels a, c, and e) and cross-sectional orientations (right panels b, d, and f). The top row (panels a and b) corresponds to the unmodified PES HF membrane. The middle row (panels c and d) corresponds to a CNT-coated HF membrane produced at a deposition feed pressure of 0.2 bar, crossflow velocity of 1.06 cm/s, and feed concentration of 7.5 mg/L CNTs. The bottom row (panels e and f) corresponds to a CNT-coated HF membrane produced at a deposition feed pressure of 0.1 bar, crossflow velocity of 0.32 cm/s, and feed concentration of 18.8 mg/L CNTs.

### 2.5.2 Feed Concentration Effects on CNT-coated HF Membranes

We chose to also study the effects of concentration of CNTs in the feed solution on the membrane performance at a fixed set of filtration conditions. Crossflow velocity and feed pressure were set to the lower limits from the DOE (0.32 cm/s and 0.1 bar, respectively) as this condition exhibited the lowest conductivity and permeability, therefore any improvement in coating due to increased SW/DWCNT concentration would be immediately apparent. The boxplot in Fig. 2.6 illustrates the substantial increase in both hydraulic permeability and surface conductivity attained at the higher concentration level compared to the DOE condition.

On average, the hydraulic permeability for membranes prepared at the higher feed concentration was 3 times higher than those prepared at the lower feed concentration. This counter-intuitive finding supports our hypothesis that well-coated CNTs protect the underlying PES membranes from thermally induced permeability loss. Much like the results in the DOE, an increase in permeability occurred simultaneously with an increase in conductivity and extent of deposition. Greater SW/DWCNT deposition on the surface likely protected the membrane pore structure from heat treatment, leading to better permeability recovery as discussed in the previous section.

The 100-fold increase in conductivity with the higher feed concentration is intuitive as there was more conductive material available in the feed for deposition and in general, particle deposition rates tend to increase with higher particle feed concentration [55]. Initial pressure was controlled to 0.1 bar but was increased throughout the crossflow deposition process to maintain a constant permeate flux as shown in the deposition pressure profiles at both concentration levels (see Fig. 2.S7). This increase in pressure was more substantial at the higher SW/DWCNT feed concentration with a maximum of 0.58 bar, compared to 0.22 bar for the lower concentration. The

higher maximum deposition pressure suggests greater resistance to flow at the higher feed concentration, likely due to increased SW/DWCNT deposition. Depositing a thin film layer with a higher concentration of SW/DWCNTs creates a more interconnected network which increases the probability of meeting and exceeding the percolation threshold (i.e. the density of SW/DWCNTs sufficient to conduct electricity across the membrane [56]). Although the mass of SW/DWCNTs deposited was not explicitly investigated, the 100-fold increase in conductivity at the high feed concentration suggests a much greater density of conductive material on the surface, in excess of the percolation threshold.

CNT concentration is a significant parameter for controlling ECM conductivity in the pressure or vacuum deposition fabrication technique. In previous development of flat sheet ECMs, increasing CNT concentration in the feed suspension is one method for improving surface conductivity [35]. This method relies on a dead-end deposition approach, thus an increase of CNTs in the feed directly leads to greater deposition. With the crossflow deposition method, there is no guarantee that all SW/DWCNTs present in the feed will deposit, therefore concentration plays an even more significant role in determining the probability of deposition.

SW/DWCNT thin film thickness and morphology for the HF membrane coated at the high concentration condition was comparable to the CNT-coated HF membrane from the DOE as confirmed by Scanning Electron Microscopy (SEM). SEM images of the CNT-coated HF membrane coated at high concentration (18.8 mg/L SW/DWCNTs at 0.32 cm/s crossflow velocity and 0.1 bar feed pressure) are shown in both top-down (Fig. 2.5e) and cross-sectional (Fig. 2.5f) configurations. The surface morphology of this CNT-coated HF membrane (Fig. 2.5e) is similar to the membrane from the DOE (Fig. 2.5c) and distinctly different from the unmodified PES HF surface (Fig. 2.5a). Coating layer thickness was estimated from the cross-sectional image (Fig.

2.5f) to be 0.6–1.3  $\mu\text{m}$ , which is in the same range as the CNT-coated HF membrane in Fig. 2.5d. This once again emphasizes the importance of understanding the influence of deposition flow parameters on HF performance as this thin coating achieved both high permeability (1800 LMH/bar) and conductivity (2000 S/m).

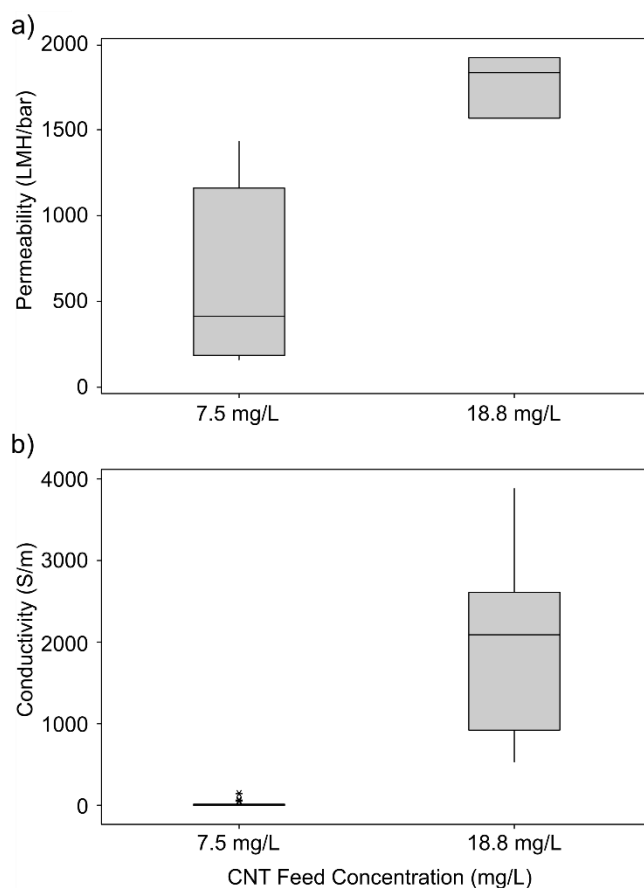


**Figure 2.6.** Boxplot comparison of effects of CNT feed concentration on hydraulic permeability (panel a) and surface conductivity (panel b) for CNT-coated HF membranes. For each boxplot, the mid-line corresponds to the median, the upper and lower box bounds correspond to the interquartile range, and the whiskers correspond to the maximum and minimum values. Statistical analysis in panel a) was based on permeability measurements for six HF membranes and three HF membranes formed with CNT feed concentrations of 7.5 mg/L and 18.8 mg/L, respectively. Statistical analysis in panel b) was based on conductivity measurements for six segments excised from each individual membrane (i.e. 36 measurements at 7.5 mg/L, 18 measurements at 18.8 mg/L).

Under higher magnification (see Fig. 2.S8), the distinction in surface morphology between the two CNT coated membranes in Fig. 2.5 c and e in terms of density of CNTs present in the coating layer becomes more apparent. These images show CNTs deposited in a random orientation to form a porous network under both coating conditions; however, the CNT coated HF in Fig. 2.S8b showed a greater proportion of CNTs in the surface layer. This corresponded to a higher surface conductivity compared to the membrane in Fig. 2.S8a (2000 S/m compared to 670 S/m) but lower permeability (1800 LMH/bar compared to 2900 LMH/bar). We hypothesize this difference in permeability is due to two major effects 1) increased pore blockage due to greater CNT deposition in Fig. 2.S8b and 2) greater presence of hydrophilic PVA in Fig. 2.S8a indicated by the surface deposited globular structures.

### *2.5.3 Examination of the Conductivity/ Permeability Trade-off for CNT-coated HF membranes via a Robeson-Like Plot*

To determine the limits of the CNT-coated HF membrane performance in terms of both surface conductivity and membrane permeability, we adopted the graphical approach that was developed by Robeson in his landmark paper on the gas separation capabilities of polymeric membranes [57] and then subsequently extended to other membrane science fields such as protein purification [58] and desalination [59,60]. To the best of our knowledge, this is the first time that this approach has been applied to the field of ECMs. The scatter plot shown in Fig. 2.7 displays the results for 29 CNT-coated HF membranes that were fabricated according to the different feed pressure, crossflow velocity, and feed concentration conditions as described in Sections 3.1 and 3.2. We excluded the results for the 10 membranes that were found to have the randomly located bare patches of membrane as noted in Section 3.1.

Overall, there is a general inverse trend between ECM surface conductivity and hydraulic permeability. This is most apparent when comparing the extremes of these two metrics. The maximum CNT-coated HF membrane permeability was 6450 LMH/bar, with a surface conductivity of 240 S/m. Conversely, 10-fold higher conductivities were achieved, with a maximum of 2200 S/m at the expense of a 4-fold lower permeability value of 1570 LMH/bar. The cluster of points near the origin with both low permeability and conductivity are an exception to this overall trend and represent the low crossflow velocity conditions from the DOE that exhibited surface coatings with low CNT density and uniformity (see Fig. 2.S4). In Section 3.1, we attributed this phenomenon to thermally induced permeability loss due to heat treatment of a poorly coated membrane surface. The solid black line in Fig. 2.7 represents the ‘upper bound’ of the CNT-coated HF membranes fabricated in this study. The shape of this curve was determined by fitting a model of the form  $y = kx^n$ , where  $y$  represents the conductivity and  $x$  represents the permeability to a sub-set of the data and then adjusting the values of the two fitting parameters such that the residual values between the model predictions and experimental data were all negative. Data points used to fit the model include the black open squares, black closed squares and green closed squares that most closely follow the upper limit line (8 points in total, Table S2).

In comparison to other CNT-based HF membranes made using alternative techniques, it would appear that there is a clear advantage to the crossflow deposition approach developed in this study. For example, the process of vacuum depositing MWCNTs onto HF membranes resulted in a reasonable conductivity (280 S/m) but very low permeability (7 LMH/bar) [25]. Also, the process of direct electrospinning of MWCNTs into a HF structure resulted in a very high permeability (12,000 LMH/bar) but very low conductivity (1.2 S/m) [1].

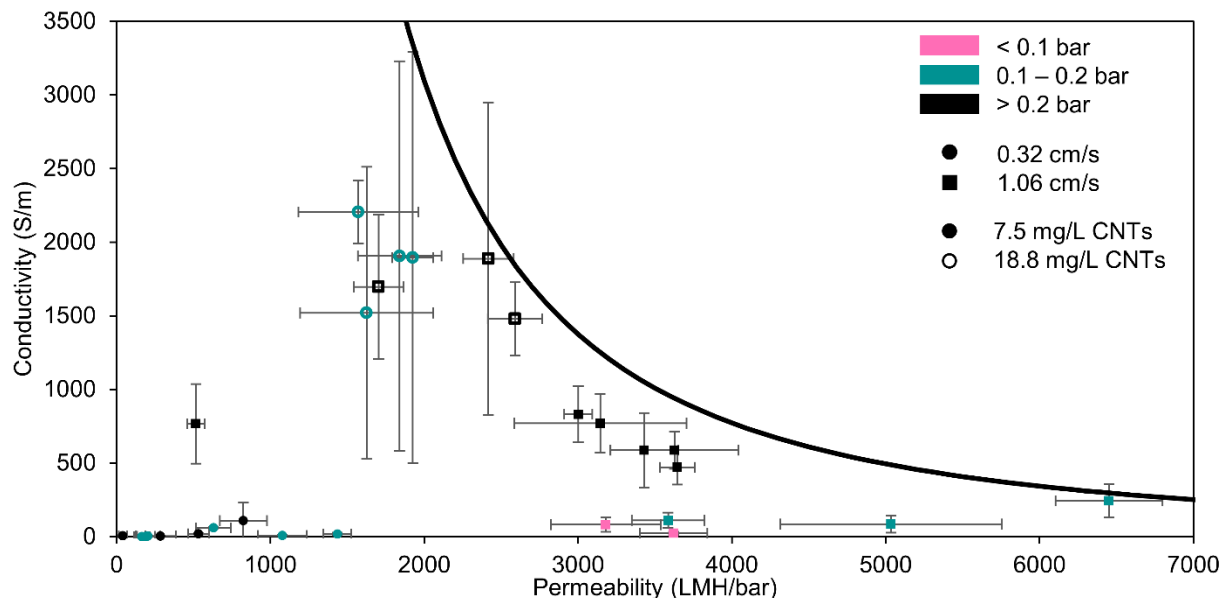


**Figure 2.7.** Robeson-like plot comparing the conductivity and permeability values for the 29 CNT-coated HF membranes that were fabricated in this study. Horizontal error bars correspond to the 95% confidence intervals from the linear regression analysis of filtrate flux (LMH) versus TMP (bar). Vertical error bars correspond to the standard deviation for the six segments from a single CNT-coated HF. The three symbol colours correspond to the range of feed pressure values. The round symbols (●, ○) and square symbols (■) correspond to crossflow velocities of 0.32 and 1.06 cm/s, respectively. The filled symbols (●, ■) and empty symbols (○) correspond to CNT concentrations in the feed suspension of 7.5 and 18.8 mg/L respectively. The upper performance limit (black line) was established by fitting an exponential curve to select data and then adjusting the model parameters such that the residual values were negative for all of the fitted data points:  $C = 1.27 \times 10^{10} \cdot L_p^{-2.00}$ .

CNT-coated HF membranes prepared with the higher SW/DWCNT feed concentration tended towards higher conductivities and lower permeabilities. In Section 3.2, we attributed this increase in conductivity with a greater availability of conductive material as well as an increase in deposition driving force (pressure) over time. A decrease in permeability, as seen in the Robeson plot (Fig. 2.7), was not apparent in Fig. 2.6. We hypothesize that a critical concentration of SW/DWCNTs protects the membranes from drying out and collapsing the pores during heat treatment, and thereby preventing a decrease in permeability. As SW/DWCNT concentration increases, the SW/DWCNTs physically block the membrane pores and the benefits to membrane permeability of protection from heat treatment are outweighed by pore blockage. Pore blockage

may have become the more dominant effect when taking the full parameter space into consideration. As evidenced from the SEM images (Fig. 2.5) and the measured reduction in CNT-coated HF membrane permeability, we hypothesize that pore blockage dominates the impacts to membrane permeability for the membranes coated at high SW/DWCNT concentrations as compared with that at low concentrations. Additionally, increased SW/DWCNT concentration led to greater error in conductivity measurements along the length of the HF membranes. This lack of uniformity could be due to the greater variability in permeation driving force as pressure increased substantially throughout the deposition process (Fig. 2.S7).

The two flow parameters evaluated in this study (crossflow velocity and feed pressure) both had a strong impact on the balance between CNT-coated HF membrane permeability and conductivity. Crossflow velocity had an especially significant impact on permeability. CNT-coated HF membranes coated at higher crossflow velocities (square points) tended towards higher permeabilities, which is consistent with the trend observed in the DOE where crossflow velocity was the only significant parameter impacting permeability. This parameter is clearly critical in fine tuning membrane permeability. When feed pressure is maintained higher than 0.1 bar, we obtained conductive and permeable HF membranes. Below this pressure, we suspect there is insufficient SW/DWCNT deposition to cross the percolation threshold required for conductivity. Conductivity shows a strong dependence on both crossflow velocity and feed pressure. The most conductive coatings from the DOE required both high pressure and crossflow velocity (black squares). Of note, membranes coated with high pressures, but low velocities (black circles) demonstrate very low conductivities, primarily due to a lack of coating uniformity that leads to CNT-coated HF membranes with uncoated or poorly coated regions.

## 2.6 Conclusions

A crossflow deposition process for fabricating electrically conductive HF membranes was developed in this work to achieve a thin, conductive SW/DWCNT layer on the lumen side of microfiltration PES membranes. Using a parallelized crossflow deposition system, a robust statistical study was conducted with 50 HF membranes in total to evaluate the effects of crossflow deposition parameters, curing, and SW/DWCNT concentration on composite membrane conductivity and permeability. In a  $2^2$  full factorial design-of-experiments study, both feed pressure and crossflow velocity were found to significantly impact CNT-coated HF membrane conductivity, while permeability was more strongly affected by crossflow velocity alone. The impact of these crossflow deposition parameters is consistent with other particle deposition literature and attributed to the balance of permeation drag and inertial lift effects. For poorly coated membranes, there was evidence of a “drying-out” effect after curing as these membranes exhibited much lower permeabilities than more well-coated membranes. We believe the internal pore structure was more protected for well-coated membranes, thus preventing pore collapse and preserving membrane permeability. Increasing SW/DWCNT feed concentration significantly improved both permeability and conductivity; however, the variability in conductivity along the length of the HF also increased. This reduction in uniformity was attributed to greater variation in the permeation driving force due to the more substantial increase in feed pressure over time.

To illustrate the performance trade-off between conductivity and permeability, we created the first-ever Robeson-like plot for ECMs. Our results show a clear inverse relationship between these two metrics. Although further optimization of the crossflow deposition conditions and process materials (i.e. type and purity of CNTs, use of chemical cross-linkers) is required, this system presents an opportunity to balance the trade-off between composite membrane permeability and

conductivity that is not achievable in dead-end vacuum deposition processes where flow parameters are not controlled. We anticipate these conductive HF membranes will be useful in electrochemical membrane applications including enhanced charged particle removal and antifouling. Future work in this area will include systematic evaluation of CNT coated HF membrane performance in these applications in comparison to traditional membrane materials (e.g. unmodified PES). Additionally, further morphological characterization of the CNT surface layer using more advanced techniques such as transmission electron microscopy or atomic force microscopy would provide interesting insights into the surface structure of a conductive, permeable coating.

## 2.7 References

- [1] G. Wei, S. Chen, X. Fan, X. Quan, H. Yu, Carbon nanotube hollow fiber membranes: High-throughput fabrication, structural control and electrochemically improved selectivity, *J. Memb. Sci.* 493 (2015) 97–105. <https://doi.org/10.1016/j.memsci.2015.05.073>.
- [2] A.J. Sutherland, M.X. Ruiz-Caldas, C.F. de Lannoy, Electro-catalytic microfiltration membranes electrochemically degrade azo dyes in solution, *J. Memb. Sci.* 611 (2020) 118335. <https://doi.org/10.1016/j.memsci.2020.118335>.
- [3] Q. Zhang, C.D. Vecitis, Conductive CNT-PVDF membrane for capacitive organic fouling reduction, *J. Memb. Sci.* 459 (2014) 143–156. <https://doi.org/10.1016/j.memsci.2014.02.017>.
- [4] N. Zhang, M.A. Halali, C.F. de Lannoy, Detection of fouling on electrically conductive membranes by electrical impedance spectroscopy, *Sep. Purif. Technol.* 242 (2020) 116823. <https://doi.org/10.1016/j.seppur.2020.116823>.
- [5] W. Duan, G. Chen, C. Chen, R. Sanghvi, A. Iddya, S. Walker, H. Liu, A. Ronen, D. Jassby, Electrochemical removal of hexavalent chromium using electrically conducting carbon nanotube/polymer composite ultrafiltration membranes, *J. Memb. Sci.* 531 (2017) 160–171. <https://doi.org/10.1016/j.memsci.2017.02.050>.
- [6] S.Y. Yang, C.D. Vecitis, H. Park, Electrocatalytic water treatment using carbon nanotube filters modified with metal oxides, *Environ. Sci. Pollut. Res.* 26 (2019) 1036–1043. <https://doi.org/10.1007/s11356-017-8495-6>.
- [7] Y. Liu, J.H. Dustin Lee, Q. Xia, Y. Ma, Y. Yu, L.Y. Lanry Yung, J. Xie, C.N. Ong, C.D. Vecitis, Z. Zhou, A graphene-based electrochemical filter for water purification, *J. Mater. Chem. A* 2 (2014) 16554–16562. <https://doi.org/10.1039/c4ta04006f>.

- [8] C.F. de Lannoy, D. Jassby, K. Gloe, A.D. Gordon, M.R. Wiesner, Aquatic biofouling prevention by electrically charged nanocomposite polymer thin film membranes, *Environ. Sci. Technol.* 47 (2013) 2760–2768. <https://doi.org/10.1021/es3045168>.
- [9] A. Ronen, W. Duan, I. Wheeldon, S. Walker, D. Jassby, Microbial Attachment Inhibition through Low-Voltage Electrochemical Reactions on Electrically Conducting Membranes, *Environ. Sci. Technol.* 49 (2015) 12741–12750. <https://doi.org/10.1021/acs.est.5b01281>.
- [10] B.S. Lalia, F.E. Ahmed, T. Shah, N. Hilal, R. Hashaikeh, Electrically conductive membranes based on carbon nanostructures for self-cleaning of biofouling, *Desalination*. 360 (2015) 8–12. <https://doi.org/10.1016/j.desal.2015.01.006>.
- [11] F.R. Omi, M.R. Choudhury, N. Anwar, A.R. Bakr, M.S. Rahaman, Highly Conductive Ultrafiltration Membrane via Vacuum Filtration Assisted Layer-by-Layer Deposition of Functionalized Carbon Nanotubes, *Ind. Eng. Chem. Res.* 56 (2017) 8474–8484. <https://doi.org/10.1021/acs.iecr.7b00847>.
- [12] A. V. Dudchenko, J. Rolf, K. Russell, W. Duan, D. Jassby, Organic fouling inhibition on electrically conducting carbon nanotube-polyvinyl alcohol composite ultrafiltration membranes, *J. Memb. Sci.* 468 (2014) 1–10. <https://doi.org/10.1016/j.memsci.2014.05.041>.
- [13] W. Duan, A. Dudchenko, E. Mende, C. Flyer, X. Zhu, D. Jassby, Electrochemical Mineral Scale Prevention and Removal on Electrically Conducting Carbon Nanotube - Polyamide Reverse Osmosis Membranes, *Environ. Sci. Process. Impacts.* 16 (2014) 1300–1308. <https://doi.org/10.31729/jnma.1240>.
- [14] J. Huang, Z. Wang, J. Zhang, X. Zhang, J. Ma, Z. Wu, A novel composite conductive microfiltration membrane and its anti-fouling performance with an external electric field in membrane bioreactors, *Sci. Rep.* 5 (2015) 1–8. <https://doi.org/10.1038/srep09268>.
- [15] L. Zhang, Y. Zhang, X. Zhang, Z. Li, G. Shen, M. Ye, C. Fan, H. Fang, J. Hu, Electrochemically controlled formation and growth of hydrogen nanobubbles, *Langmuir*. 22 (2006) 8109–8113. <https://doi.org/10.1021/la060859f>.
- [16] P.M. Doran, Membrane Filtration, in: *Bioprocess Eng. Princ.*, 2nd ed., Elsevier Ltd, Waltham, MA, 2013: pp. 493–526.
- [17] T. Matsuura, Synthetic Membranes and Membrane Separation Processes, in: *Synth. Membr. Membr. Sep. Process.*, CRC Press, Inc., Boca Raton, 1994: pp. 305–341.
- [18] L. Guo, Y. Jing, B.P. Chaplin, Development and Characterization of Ultrafiltration TiO<sub>2</sub> Magnéli Phase Reactive Electrochemical Membranes, *Environ. Sci. Technol.* 50 (2016) 1428–1436. <https://doi.org/10.1021/acs.est.5b04366>.
- [19] K.P. Katuri, N.M.S. Bettahalli, X. Wang, G. Matar, S. Chisca, S.P. Nunes, P.E. Saikaly, A Microfiltration Polymer-Based Hollow-Fiber Cathode as a Promising Advanced Material for Simultaneous Recovery of Energy and Water, *Adv. Mater.* 28 (2016) 9504–9511. <https://doi.org/10.1002/adma.201603074>.
- [20] D. Bell, R. Sengpiel, M. Wessling, Metallized hollow fiber membranes for electrochemical fouling control, *J. Memb. Sci.* 594 (2020) 117397. <https://doi.org/10.1016/j.memsci.2019.117397>.

- [21] K.P. Katuri, C.M. Werner, R.J. Jimenez-Sandoval, W. Chen, S. Jeon, B.E. Logan, Z. Lai, G.L. Amy, P.E. Saikaly, A novel anaerobic electrochemical membrane bioreactor (AnEMBR) with conductive hollow-fiber membrane for treatment of low-organic strength solutions, *Environ. Sci. Technol.* 48 (2014) 12833–12841. <https://doi.org/10.1021/es504392n>.
- [22] D. Liu, X. Chen, B. Bian, Z. Lai, Y. Situ, Dual-Function Conductive Copper Hollow Fibers for Microfiltration and Anti-biofouling in Electrochemical Membrane Bioreactors, *Front. Chem.* 6 (2018) 1–10. <https://doi.org/10.3389/fchem.2018.00445>.
- [23] K. Goh, L. Setiawan, L. Wei, W. Jiang, R. Wang, Y. Chen, Fabrication of novel functionalized multi-walled carbon nanotube immobilized hollow fiber membranes for enhanced performance in forward osmosis process, *J. Memb. Sci.* 446 (2013) 244–254. <https://doi.org/10.1016/j.memsci.2013.06.022>.
- [24] Y. Yang, S. Qiao, R. Jin, J. Zhou, X. Quan, A novel aerobic electrochemical membrane bioreactor with CNTs hollow fiber membrane by electrochemical oxidation to improve water quality and mitigate membrane fouling, *Water Res.* 151 (2019) 54–63. <https://doi.org/10.1016/j.watres.2018.12.012>.
- [25] G. Wei, J. Dong, J. Bai, Y. Zhao, Y. Li, Structurally Stable, Antifouling, and Easily Renewable Reduced Graphene Oxide Membrane with a Carbon Nanotube Protective Layer, *Environ. Sci. Technol.* 53 (2019) 11896–11903. <https://doi.org/10.1021/acs.est.9b03129>.
- [26] L. Du, X. Quan, X. Fan, G. Wei, S. Chen, Conductive CNT/nanofiber composite hollow fiber membranes with electrospun support layer for water purification, *J. Memb. Sci.* 596 (2020) 117613. <https://doi.org/10.1016/j.memsci.2019.117613>.
- [27] C. Cuevas, D. Kim, K.P. Katuri, P. Saikaly, S.P. Nunes, Electrochemically active polymeric hollow fibers based on poly(ether-b-amide)/carbon nanotubes, *J. Memb. Sci.* 545 (2018) 323–328. <https://doi.org/10.1016/j.memsci.2017.09.052>.
- [28] C.M. Werner, K.P. Katuri, A.R. Hari, W. Chen, Z. Lai, B.E. Logan, G.L. Amy, P.E. Saikaly, Graphene-Coated Hollow Fiber Membrane as the Cathode in Anaerobic Electrochemical Membrane Bioreactors - Effect of Configuration and Applied Voltage on Performance and Membrane Fouling, *Environ. Sci. Technol.* 50 (2016) 4439–4447. <https://doi.org/10.1021/acs.est.5b02833>.
- [29] J. Liu, C. Tian, J. Xiong, B. Gao, S. Dong, L. Wang, Polypyrrole vapor phase polymerization on PVDF membrane surface for conductive membrane preparation and fouling mitigation, *J. Chem. Technol. Biotechnol.* 93 (2018) 683–689. <https://doi.org/10.1002/jctb.5416>.
- [30] M. Mukherjee, S. De, Robust self cleaning polypyrrole-polysulfone blend hollow fiber membrane for biofouling mitigation, *J. Chem. Technol. Biotechnol.* 93 (2018) 3185–3198. <https://doi.org/10.1002/jctb.5675>.
- [31] H. Farrokhzad, T. Van Gerven, B. Van Der Bruggen, Preparation and characterization of a conductive polyaniline/polysulfone film and evaluation of the effect of co-solvent, *Eur. Polym. J.* 49 (2013) 3234–3243. <https://doi.org/10.1016/j.eurpolymj.2013.06.027>.

- [32] H. Kim, Y.S. Hwang, V.K. Sharma, Adsorption of antibiotics and iopromide onto single-walled and multi-walled carbon nanotubes, *Chem. Eng. J.* 255 (2014) 23–27. <https://doi.org/10.1016/j.cej.2014.06.035>.
- [33] P. Xie, C.F. de Lannoy, J. Ma, Z. Wang, S. Wang, J. Li, M.R. Wiesner, Improved chlorine tolerance of a polyvinyl pyrrolidone-polysulfone membrane enabled by carboxylated carbon nanotubes, *Water Res.* 104 (2016) 497–506. <https://doi.org/10.1016/j.watres.2016.08.029>.
- [34] B. Hinds, Dramatic transport properties of carbon nanotube membranes for a robust protein channel mimetic platform, *Curr. Opin. Solid State Mater. Sci.* 16 (2012) 1–9. <https://doi.org/10.1016/j.cossms.2011.05.003>.
- [35] C.F. de Lannoy, D. Jassby, D.D. Davis, M.R. Wiesner, A highly electrically conductive polymer-multiwalled carbon nanotube nanocomposite membrane, *J. Memb. Sci.* 415–416 (2012) 718–724. <https://doi.org/10.1016/j.memsci.2012.05.061>.
- [36] L. Liu, F. Zhao, J. Liu, F. Yang, Preparation of highly conductive cathodic membrane with graphene (oxide)/PPy and the membrane antifouling property in filtrating yeast suspensions in EMBR, *J. Memb. Sci.* 437 (2013) 99–107. <https://doi.org/10.1016/j.memsci.2013.02.045>.
- [37] M.A. Halali, C.F. De Lannoy, The Effect of Cross-Linkers on the Permeability of Electrically Conductive Membranes, *Ind. Eng. Chem. Res.* 58 (2019) 3832–3844. <https://doi.org/10.1021/acs.iecr.8b05691>.
- [38] L. Song, M. Elimelech, Particle deposition onto a permeable surface in laminar flow, *J. Colloid Interface Sci.* 173 (1995) 165–180. <https://doi.org/10.1006/jcis.1995.1310>.
- [39] J. Altmann, S. Ripperger, Particle deposition and layer formation at the crossflow microfiltration, *J. Memb. Sci.* 124 (1997) 119–128. [https://doi.org/10.1016/S0376-7388\(96\)00235-9](https://doi.org/10.1016/S0376-7388(96)00235-9).
- [40] A. Bogler, A. Kastl, M. Spinnler, T. Sattelmayer, A. Be’er, E. Bar-Zeev, Where, when and why? Quantifying the relation of particle deposition to crossflow velocity and permeate water flux in forward osmosis, *J. Memb. Sci.* 604 (2020) 118055. <https://doi.org/10.1016/j.memsci.2020.118055>.
- [41] D.C. Choi, S.Y. Jung, Y.J. Won, J.H. Jang, J. Lee, H.R. Chae, K.H. Ahn, S. Lee, P.K. Park, C.H. Lee, Three-dimensional hydraulic modeling of particle deposition on the patterned isopore membrane in crossflow microfiltration, *J. Memb. Sci.* 492 (2015) 156–163. <https://doi.org/10.1016/j.memsci.2015.05.054>.
- [42] S. Kang, M. Herzberg, D.F. Rodrigues, M. Elimelech, Antibacterial effects of carbon nanotubes: Size does matter!, *Langmuir.* 24 (2008) 6409–6413. <https://doi.org/10.1021/la800951v>.
- [43] A.S. Kazemi, L. Boivin, S. Mi Yoo, R. Ghosh, D.R. Latulippe, Elucidation of filtration performance of hollow-fiber membranes via a high-throughput screening platform, *J. Memb. Sci.* 533 (2017) 241–249. <https://doi.org/10.1016/j.memsci.2017.03.042>.
- [44] Haldor Topsoe, Geometric factors in four point resistivity measurement, 2nd ed., Vedbaek,

1968.

- [45] K.G. Dassios, P. Alafogianni, S.K. Antiohos, C. Leptokaridis, N.M. Barkoula, T.E. Matikas, Optimization of sonication parameters for homogeneous surfactant assisted dispersion of multiwalled carbon nanotubes in aqueous solutions, *J. Phys. Chem. C*. 119 (2015) 7506–7516. <https://doi.org/10.1021/acs.jpcc.5b01349>.
- [46] A.I. Radu, M.S.H. van Steen, J.S. Vrouwenvelder, M.C.M. van Loosdrecht, C. Picioreanu, Spacer geometry and particle deposition in spiral wound membrane feed channels, *Water Res.* 64 (2014) 160–176. <https://doi.org/10.1016/j.watres.2014.06.040>.
- [47] E.J. Petersen, D.X. Flores-Cervantes, T.D. Bucheli, L.C.C. Elliott, J.A. Fagan, A. Gogos, S. Hanna, R. Kägi, E. Mansfield, A.R.M. Bustos, D.L. Plata, V. Reipa, P. Westerhoff, M.R. Winchester, Quantification of Carbon Nanotubes in Environmental Matrices: Current Capabilities, Case Studies, and Future Prospects, *Environ. Sci. Technol.* 50 (2016) 4587–4605. <https://doi.org/10.1021/acs.est.5b05647>.
- [48] D. Di Carlo, Inertial microfluidics, *Lab Chip*. 9 (2009) 3038–3046. <https://doi.org/10.1039/b912547g>.
- [49] J.M. Martel, M. Toner, Inertial Focusing in Microfluidics, *Annu. Rev. Biomed. Eng.* 16 (2014) 371–396. <https://doi.org/10.1146/annurev-bioeng-121813-120704>.
- [50] Y. Gou, Y. Jia, P. Wang, C. Sun, Progress of inertial microfluidics in principle and application, *Sensors (Switzerland)*. 18 (2018). <https://doi.org/10.3390/s18061762>.
- [51] M. Gholami, S. Nasserri, C.Y. Feng, T. Matsuura, K.C. Khulbe, The effect of heat-treatment on the ultrafiltration performance of polyethersulfone (PES) hollow-fiber membranes, *Desalination*. 155 (2003) 293–301. [https://doi.org/10.1016/S0011-9164\(03\)00307-2](https://doi.org/10.1016/S0011-9164(03)00307-2).
- [52] A. Saraf, K. Johnson, M.L. Lind, Poly(vinyl) alcohol coating of the support layer of reverse osmosis membranes to enhance performance in forward osmosis, *Desalination*. 333 (2014) 1–9. <https://doi.org/10.1016/j.desal.2013.11.024>.
- [53] B. Bolto, T. Tran, M. Hoang, Z. Xie, Crosslinked poly(vinyl alcohol) membranes, *Prog. Polym. Sci.* 34 (2009) 969–981. <https://doi.org/10.1016/j.progpolymsci.2009.05.003>.
- [54] K. Lang, S. Sourirajan, T. Matsuura, G. Chowdhury, A study on the preparation of polyvinyl alcohol thin-film composite membranes and reverse osmosis testing, *Desalination*. 104 (1996) 185–196.
- [55] S. Kim, M. Marion, B.H. Jeong, E.M.V. Hoek, Crossflow membrane filtration of interacting nanoparticle suspensions, *J. Memb. Sci.* 284 (2006) 361–372. <https://doi.org/10.1016/j.memsci.2006.08.008>.
- [56] N.G. Sahoo, S. Rana, J.W. Cho, L. Li, S.H. Chan, Polymer nanocomposites based on functionalized carbon nanotubes, *Prog. Polym. Sci.* 35 (2010) 837–867. <https://doi.org/10.1016/j.progpolymsci.2010.03.002>.
- [57] L.M. Robeson, Correlation of separation factor versus permeability for polymeric membranes, *J. Memb. Sci.* 62 (1991) 165–185. [https://doi.org/10.1016/0376-7388\(91\)80060-J](https://doi.org/10.1016/0376-7388(91)80060-J).

- [58] A. Mehta, A.L. Zydney, Permeability and selectivity analysis for ultrafiltration membranes, *J. Memb. Sci.* 249 (2005) 245–249. <https://doi.org/10.1016/j.memsci.2004.09.040>.
- [59] G.M. Geise, H.B. Park, A.C. Sagle, B.D. Freeman, J.E. McGrath, Water permeability and water/salt selectivity tradeoff in polymers for desalination, *J. Memb. Sci.* 369 (2011) 130–138. <https://doi.org/10.1016/j.memsci.2010.11.054>.
- [60] C. Buelke, A. Alshami, J. Casler, Y. Lin, M. Hickner, I.H. Aljundi, Evaluating graphene oxide and holey graphene oxide membrane performance for water purification, *J. Memb. Sci.* 588 (2019) 117195. <https://doi.org/10.1016/j.memsci.2019.117195>.

## 2.8 Supplementary Information

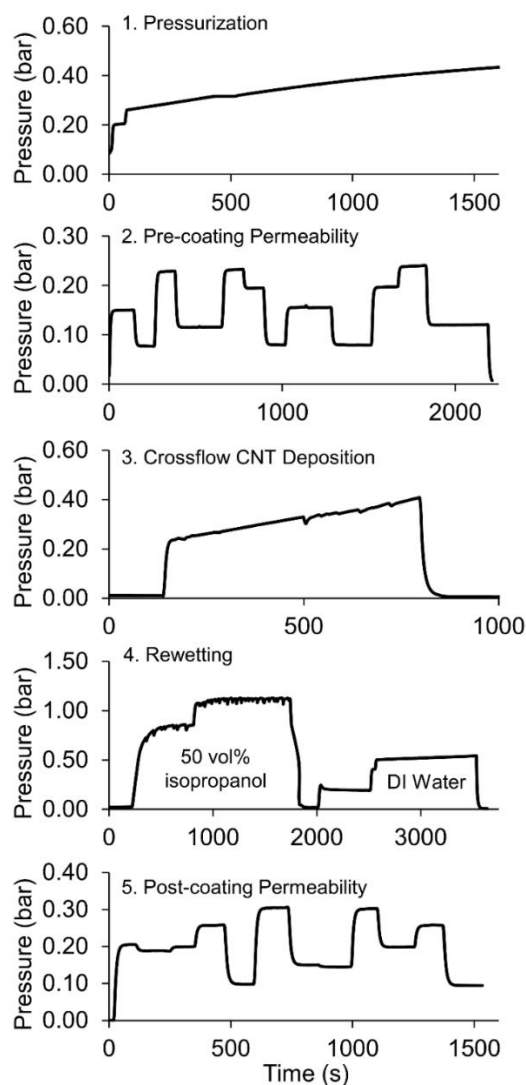


**Figure 2.S1.** Sample feed pressure profiles for one PES HF membrane coated at a crossflow velocity of 1.06 cm/s, feed pressure of 0.2 bar and feed CNT concentration of 7.5 mg/L. Feed pressure was measured every 3 seconds via USB transducer at each of the following preparation stages: 1) pressurization 2) pre-coating permeability measurement 3) crossflow CNT deposition 4) rewetting first with 50 vol% isopropanol then with DI water and 5) post-coating permeability measurement.

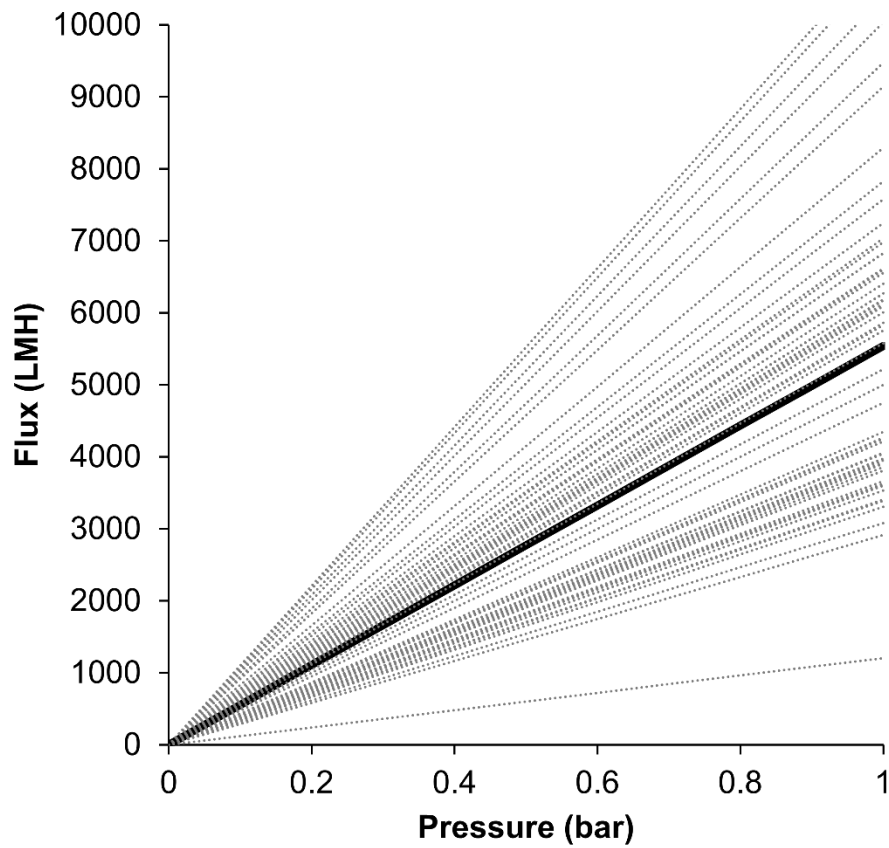


**Figure 2.S2.** Collection of all 62 hydraulic permeability measurements for the unmodified PES HF membranes throughout the experimental study. The minimum and maximum values are 1,204 and 11,039 LMH/bar. The thick black line corresponds to the average of all 61 measurements of 5,540 LMH/bar.

## a) Permeability P-values

		0.1 bar				0.2 bar	
		PVA&		0.32 cm/s	1.06 cm/s	0.32 cm/s	1.06 cm/s
		Heat	Heat				
0.1 bar	Heat	-					
	PVA & Heat	0.007	-				
	0.32 cm/s	0.238	0.000	-			
	1.06 cm/s	0.005	0.105	0.002	-		
0.2 bar	0.32 cm/s	0.313	0.000	0.767	0.002	-	
	1.06 cm/s	0.023	0.922	0.005	0.152	0.006	-

## b) Conductivity P-values

		0.1 bar		0.2 bar	
		0.32 cm/s	1.06 cm/s	0.32 cm/s	1.06 cm/s
0.1 bar	0.32 cm/s	-			
	1.06 cm/s	0.000	-		
0.2 bar	0.32 cm/s	0.027	0.000	-	
	1.06 cm/s	0.000	0.000	0.000	-

**Figure 2.S3.** P-value statistics from a series of two sample T-tests comparing coating membrane **a)** permeabilities and **b)** conductivities with the null hypothesis that sample means are equal. Values are read by matching conditions along the horizontal and vertical axes. Only the lower matrix is included due to the symmetry of the full matrix. Points where the null hypothesis is rejected ( $p < 0.05$ ) are shaded to indicate a statistically significant difference between these measured values. Experiments included:  $2^2$  DOE test conditions and permeabilities for two controls: “heat” control testing the curing process with no prior crossflow deposition and “PVA & Heat” control testing both crossflow deposition and curing excluding CNTs from the feed suspension.

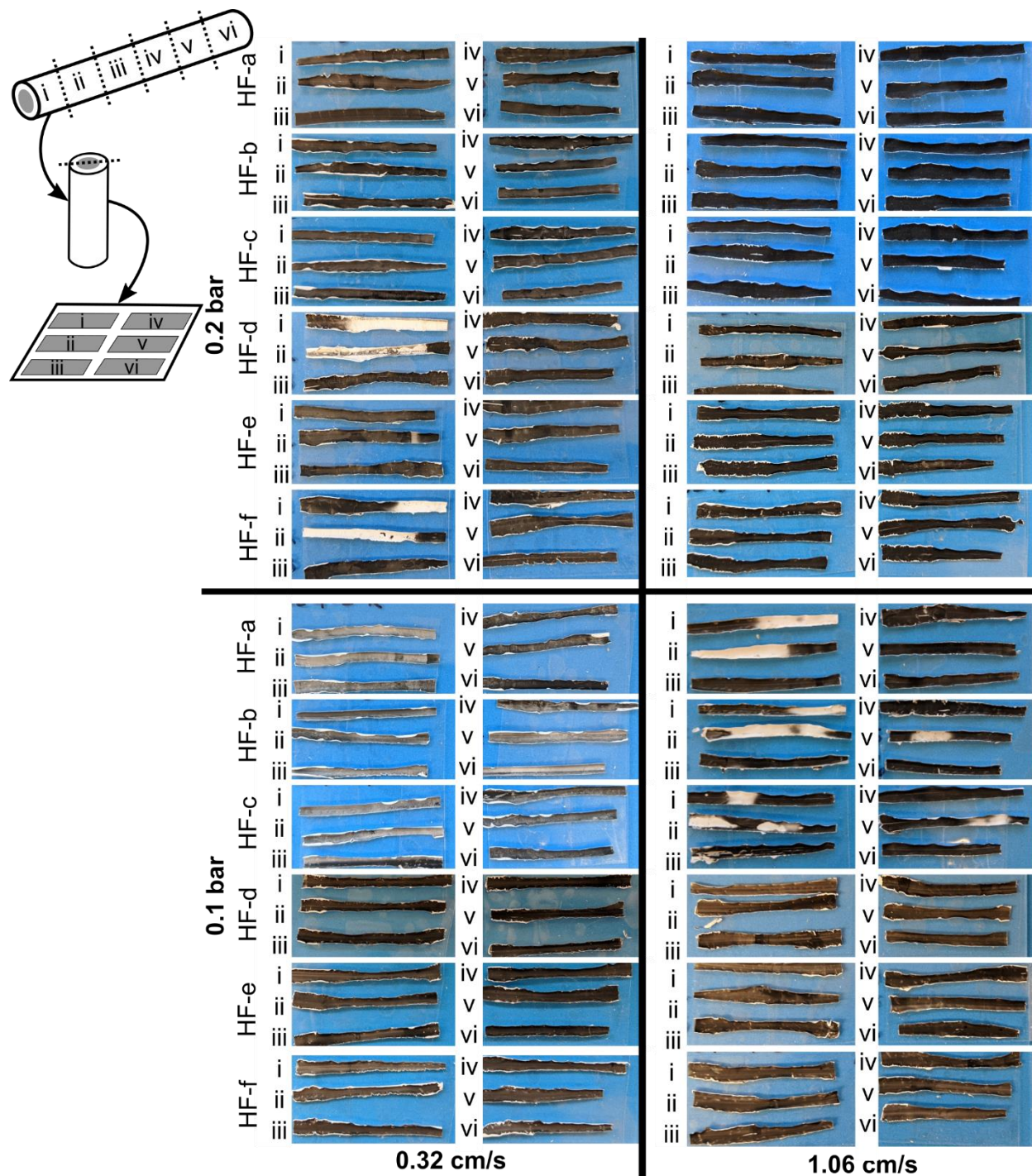


**Figure 2.S4.** Photos of the six HF membranes prepared at each of the crossflow velocity and pressure conditions studied in the  $2^2$  full factorial DOE. The cartoon on the left shows how each HF was cut into six segments, cut in half and folded open prior to imaging. The six segments are identified from inlet (i) to outlet (vi) on each of the HF images.

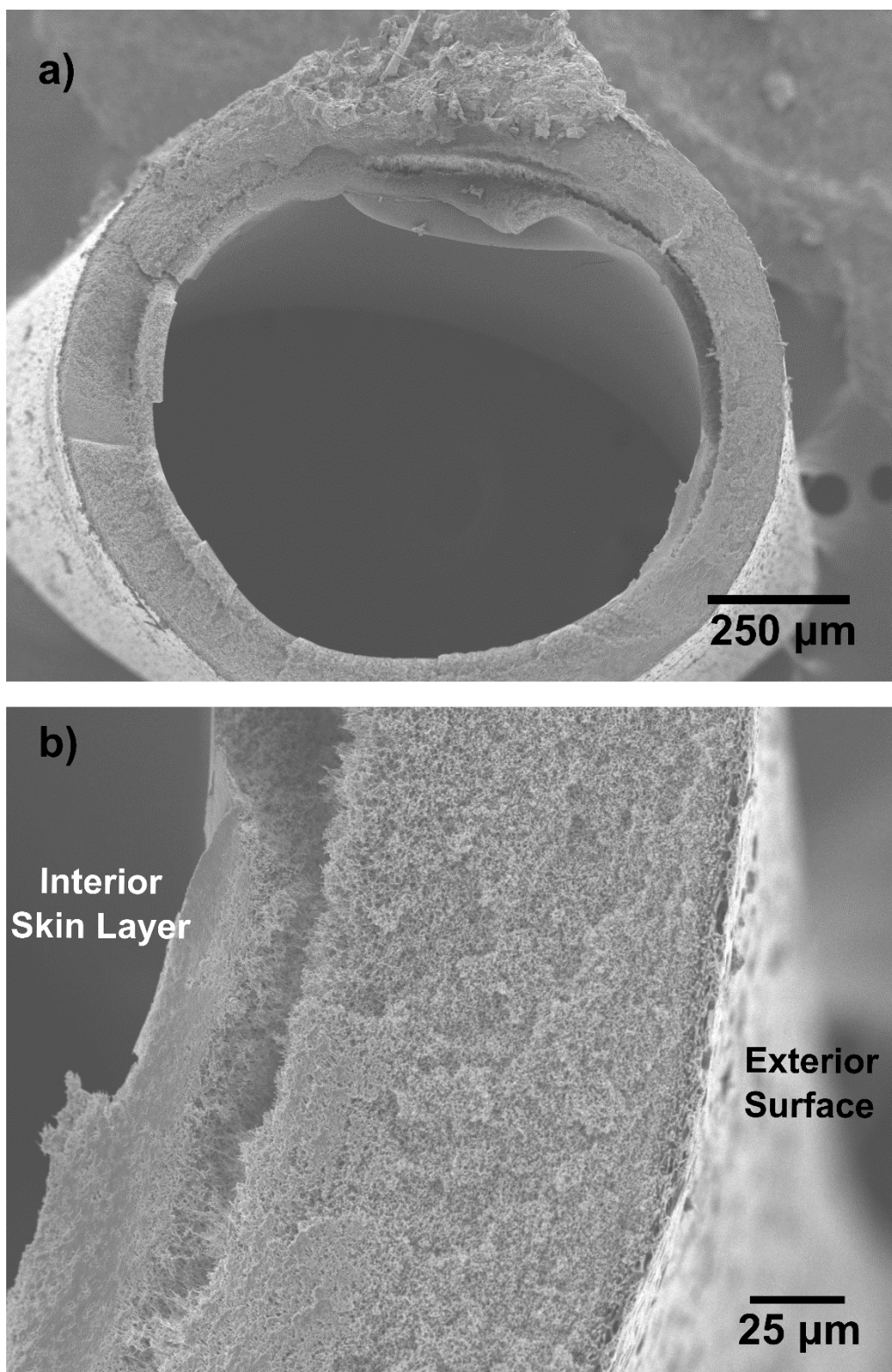


**Figure 2.S5.** Scanning Electron Microscopy (SEM) images of the unmodified PES HF membranes shown in cross-section at low magnification (a) for context and high magnification (b) to illustrate the interior skin layer and bulk porous layer.

**Table 2.S1.** Design-of-experiments multiple linear regression model coefficients, p-values and  $R^2$  for two responses: permeability and conductivity. Coefficients were calculated for each input variable (pressure, crossflow velocity) and the interaction parameter (pressure  $\times$  velocity).

Response \ Input	Pressure (bar)		Crossflow Velocity (cm/s)		Interaction (P $\times$ v)		Model $R^2$
	Coefficient	P-value	Coefficient	P-value	Coefficient	P-value	
Permeability (LMH/bar)	731	0.580	3482	0.000	539	0.920	0.9106
Permeability (LMH/bar) – Reduced Terms	0	N/A	3575	0.000	0	N/A	0.9089
Conductivity (S/m)	-1384	0.000	-137.9	0.000	5361	0.000	0.8241

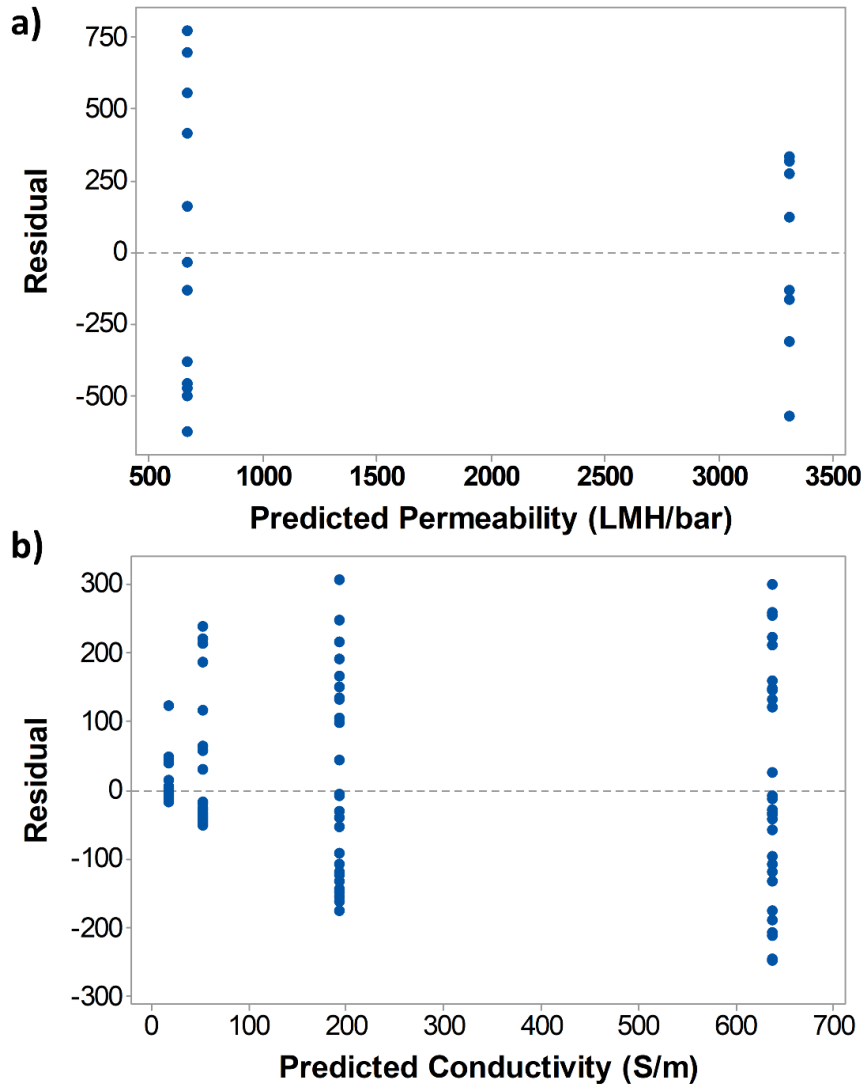


**Figure 2.S6.** Residual plots for the multiple linear regression models of a) permeability and b) conductivity from the  $2^2$  full factorial Design-of-Experiments model evaluating two flow parameters: feed pressure and crossflow velocity.

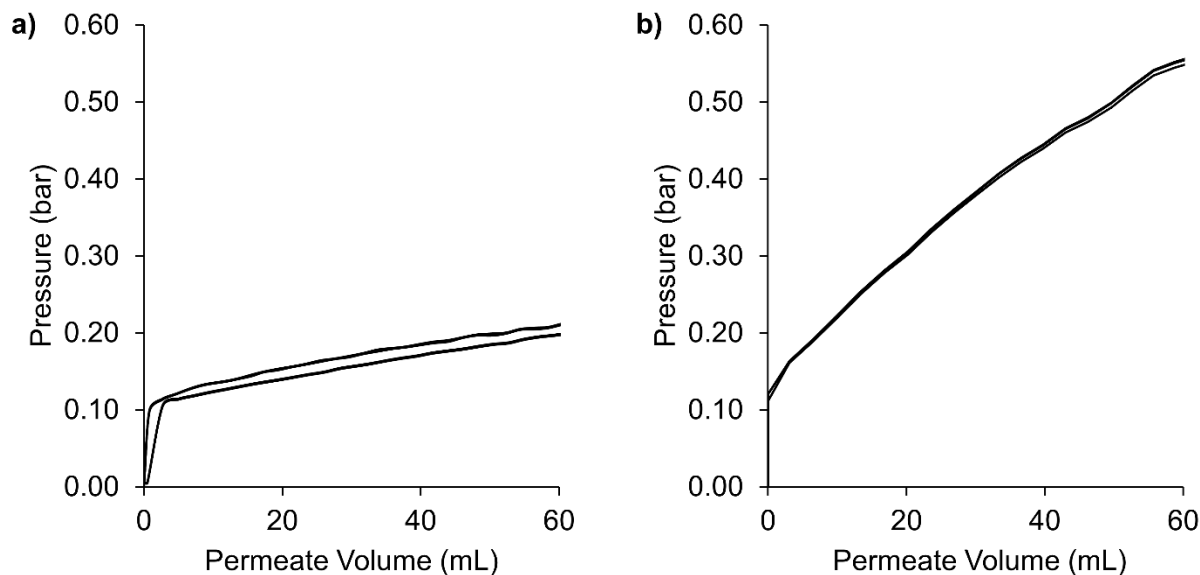


**Figure 2.S7.** Crossflow deposition pressure profiles at a crossflow velocity of 0.32 cm/s and feed pressure of 0.1 bar for two different feed concentrations: a) 7.5 mg/L CNTs b) 18.75 mg/L CNTs.

**Table 2.S2.** Measured CNT-coated HF membrane permeabilities and surface conductivities used to develop the upper limit line in the Robeson-like plot (Fig. 2.7). Model parameters ( $k$ ,  $n$ ) were determined by fitting an equation of the form  $C = kL_p^n$  to the data points below where  $C$  is the conductivity, and  $L_p$  is the permeability. Parameters were then manually adjusted such that the residual values were negative for all the fitted data points. Conductivities predicted using the upper limit equation  $C = 1.27 \times 10^{10} \cdot L_p^{-2.00}$  are included below along with their corresponding residuals.

Permeability (LMH/bar)	Measured Conductivity (S/m)	Predicted Conductivity (S/m)	Residuals (S/m)
6451.12	242.38	296.47	-54.09
3644.57	470.81	930.44	-459.63
3626.28	586.67	939.87	-353.20
3430.58	587.47	1050.33	-462.85
3143.49	769.89	1251.26	-481.37
3001.06	830.86	1373.03	-542.17
2590.22	1478.72	1843.94	-365.22
2417.17	1887.27	2117.84	-230.58

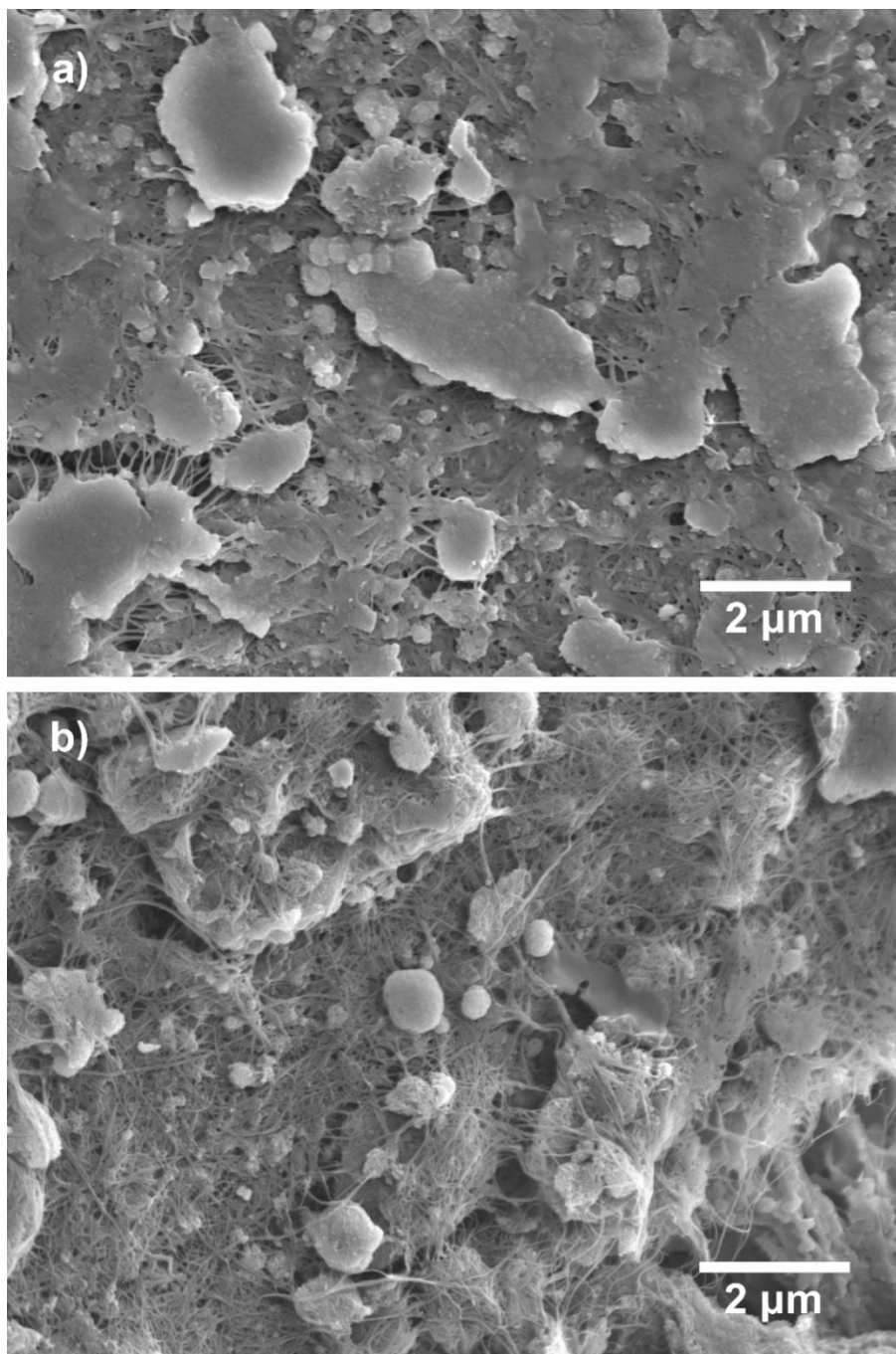


**Figure 2.S8.** High magnification Scanning Electron Microscopy (SEM) images of the interior surface of two CNT coated HF membranes shown in Fig. 2.5. Image A corresponds to the CNT-coated HF membrane produced at a deposition feed pressure of 0.2 bar, crossflow velocity of 1.06 cm/s, and feed concentration of 7.5 mg/L CNTs (shown in Fig. 2.5 c, d). Image B corresponds to the CNT-coated HF membrane produced at a deposition feed pressure of 0.1 bar, crossflow velocity of 0.32 cm/s, and feed concentration of 18.8 mg/L CNTs (shown in Fig. 2.5 e, f).

## **Chapter 3: A universal method for evaluating electrically conductive membrane performance: comparative review of the conductivity/ permeability trade-off**

Authors: Melissa J. Larocque, Adi Gelb, David R. Latulippe, Charles-François de Lannoy

### **3.1 Preface**

In this chapter, the conductivity/ permeability trade-off established in Chapter 2 is explored further across the electrically conductive membrane (ECM) field using data for 80 membranes collected from 38 different papers. Deposition-based synthesis techniques for ECMs involve a build-up of a conductive layer on the surface of support membranes; generally, more conductive material increases the conductivity of this surface layer but restricts flux through the membrane. This effect was obvious in Chapter 2 where an inverse relationship was noted between surface conductivity and hydraulic permeability for the carbon nanotube (CNT) coated hollow fiber membranes. Both the selected flow parameters and particle loadings had a significant impact on the magnitude of this trade-off. However, CNT-based coatings represent a small sub-set of the field of ECMs. As mentioned in Chapter 1, ECMs have been developed using various conductive materials (i.e. graphitic nanomaterials, metals, conductive polymers) and for various separation types (i.e. MF/UF/NF/RO/FO), configurations (i.e. flat sheet, hollow fiber, tubular), and applications (i.e. antifouling, redox, enhanced separations). The results from this chapter confirm a similar conductivity/ permeability trade-off exists across the field of ECMs, the magnitude of which varies depending on the parameters listed above.

### 3.2 Abstract

Electrically conductive membranes (ECMs) are developed using many types of conductive materials and fabrication methods intended for specific applications in fouling mitigation, enhanced selectivity, electrochemical degradation of contaminants, and sensing. Given the wide diversity of materials and applications, comparing ECM performance is a significant challenge. Surface conductivity and hydraulic permeability are two key metrics commonly used to quantify ECM performance but are often linked in an inherent trade-off. Similar trade-offs exist in other fields of membrane science, with the most notable being the permeability/ selectivity trade-off first illustrated in the gas separation membrane field by Robeson. In this work, we present a method for quantifying the trade-off between ECM surface conductivity and permeability. Conductivity and permeability data were collected from 38 ECM papers and plotted against each other in a series of log-log plots organized by the type of conductive material used in fabrication: graphitic nanomaterials, metals, and conductive polymers. These figures clearly illustrated the conductivity/ permeability trade-off, which was quantified by fitting upper limit models for each type of conductive material. Metallic-based ECMs out-performed the other two material classes with the highest conductivities (three orders of magnitude greater) and comparable permeabilities; however, these membranes largely consisted of high flux microfiltration applications (~68% of data for metallic-based ECMs) which partially explains the greater ability to maintain both high permeability and conductivity. A wide variety of conditions were used to test ECMs, with 35 unique pollutants tested across 63 different experiments. This variety of conditions makes ECM performance comparisons challenging. Further, this analysis revealed that limited ECM research has been conducted using realistic feed sources (e.g. municipal wastewater). The conductivity/ permeability plots developed herein present a standardized approach for evaluating ECM

performance and will be useful for making ECM design decisions to target specific performance levels.

### 3.3 Introduction

Membrane separation technologies are ubiquitous in municipal and industrial wastewater treatment; however, current commercial technologies are susceptible to fouling and scaling in long-term operations and are limited to a single mechanism for removal. This mechanism is typically size exclusion for removal of bacteria and large particles (e.g. microfiltration (MF) and ultrafiltration (UF)) or diffusivity for ion and small particle removal (e.g. nanofiltration (NF), reverse osmosis (RO)). Additionally, while contaminants are removed from feed waters, they are not chemically degraded, thus concentrating and transferring contaminants from one system to another and potentially re-introducing them to the environment. Electrically conductive membranes (ECMs) have drawn significant interest for their ability to address these challenges. Specifically, ECMs present the following benefits: 1) coupling of size exclusion and electrochemical effects (electrostatic repulsion, pH change) for enhanced removal [1,2], 2) high propensity for mitigating surface fouling (i.e. biofouling [3,4], organic matter [5,6], and scaling [7]), and 3) facilitating electrochemical degradation of contaminants (e.g. phenol [8–10], tetracycline [10], nitrobenzene [11])

ECMs have been developed from a variety of conductive materials, either cast directly into porous structures or used in composites with traditional membrane materials such as polymers (e.g. polyether sulfone [8,12,13], polyvinylidene fluoride [5,11,14,15]) or ceramics [16]. These generally include three major classes of conductive materials: 1) graphitic nanomaterials (e.g. carbon nanotubes (CNTs) [1,4,5–7,10,11,13–15,16–25], graphene [10,26], graphite [27]); 2) metals (e.g. nickel [12], copper [28], titanium oxide [9,29,30]); 3) conductive polymers (e.g.

polypyrrole [31], polyaniline [19,21,23,27,32–34]). ECMs have also been developed for a variety of separation types (e.g. MF, UF, NF, RO, and forward osmosis (FO)), and membrane configurations (e.g. flat sheet, hollow fiber, tubular).

Fabrication methods for developing ECMs are widely varied even within a specific type of conductive material. For example, CNT-based ECMs are often vacuum or pressure-deposited onto a support membrane [4,6,7,10,13,15,16,18–21], but they have also been cast directly into membrane structures to either create a composite CNT-polymeric membrane [5,11] or a porous self-supported CNT network [1]. Metallic-based ECMs have been developed using a variety of specialized techniques including electrospraying [9], sputter coating [35], electroless plating [36] or atomic layer deposition [30]. Conductive polymers have been polymerized directly at the surface of a support membrane [19,31], cast onto a support membrane via phase inversion [27], or incorporated into the casting solution with a traditional membrane polymer [34]. Additionally, multiple conductive materials have been incorporated into ECMs such as CNT/polyaniline [19,21,23] or graphene/nickel [26] composites developed using combinations of these techniques.

It is difficult to compare membrane performance given the wide diversity in ECM fabrication methods and the lack of a standardized method for evaluating ECM performance. ECM surface conductivity differentiates them from conventional membranes and is the property that enables electro-active effects under an applied potential, such as electrostatic repulsion [1] and reactive oxygen species generation [37]. ECM surface conductivity must be sufficiently high to enable a current to flow across the membrane while submerged in electrolytes, such as wastewater or seawater. Depending on the intended application, ECM surfaces must also exhibit high capacitance, and therefore high conductivity. In most configurations, the ECM is considered the working electrode and a counter electrode is positioned nearby, establishing an electrochemical

cell. The ECM must have a high capacitance, and thus a high electrical conductivity, in order to generate a high surface charge, necessary to engage in electrostatic repulsion of ions and electrochemical reactions.

ECM permeability or water flux, as with all membranes, must also be high for industrial applicability. As most ECMs are formed by modifying existing polymer membranes, it is imperative to minimize the permeability loss of ECMs in comparison to the original polymer membrane. Surface conductivity and hydraulic permeability have been shown to be related, particularly with deposition-based methods as greater conductive material deposition tends to increase conductivity, while blocking pores and reducing membrane permeability [36].

In the gas separation membrane field, Robeson first presented a simple graphical method for comparing membrane performance across various membrane materials and intended applications [38]. The trade-off between desired species permeability and selectivity was established in a series of log-log plots and an upper bound was defined to describe the maximum attainable combinations of permeability and selectivity for various gas separation membrane technologies. A similar approach has since been applied to other fields of membrane science including protein purification [39] and desalination [40,41].

In our previous work, we presented an analogous “Robeson plot” to quantify the trade-off between surface conductivity and hydraulic permeability for ECMs that we synthesized composed of CNTs [36]. The objectives of this short review are: 1) to extend this approach to explore the conductivity/ permeability trade-off for various conductive materials used in fabrication; 2) quantify this trade-off by fitting upper limit models for the three major classes of conductive materials (i.e. graphitic nanomaterials, metals, conductive polymers); 3) critically compare

membrane performance while acknowledging the diversity in ECM fabrication in terms of conductive materials, separation type, membrane configuration, and intended application.

### 3.4 Literature Review & Methodology

A thorough literature review was conducted to ensure the collected data was representative of the current state of the electrically conductive membrane (ECM) field. All permutations of the following list of keywords were used to search for appropriate journal articles in the Web of Science academic database: electrically conductive, membrane filtration, metal (nickel, copper, titanium, tin, aluminum, gold), conductive polymer (polypyrrole, polyaniline, polyacetylene, polythiophene), carbon nanomaterial (graphite, graphene, carbon nanotube, carbon nanofiber), microfiltration, ultrafiltration, nanofiltration, reverse osmosis and forward osmosis. For example, the generic keywords “electrically conductive,” and “membrane filtration,” were combined with a more specific identifier such as “graphene,” in an individual search. In this process we found 93 relevant papers, 30 of which had only partial data (either they reported conductivity (S/m) or permeability (LMH/bar), but not both), and 25 of which reported neither. The remaining 38 papers contained both conductivity (S/m) (or resistivity ( $\Omega\text{m}$ ), sheet resistance ( $\Omega/\text{sq}$ ) and conductive layer thickness (m), or sheet conductance (S/m) and conductive layer thickness (m)) and permeability (LMH/bar) data for 80 different membranes in total which were used for the creation of a series of “Robeson-like” plots. Only 41% of the papers reviewed reported sufficient data for proper comparison. This indicates a significant dearth of proper reporting of standard properties, which we discuss in Section 3.

Surface conductivity and permeability data were obtained directly from the papers reviewed, with minor unit conversions required to report consistently in terms of S/m and LMH/bar, respectively. Various methods were used in the 38 papers reviewed to measure surface

conductivity including the four-point probe method [1,2,4,6,7,12,13,15–19,21,24,25,27,28,30–33,35,41], a two-probe method [10,23], using a digital multimeter [5,11], a potentiostat [14] and electrical impedance spectroscopy [9,22,26,29,37,42,43] (methods not reported in: [8,20,34]). In cases where only sheet resistance ( $R$ ) was reported [2,7,10,12,19,23,26,28,30,31,34,37] in  $\Omega/\text{sq}$ , surface conductivity ( $\sigma$ ) in S/m was calculated using the thickness ( $t$ ) of the conductive layer in Equation 1:

$$\sigma = \frac{1}{R \times t} \quad (1)$$

Pure water permeabilities were reported for the majority of the 38 papers. In several cases, permeability was not reported directly, but was calculated using the initial flux and pressure values provided for fouling and rejection experiments [4,6,9,12,22,26,30,32]. Numerical data was obtained directly from the text or tables where available. If only figures were provided without corresponding values reported in the text, GetData Graph Digitizer software was used to estimate the values of conductivity and/or permeability (or flux) from the graph based on the axes' scale and values provided.

### **3.5 Comparing Electrically Conductive Membrane (ECM) Properties, Materials and Applications**

#### *3.5.1 Establishing the conductivity/permeability trade-off for various conductive materials*

To establish the membrane performance trade-off between permeability and conductivity, we created a series of Robeson-like plots comparing permeability (x-axis) to conductivity (y-axis) for 80 different membranes from 38 papers. These plots are included in Fig. 3.1 and organized according to the class of conductive material used in membrane fabrication, with legend entries identifying the specific material used: a) graphitic nanomaterials; b) metals; and c) conductive

polymers. Composite materials belonging to more than one class are shown in each applicable panel. The general inverse relationship between permeability and conductivity is immediately apparent. For the graphitic nanomaterial-based membranes presented in Fig. 3.1a, membranes with conductivities above 10-100 S/m had permeabilities lower than 1000 LMH/bar; however, a decrease in membrane conductivities corresponded to membranes with higher permeabilities such that membranes with conductivities in the range of 0.1-1 S/m when demonstrated permeabilities greater than 1000 LMH/bar. This inverse relationship between conductivity and permeability followed an approximate log-log relationship, as presented in Figure 1a. Similar inverse log-log trends were observed for polymeric (Fig. 3.1c) and to a lesser extent metallic-based (Fig. 3.1b) conductive membranes.

Substantial differences in the achievable conductivity and permeability values between conductive material classes were evident. Use of metallics for ECM fabrication resulted in conductivities up to  $1.00 \times 10^7$  S/m [35] and permeabilities up to  $4.36 \times 10^4$  LMH/bar [9]. ECMs fabricated with graphitic nanomaterials had the next highest values with conductivities up to  $4.01 \times 10^4$  S/m [25] and permeabilities up to  $9.00 \times 10^4$  LMH/bar [24]. Membranes composed of conductive polymers alone, had both lower conductivities, with a maximum conductivity of  $7.71 \times 10^2$  S/m [32], and lower permeabilities, with maximum permeability of  $5.69 \times 10^2$  LMH/bar [31]. Membranes composed of composites containing conductive polymers and graphitic nanomaterials, such as carbon nanotube/ polyaniline based conductive membranes, yielded higher conductivities and permeabilities with a maximum conductivity of  $8.93 \times 10^3$  S/m [19] and maximum permeability of  $1.02 \times 10^4$  LMH/bar [23]. The maximal values achieved with the polymer/ graphitic nanomaterial composite approach were comparable with graphitic

nanomaterials alone, suggesting that there was no advantage to using conductive polymers with respect to a membrane's conductivity and permeability.

To quantify the inverse relationship between hydraulic permeability ( $L_p$ ) and conductivity ( $C$ ), an upper performance limit (see Fig. 3.1, black line) was established for each class of conductive material using a process similar to that of Robeson's original work [38]. A model of the form:  $C = kL_p^n$  was fitted to select data (see Table 3.S1 to 3.S4) and model parameters ( $k$ ,  $n$ ) were then manually adjusted such that the residual values were negative for all fitted data points. Fitted models were as follows: a)  $C = 8.79 \times 10^9 L_p^{-1.91}$  for graphitic nanomaterial-based ECMs; b)  $C = 9.07 \times 10^{21} L_p^{-3.88}$  for metallic-based ECMs; c)  $C = 1.11 \times 10^8 L_p^{-1.35}$  for ECMs containing conductive polymers and  $C = 1.29 \times 10^6 L_p^{-2.17}$  when composite materials were excluded. Model parameters for ECMs developed using graphitic nanomaterials were similar in magnitude to that of the composite polymer/ graphitic nanomaterial based ECMs, which further emphasizes the similarities in the conductivity/ permeability trade-off for these two types of ECMs. Model parameters were substantially larger for the metallic-based ECMs which were required to describe the significant increase observed in both conductivity and permeability compared to the other two classes of conductive materials.

Although metallic-based ECMs offered the best performance in terms of conductivity/ permeability, graphitic nanomaterials offer several other unique advantages. In addition to electrochemical effects, graphitic nanomaterials have a high adsorptive capacity [44], inherent, passive antimicrobial properties [45], and catalytic activity [22] useful for removing or degrading contaminants. Conductivity is not the only significant electrochemical property for evaluating ECM performance. For example, although high conductivity indicates the surface serves as a good capacitor for inducing electrostatic repulsion, electrochemical reactivity better describes the ability

of the ECM to achieve efficient electrochemical degradation of contaminants. Furthermore, fabrication methods for metallic-based ECMs often involve specialized equipment (e.g. sputter coating [35]), strong reducing agents (e.g. sodium borohydride [12]) or energy intensive, high temperature reductive steps [42]. In comparison, simple pressure or vacuum deposition techniques are commonly used for graphitic nanomaterial-based ECM fabrication [4,6,7,10,13,15,16,18–21]. Metallic-based ECMs are useful for high conductivity/ high flux applications but graphitic nanomaterials should not be discounted due to their additional functionalities and simple fabrication techniques.

It is highly probable that the conductivity/permeability trade-off exists as a result of the inherent challenges associated with making a porous conductive thin film. Since pores are not electrically conductive, the greater the surface porosity, the lower the surface conductance. Further, greater conductivity is achievable with more conductive material. More conductive material deposited on the surface of a membrane, occludes the supporting membrane's pores more severely, thereby reducing the membrane permeability. While material requirements associated with making porous conductive materials is likely a fundamental limit, there are still great gains achievable with new materials (e.g. 2D conductive materials, the new generation of conductive polymers) and advanced synthesis techniques (e.g. atomic layer deposition, 3D printing, micropatterning). As such, we hypothesize that the upper bounds we have identified here are not permanent and will continually be surpassed as the pace of new ECM research continues to accelerate. Rather, these current upper bounds are goalposts to aim for, helping researchers compare their results with those that have come before.

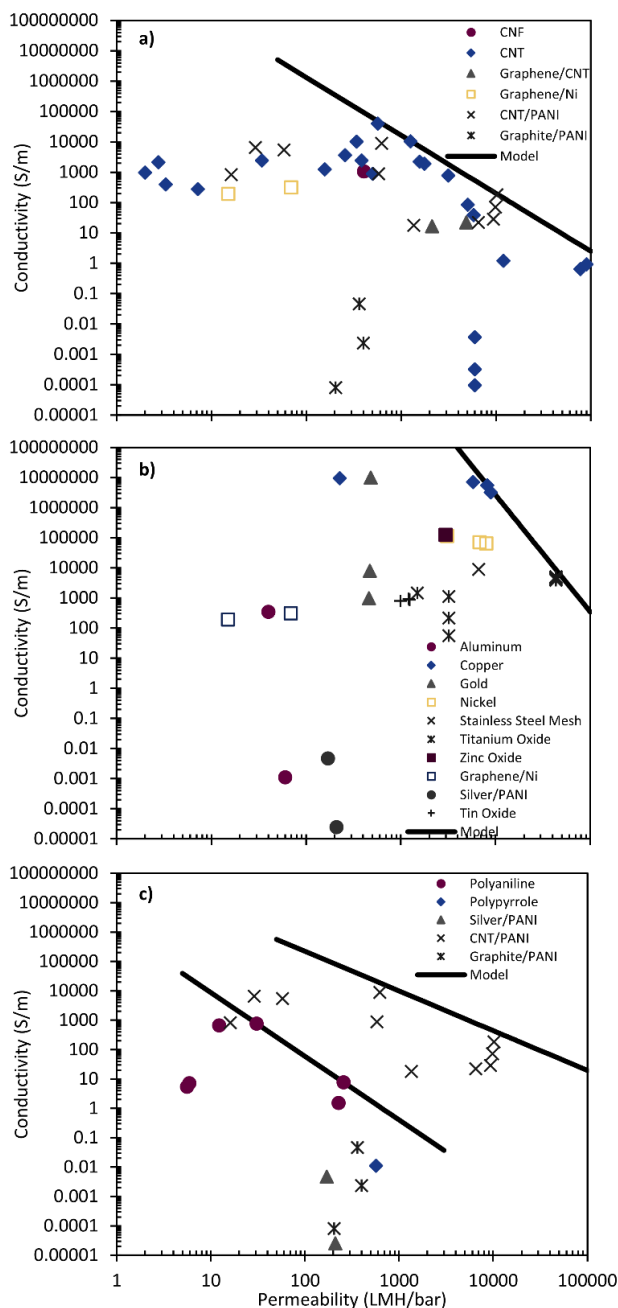


**Figure 3.1.** Series of Robeson-like plots comparing the conductivity and permeability values for 80 different electrically conductive membranes developed in 38 different published journal articles. Each panel represents a different class of conductive material used for developing the membrane: **a)** graphitic nanomaterials; **b)** metals; **c)** conductive polymers. Legend entries identify the exact conductive material used. Composite materials belonging to more than one class are shown in each applicable panel. The upper performance limit (black line) in each panel was established by fitting an exponential curve to select data and then adjusting the model parameters such that the residual values were negative for all the fitted data points: **a)**  $C = 8.79 \times 10^9 L_p^{-1.91}$ ; **b)**  $C = 9.07 \times 10^{21} L_p^{-3.88}$ ; **c)**  $C = 1.11 \times 10^8 L_p^{-1.35}$  and  $C = 1.29 \times 10^6 L_p^{-2.17}$  when composite materials were excluded.

### 3.5.2 *Assessing the Distribution of ECM Materials and Configurations*

In Fig. 3.1 there exists a wide variety of applications for which these membranes were developed. The 80 data points in Fig. 1 represent a variety of separation types (i.e. MF, UF, NF, RO, FO), and membrane configuration (i.e. flat sheet, hollow fiber, tubular). As such, comparisons of membrane selectivity across all data points should not be made. The distribution of these data points in terms of conductive material class, separation type, and membrane configuration are represented graphically in Fig. 2 as three separate rings. Each ring is broken into segments that are proportional in size to the number of data points from Fig. 3.1 that fit within the given category. For example, of all the 80 data points in Fig. 3.1, 42% of the membranes (34 data points) contained graphitic nanomaterials as at least one of the conductive materials. Of those graphitic nanomaterial- based ECMs, 50% (17 data points) were UF membranes and of those UF membranes, 95% (16 data points) were made in a flat sheet configuration. Composites that contained more than one type of conductive material were accounted for in each applicable class, such that those membranes which were composed of graphitic and polymer materials were double counted.

Metallic-based ECMs tended towards the highest permeability and conductivity values compared to polymeric and graphitic nanomaterial-based ECMs (see Fig. 3.1). The trend towards higher permeability can be partially explained by the separation type for which these metallic ECMs were designed. As shown in Fig. 3.2, MF separations account for ~68% of all metallic-based ECMs included in Fig. 3.1, with the rest made up by UF. In comparison, MF separations accounted for only ~39% of graphitic nanomaterial based ECMs and none of the conductive polymer based ECMs. Thus, the metallic-based ECMs naturally trended towards higher permeabilities as they were largely intended for high flux MF applications. Despite the high

porosity of MF membranes onto which the metals were deposited, the metallic-based ECMs were still able to achieve high conductivity, while maintaining the membrane's high permeability. This suggests that metallic-based NF membranes would also demonstrate high conductivities while experiencing limited changes to permeability. The impact on RO membranes is still as yet unexplored. This demonstrates an opportunity for researchers to investigate NF and RO metallic-based ECMs.

In terms of configuration, flat sheet membranes represented the overall majority with ~68% of all data points; however, this distribution was not proportionate between different classes of conductive materials. ECMs based on conductive polymers were only developed in the flat sheet format. Graphitic nanomaterial-based ECMs were formed primarily as flat sheet membranes, but ~22% of these membranes were formed as hollow fibers (HF). Metallic-based ECMs show the most diversity with ~34% HF, ~10% tubular and ~56% flat sheet. As might be expected, HF and tubular configurations were exclusively developed for MF and UF applications while none were developed for NF/RO/FO, as the pressure requirements for these applications can be challenging to meet in HF configurations.

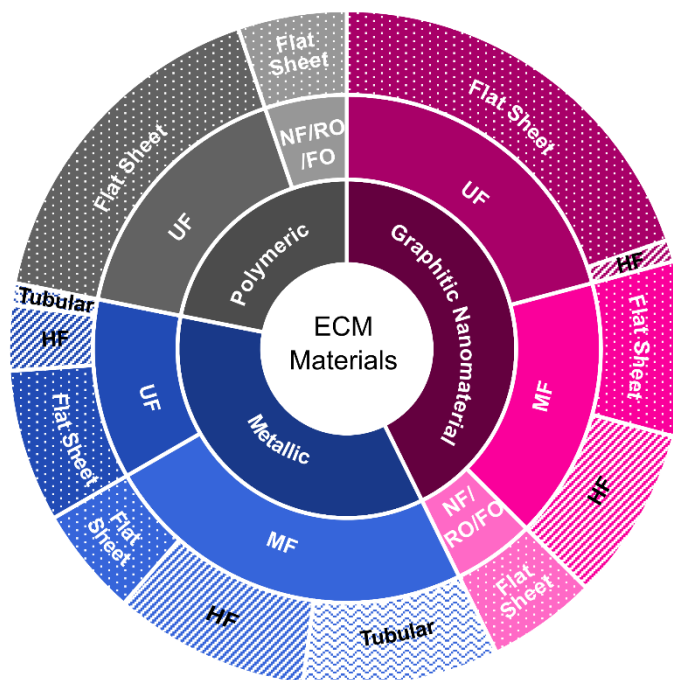


**Figure 3.2.** Distribution of the 80 data points in Figure 3.1. classified by conductive material used (inner ring), separation type (middle ring), and membrane configuration (outer ring). The arc length of each ring segment is proportional to the number of data points that fit in the category. Ring segments are coloured first according to conductive material (maroon for graphitic nanomaterials, blue for metallic and grey for polymeric), then by separation type (darkest shade for UF, middle shade for MF and lightest for NF/RO/FO), and are patterned according to membrane configuration (dotted for flat sheet, lined for hollow fiber and wave pattern for tubular).

### 3.5.3 Assessing the Distribution of ECM Applications

The electro-functional capabilities of ECMs have been used in a variety of applications with a primary focus on antifouling, enhanced separations, and electrochemical degradation of contaminants. This distribution in performance testing is illustrated in Fig. 3.3 where all 63 performance tests conducted across the 38 papers reviewed are summarized graphically in a similar method to Fig. 3.2. Tests were classified by general application (inner ring), specific test (middle ring), and target solute/ foulant/ pollutant (outer ring) where the arc length of the ring segment is proportional to the number of tests that fit in that category. Antifouling applications were subdivided into organic foulants, biological foulants, and scalants. Redox based degradation primarily occurred through oxidation with two studies comparing the effects of both oxidation and

reduction [9,11], and one focussed on reduction [25]. For enhanced separations, some research focused on the electrostatic effects to improve charged particle separation while pore-size tuning was unique to polyaniline (PANI) based ECMs, in which the charge and volumetric changes of PANI under an applied potential were used to alter rejection characteristics [32]. Some pollutants appeared twice depending on the nature of the performance test. For example, methyl blue was evaluated both as an organic foulant while monitoring flux decline [20] and as a contaminant subjected to oxidative degradation with concentration tracked over time [18]. Results from three papers were excluded from this figure as they focused on ECM development and did not conduct detailed performance tests [13,24,36].

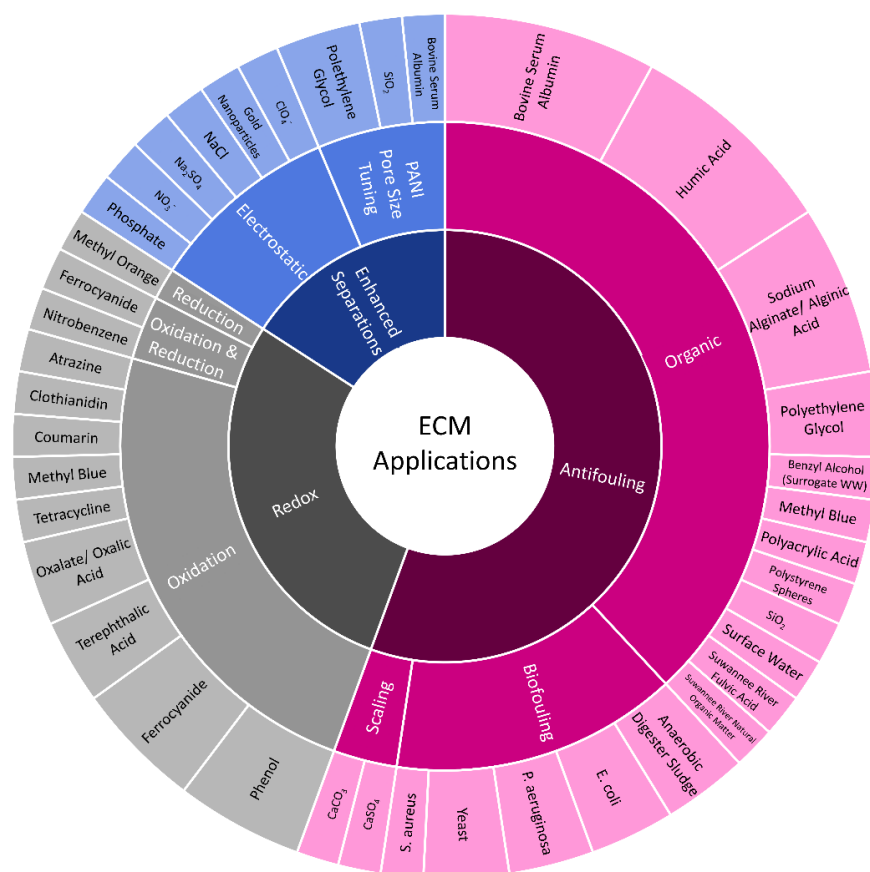


**Figure 3.3.** Distribution of the 63 conductive membrane performance tests conducted in the 38 papers reviewed classified by the general application (inner ring), specific test (middle ring), and specific pollutant (outer ring) used. The arc length of each ring segment is proportional to the number of tests that fit in the category. Ring segments are coloured according to the general application (maroon for antifouling, blue for enhanced separations and grey for redox).

The wide diversity in ECM applications is immediately apparent from the outer ring in Fig. 3.3, which indicates 35 unique performance tests were conducted. Antifouling applications represented the greatest proportion of tests (~56%), followed by redox reactions (~29%) and enhanced separations (~15%). The most diverse performance tests included organic fouling prevention by ECMs, in which the fouling impact of 12 different pollutants were investigated across 24 separate studies. Research on the oxidation of contaminants were similarly diverse, in which the oxidative reactions of 9 different pollutants were investigated across 15 separate studies. While this wide variety of studies indicates the many applications which ECMs can enhance, it also highlights the difficulty in conducting effective comparisons between ECMs formed in different research groups. This diversity indicates the need for a consistent metric to be able to confidently compare performance between different types of ECMs. We encourage research into exploring more applications for ECMs, and we also recommend a set of standard molecules for certain separations to properly compare different ECMs against each other. Not all separations necessitate standards, however the standards would benefit the evaluation of ECM potential towards preventing organic fouling and biofouling, and their ability to engage in redox reactions. This list of proposed standard pollutants is found in Table 1, selected for their relative safe handling, ease of monitoring, and ready availability in standardized formats [4,19,25]. Measurements of permeability (LMH/bar), resistivity ( $\Omega\text{m}$ ), sheet resistance ( $\Omega/\text{sq}$ ) and active layer thickness ( $\mu\text{m}$ ) should also be standardized to assess membrane throughput and electrochemical functionality. Further, assessment of Fig. 3.3 shows that most of the performance tests using ECMs were conducted with controlled simple lab solutions. Only three studies used realistic solutions including surface water and anaerobic digester sludge [15,26,28]. As the field

of ECMs continues to grow and mature, there is a need for testing with more realistic feed sources to evaluate performance in real wastewater/ water scenarios.

To relate the conductivity/ permeability trade-off to specific applications, we have included a modified version of the Robeson-like plots in Fig. 3.S1 with the legend entries identifies specific applications (corresponding to the middle ring in Fig. 3.3) for the graphitic nanomaterial, metallic, and conductive polymer based ECMs, as opposed to the type of materials used in those applications.

ECMs for some applications have been developed with a wide range of properties. For example, ECMs synthesized to prevent biofouling have been made with conductivities that span a 12-order of magnitude range and permeabilities that span a 4-order of magnitude range. ECMs used for other applications have properties synthesized with much narrower ranges. ECMs synthesized to oxidize contaminants have been made with conductivities from  $\sim 10$ - $10,000$  S/m and permeabilities from  $\sim 300$ - $4,000$  LMH/bar, and PANI pore size tuning with conductivities  $\sim 5$ - $200$  S/m, all properties within a 3-order or less magnitude range. The consistency identified for these two applications may be due to material limitations, such as the inherently lower conductivity of PANI over other conductive materials [46], or the minimum metal thickness required to overcome the percolation threshold. This may also indicate that ECMs formed for these applications these applications have been optimized in terms of their conductivities necessary for their application, however the small number of papers in these areas suggests that these ECMs have not yet been optimized.

**Table 3.1.** Recommended standard tests/ pollutants for evaluating common ECM applications.

Application	Biofouling	Organic Fouling	Oxidation/ Reduction
<b>Standard Test</b>			
Pollutant Filtration	<i>E. coli</i>	Bovine serum albumin (BSA)	Methyl orange dye
Permeability	Pure water permeability (LMH/bar)		
Surface Conductivity/ Electrochemical Properties	Resistivity ( $\Omega\text{m}$ ) & Sheet Resistance ( $\Omega/\text{sq}$ )		
	Active Layer Thickness ( $\mu\text{m}$ )		

### 3.6 Conclusions

The “Robeson-like” plots developed herein clearly illustrate the trade-off in electrically conductive membrane (ECM) surface conductivity and hydraulic permeability and provide a simple method for comparing ECM performance across various fabrication parameters. Literature data was collected and analyzed for ECMs developed using a variety of conductive materials (i.e. graphitic nanomaterials, metals, and conductive polymers) and for a variety of separation types (i.e. MF, UF, NF/RO/FO), configurations (i.e. flat sheet, hollow fiber, tubular), and applications (i.e. antifouling, enhanced separations, redox). Upper limit models were developed to quantify the conductivity/ permeability trade-off for each of the three major classes of conductive materials. With respect to electrical conductivity, metallic-based ECMs out-performed ECMs made from graphitic nanomaterials and conductive polymers with maximum conductivities over three orders of magnitude greater. Maximum achievable permeabilities were more comparable across the three classes of conductive materials. Although metallic ECMs demonstrated higher overall permeabilities, they were largely designed for high flux MF applications (~68% of data for metallic-based ECMs) which is a significant contributing factor to their observed performance. A large diversity was evident in the 63 performance tests conducted across the 38 papers reviewed and revealed several limitations for proper comparison in the field: 1) a lack of standard pollutants against which each membrane can be compared for their specific application, and 2) limited testing using realistic water sources. The lack of standards for ECM performance makes it difficult to

compare performance between ECMs, while limited testing under realistic conditions is necessary to demonstrate ECM's real-world applicability. Moreover, of the 93 relevant papers in the field, only 38 papers provided both permeability and conductivity (or conductance and thin film thickness) data. It is critical to report these data so that proper comparisons can be made across all ECMs. Our conductivity/ permeability trade-off plots create a standardized method for evaluating ECM performance and utility. These plots would be useful for identifying specific requirements for an ECM application, or to identify materials and fabrication methods that lead to optimal ECMs.

### 3.7 References

- [1] G. Wei, S. Chen, X. Fan, X. Quan, H. Yu, Carbon nanotube hollow fiber membranes: High-throughput fabrication, structural control and electrochemically improved selectivity, *J. Memb. Sci.* 493 (2015) 97–105. <https://doi.org/10.1016/j.memsci.2015.05.073>.
- [2] R. Liu, Y. Sui, X. Wang, Metal–organic framework-based ultrafiltration membrane separation with capacitive-type for enhanced phosphate removal, *Chem. Eng. J.* 371 (2019) 903–913. <https://doi.org/10.1016/j.cej.2019.04.136>.
- [3] C.F. De Lannoy, D. Jassby, K. Gloe, A.D. Gordon, M.R. Wiesner, Aquatic biofouling prevention by electrically charged nanocomposite polymer thin film membranes, *Environ. Sci. Technol.* (2013) 1304–1319.
- [4] A. Ronen, W. Duan, I. Wheeldon, S. Walker, D. Jassby, Microbial Attachment Inhibition through Low-Voltage Electrochemical Reactions on Electrically Conducting Membranes, *Environ. Sci. Technol.* 49 (2015) 12741–12750. <https://doi.org/10.1021/acs.est.5b01281>.
- [5] Q. Zhang, C.D. Vecitis, Conductive CNT-PVDF membrane for capacitive organic fouling reduction, *J. Memb. Sci.* 459 (2014) 143–156. <https://doi.org/10.1016/j.memsci.2014.02.017>.
- [6] A. V. Dudchenko, J. Rolf, K. Russell, W. Duan, D. Jassby, Organic fouling inhibition on electrically conducting carbon nanotube-polyvinyl alcohol composite ultrafiltration membranes, *J. Memb. Sci.* 468 (2014) 1–10. <https://doi.org/10.1016/j.memsci.2014.05.041>.
- [7] W. Duan, A. Dudchenko, E. Mende, C. Flyer, X. Zhu, D. Jassby, Electrochemical mineral scale prevention and removal on electrically conducting carbon nanotube-polyamide reverse osmosis membranes, *Environ. Sci. Process. Impacts.* 16 (2014) 1300–1308. <https://doi.org/10.1039/c3em00635b>.
- [8] J. Li, Q. Liu, Y. Liu, J. Xie, Development of electro-active forward osmosis membranes to remove phenolic compounds and reject salts, *Environ. Sci. Water Res. Technol.* 3 (2017)

- 139–146. <https://doi.org/10.1039/c6ew00275g>.
- [9] M.C. Santos, Y.A. Elabd, Y. Jing, B.P. Chaplin, L. Fang, Highly Porous Ti<sub>4</sub>O<sub>7</sub> Reactive Electrochemical Water Filtration Membranes Fabricated via Electrospinning/Electrospraying, *AIChE J.* 62 (2015) 508–524. <https://doi.org/10.1002/aic>.
- [10] Y. Liu, J.H. Dustin Lee, Q. Xia, Y. Ma, Y. Yu, L.Y. Lanry Yung, J. Xie, C.N. Ong, C.D. Vecitis, Z. Zhou, A graphene-based electrochemical filter for water purification, *J. Mater. Chem. A* 2 (2014) 16554–16562. <https://doi.org/10.1039/c4ta04006f>.
- [11] G. Gao, Q. Zhang, C.D. Vecitis, CNT-PVDF composite flow-through electrode for single-pass sequential reduction-oxidation, *J. Mater. Chem. A* 2 (2014) 6185–6190. <https://doi.org/10.1039/c3ta14080f>.
- [12] D. Bell, R. Sengpiel, M. Wessling, Metallized hollow fiber membranes for electrochemical fouling control, *J. Memb. Sci.* 594 (2020) 117397. <https://doi.org/10.1016/j.memsci.2019.117397>.
- [13] C.F. de Lannoy, D. Jassby, D.D. Davis, M.R. Wiesner, A highly electrically conductive polymer-multiwalled carbon nanotube nanocomposite membrane, *J. Memb. Sci.* 415–416 (2012) 718–724. <https://doi.org/10.1016/j.memsci.2012.05.061>.
- [14] S. Wang, S. Liang, P. Liang, X. Zhang, J. Sun, S. Wu, X. Huang, In-situ combined dual-layer CNT/PVDF membrane for electrically-enhanced fouling resistance, *J. Memb. Sci.* 491 (2015) 37–44. <https://doi.org/10.1016/j.memsci.2015.05.014>.
- [15] L. Du, X. Quan, X. Fan, G. Wei, S. Chen, Conductive CNT/nanofiber composite hollow fiber membranes with electrospun support layer for water purification, *J. Memb. Sci.* 596 (2020) 117613. <https://doi.org/10.1016/j.memsci.2019.117613>.
- [16] X. Fan, H. Zhao, X. Quan, Y. Liu, S. Chen, Nanocarbon-based membrane filtration integrated with electric field driving for effective membrane fouling mitigation, *Water Res.* 88 (2016) 285–292. <https://doi.org/10.1016/j.watres.2015.10.043>.
- [17] C.F. de Lannoy, D. Jassby, K. Gloe, A.D. Gordon, M.R. Wiesner, Aquatic biofouling prevention by electrically charged nanocomposite polymer thin film membranes, *Environ. Sci. Technol.* 47 (2013) 2760–2768. <https://doi.org/10.1021/es3045168>.
- [18] W. Duan, A. Ronen, J.V. de Leon, A. Dudchenko, S. Yao, J. Corbala-Delgado, A. Yan, M. Matsumoto, D. Jassby, Treating anaerobic sequencing batch reactor effluent with electrically conducting ultrafiltration and nanofiltration membranes for fouling control, *J. Memb. Sci.* 504 (2016) 104–112. <https://doi.org/10.1016/j.memsci.2016.01.011>.
- [19] W. Duan, A. Ronen, S. Walker, D. Jassby, Polyaniline-Coated Carbon Nanotube Ultrafiltration Membranes: Enhanced Anodic Stability for in Situ Cleaning and Electro-Oxidation Processes, *ACS Appl. Mater. Interfaces.* 8 (2016) 22574–22584. <https://doi.org/10.1021/acsami.6b07196>.
- [20] G. Wei, J. Dong, J. Bai, Y. Zhao, Y. Li, Structurally Stable, Antifouling, and Easily Renewable Reduced Graphene Oxide Membrane with a Carbon Nanotube Protective Layer, *Environ. Sci. Technol.* 53 (2019) 11896–11903. <https://doi.org/10.1021/acs.est.9b03129>.

- [21] H. Zhang, X. Quan, X. Fan, G. Yi, S. Chen, H. Yu, Y. Chen, Improving Ion Rejection of Conductive Nanofiltration Membrane through Electrically Enhanced Surface Charge Density, *Environ. Sci. Technol.* 53 (2019) 868–877. <https://doi.org/10.1021/acs.est.8b04268>.
- [22] M.H. Schnoor, C.D. Vecitis, Quantitative examination of aqueous ferrocyanide oxidation in a carbon nanotube electrochemical filter: Effects of flow rate, ionic strength, and cathode material, *J. Phys. Chem. C* 117 (2013) 2855–2867. <https://doi.org/10.1021/jp3112099>.
- [23] Y. Liao, D.G. Yu, X. Wang, W. Chain, X.G. Li, E.M.V. Hoek, R.B. Kaner, Carbon nanotube-templated polyaniline nanofibers: Synthesis, flash welding and ultrafiltration membranes, *Nanoscale* 5 (2013) 3856–3862. <https://doi.org/10.1039/c3nr00441d>.
- [24] C. Otto, U.A. Handge, P. Georgopoulos, O. Aschenbrenner, J. Kerwitz, C. Abetz, A.L. Metze, V. Abetz, Porous UHMWPE Membranes and Composites Filled with Carbon Nanotubes: Permeability, Mechanical, and Electrical Properties, *Macromol. Mater. Eng.* 302 (2017) 1–14. <https://doi.org/10.1002/mame.201600405>.
- [25] A.J. Sutherland, M.X. Ruiz-Caldas, C.F. de Lannoy, Electro-catalytic microfiltration membranes electrochemically degrade azo dyes in solution, *J. Memb. Sci.* 611 (2020) 118335. <https://doi.org/10.1016/j.memsci.2020.118335>.
- [26] C.M. Werner, K.P. Katuri, A.R. Hari, W. Chen, Z. Lai, B.E. Logan, G.L. Amy, P.E. Saikaly, Graphene-Coated Hollow Fiber Membrane as the Cathode in Anaerobic Electrochemical Membrane Bioreactors - Effect of Configuration and Applied Voltage on Performance and Membrane Fouling, *Environ. Sci. Technol.* 50 (2016) 4439–4447. <https://doi.org/10.1021/acs.est.5b02833>.
- [27] L.L. Xu, Y. Xu, L. Liu, K.P. Wang, D.A. Patterson, J. Wang, Electrically responsive ultrafiltration polyaniline membrane to solve fouling under applied potential, *J. Memb. Sci.* 572 (2019) 442–452. <https://doi.org/10.1016/j.memsci.2018.11.026>.
- [28] D. Liu, X. Chen, B. Bian, Z. Lai, Y. Situ, Dual-Function Conductive Copper Hollow Fibers for Microfiltration and Anti-biofouling in Electrochemical Membrane Bioreactors, *Front. Chem.* 6 (2018) 1–10. <https://doi.org/10.3389/fchem.2018.00445>.
- [29] Y. Jing, L. Guo, B.P. Chaplin, Electrochemical impedance spectroscopy study of membrane fouling and electrochemical regeneration at a sub-stoichiometric TiO<sub>2</sub> reactive electrochemical membrane, *J. Memb. Sci.* 510 (2016) 510–523. <https://doi.org/10.1016/j.memsci.2016.03.029>.
- [30] W. Yang, M. Son, R. Rossi, J.S. Vrouwenvelder, B.E. Logan, Adapting Aluminum-Doped Zinc Oxide for Electrically Conductive Membranes Fabricated by Atomic Layer Deposition, *ACS Appl. Mater. Interfaces* 12 (2020) 963–969. <https://doi.org/10.1021/acsami.9b20385>.
- [31] J. Liu, C. Tian, J. Xiong, B. Gao, S. Dong, L. Wang, Polypyrrole vapor phase polymerization on PVDF membrane surface for conductive membrane preparation and fouling mitigation, *J. Chem. Technol. Biotechnol.* 93 (2018) 683–689. <https://doi.org/10.1002/jctb.5416>.

- [32] R. Rohani, I.I. Yusoff, Towards electrically tunable nanofiltration membranes: polyaniline-coated polyvinylidene fluoride membranes with tunable permeation properties, *Iran. Polym. J. (English Ed.)* 28 (2019) 789–800. <https://doi.org/10.1007/s13726-019-00744-0>.
- [33] L. Xu, S. Shahid, A.K. Holda, E.A.C. Emanuelsson, D.A. Patterson, Stimuli responsive conductive polyaniline membrane: In-filtration electrical tuneability of flux and MWCO, *J. Memb. Sci.* 552 (2018) 153–166. <https://doi.org/10.1016/j.memsci.2018.01.070>.
- [34] Y. Zhou, S. Maharubin, P. Tran, T. Reid, G.Z. Tan, Anti-biofilm AgNP-polyaniline-polysulfone composite membrane activated by low intensity direct/alternating current, *Environ. Sci. Water Res. Technol.* 4 (2018) 1511–1521. <https://doi.org/10.1039/c8ew00259b>.
- [35] T. Mantel, P. Benne, S. Parsin, M. Ernst, Electro-conductive composite gold-polyethersulfone-ultrafiltration-membrane: Characterization of membrane and natural organic matter (NOM) filtration performance at different in-situ applied surface potentials, *Membranes (Basel)*. 8 (2018). <https://doi.org/10.3390/membranes8030064>.
- [36] M.J. Larocque, D.R. Latulippe, C.F. de Lannoy, Formation of electrically conductive hollow fiber membranes via crossflow deposition of carbon nanotubes – addressing the conductivity/permeability trade-off, *J. Memb. Sci.* (2020). <https://doi.org/10.1016/j.memsci.2020.118859>.
- [37] J. Huang, Z. Wang, J. Zhang, X. Zhang, J. Ma, Z. Wu, A novel composite conductive microfiltration membrane and its anti-fouling performance with an external electric field in membrane bioreactors, *Sci. Rep.* 5 (2015) 1–9. <https://doi.org/10.1038/srep09268>.
- [38] L.M. Robeson, Correlation of separation factor versus permeability for polymeric membranes, *J. Memb. Sci.* 62 (1991) 165–185. [https://doi.org/10.1016/0376-7388\(91\)80060-J](https://doi.org/10.1016/0376-7388(91)80060-J).
- [39] A. Mehta, A.L. Zydney, Permeability and selectivity analysis for ultrafiltration membranes, *J. Memb. Sci.* 249 (2005) 245–249. <https://doi.org/10.1016/j.memsci.2004.09.040>.
- [40] G.M. Geise, H.B. Park, A.C. Sagle, B.D. Freeman, J.E. McGrath, Water permeability and water/salt selectivity tradeoff in polymers for desalination, *J. Memb. Sci.* 369 (2011) 130–138. <https://doi.org/10.1016/j.memsci.2010.11.054>.
- [41] C. Buelke, A. Alshami, J. Casler, Y. Lin, M. Hickner, I.H. Aljundi, Evaluating graphene oxide and holey graphene oxide membrane performance for water purification, *J. Memb. Sci.* 588 (2019) 117195. <https://doi.org/10.1016/j.memsci.2019.117195>.
- [42] L. Guo, Y. Jing, B.P. Chaplin, Development and Characterization of Ultrafiltration TiO<sub>2</sub> Magnéli Phase Reactive Electrochemical Membranes, *Environ. Sci. Technol.* 50 (2016) 1428–1436. <https://doi.org/10.1021/acs.est.5b04366>.
- [43] P. Gayen, C. Chen, J.T. Abiade, B.P. Chaplin, Electrochemical Oxidation of Atrazine and Clothianidin on Bi-doped SnO<sub>2</sub>-Ti<sub>n</sub>O<sub>2n-1</sub> Electrocatalytic Reactive Electrochemical Membranes, *Environ. Sci. Technol.* 52 (2018) 12675–12684. <https://doi.org/10.1021/acs.est.8b04103>.
- [44] J. Chen, W. Chen, D. Zhu, Adsorption of nonionic aromatic compounds to single-walled

carbon nanotubes: Effects of aqueous solution chemistry, *Environ. Sci. Technol.* 42 (2008) 7225–7230. <https://doi.org/10.1021/es801412j>.

[45] S. Kang, M. Herzberg, D.F. Rodrigues, M. Elimelech, Antibacterial effects of carbon nanotubes: Size does matter!, *Langmuir*. 24 (2008) 6409–6413. <https://doi.org/10.1021/la800951v>.

[46] I.H. Loh, R.A. Moody, J.C. Huang, Electrically conductive membranes: Synthesis and applications, *J. Memb. Sci.* 50 (1990) 31–49. [https://doi.org/10.1016/S0376-7388\(00\)80884-4](https://doi.org/10.1016/S0376-7388(00)80884-4).

### 3.8 Supplementary Information

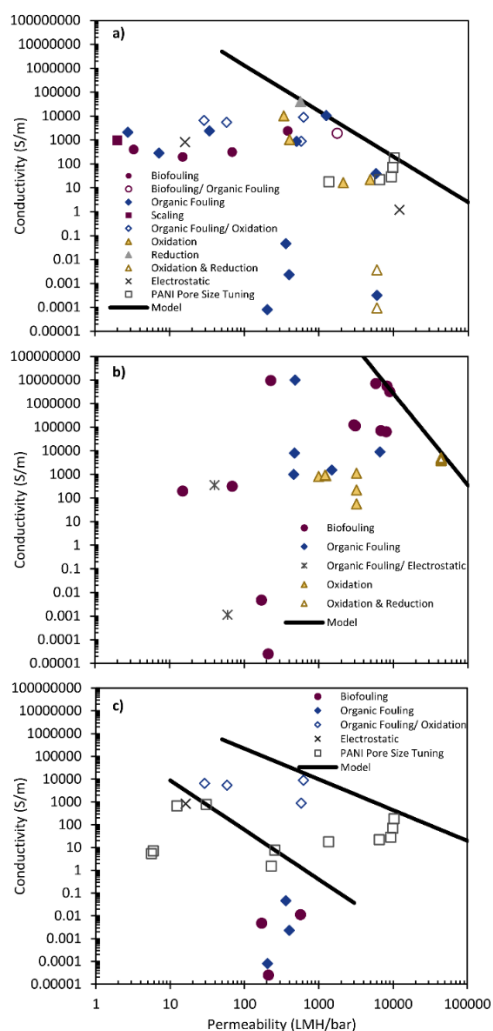


**Figure 3.S1.** Series of Robeson-like plots representing the same conductivity/ permeability data from Fig. 3.1 with the specific applications each membrane was design for identified in the legend entries. Panels correspond to **a)** graphitic nanomaterials; **b)** metals; **c)** conductive polymers. Composite materials belonging to more than one class are shown in each applicable panel. The same upper performance limits (black line) are included from Fig. 3.1.

**Table 3.S1.** Literature values for conductive membrane hydraulic permeability and surface conductivity used to develop the upper limit line for graphitic nanomaterials in the Robeson-like plot (Fig. 3.1a). Conductivities predicted using the upper limit equation  $C = 8.79 \times 10^9 \cdot L_p^{-1.91}$  are included below along with their corresponding residuals.

Reference	Permeability (LHM/bar)	Conductivity (S/m)	Predicted Conductivity (S/m)	Residuals (S/m)
[1]	1260.00	10490.00	10509.88	-19.88
[2]	1760.00	1900.00	5550.63	-3650.63
[3]	6529.07	22.22	453.70	-431.48
[3]	9362.44	28.57	227.90	-199.33
[3]	9855.20	71.43	206.63	-135.20
[3]	10224.77	181.82	192.60	-10.78
[4]	5800.00	39.00	568.86	-529.86
[5]	90000.00	0.93	3.02	-2.09
[5]	77500.00	0.64	4.02	-3.38
[6]	5034.71	84.95	745.41	-660.46
[6]	1571.42	2204.61	6892.30	-4687.68
[6]	3143.49	769.89	1832.97	-1063.08
[7]	565.70	40098.00	48523.00	-8425.00

**Table 3.S2.** Literature values for conductive membrane hydraulic permeability and surface conductivity used to develop the upper limit line for metals in the Robeson-like plot (Fig. 3.1b). Conductivities predicted using the upper limit equation  $C = 9.07 \times 10^{21} \cdot L_p^{-3.88}$  are included below along with their corresponding residuals.

Reference	Permeability (LHM/bar)	Conductivity (S/m)	Predicted Conductivity (S/m)	Residuals (S/m)
[8]	8913.00	3227888.96	4132592.31	-904703.35
[8]	8200.00	5555555.56	5712923.37	-157367.82
[8]	5812.00	7142857.14	21749745.23	-14606888.08
[9]	43571.43	4725.00	8700.26	-3975.26
[9]	43571.43	4567.00	8700.26	-4133.26
[9]	43571.43	4135.00	8700.26	-4565.26
[9]	43571.43	3838.00	8700.26	-4862.26
[9]	43571.43	4695.00	8700.26	-4005.26
[9]	43571.43	5071.00	8700.26	-3629.26
[9]	43571.43	4612.00	8700.26	-4088.26
[9]	43571.43	4235.00	8700.26	-4465.26
[9]	43571.43	4218.00	8700.26	-4482.26
[10]	2973.27	124378.11	293777780.77	-293653402.66

**Table 3.S3.** Literature values for conductive membrane hydraulic permeability and surface conductivity used to develop the upper limit line for conductive polymers in the Robeson-like plot (Fig. 3.1c). Conductivities predicted using the upper limit equation  $C = 1.11 \times 10^8 \cdot L_p^{-1.35}$  are included below along with their corresponding residuals.

Reference	Permeability (LHM/bar)	Conductivity (S/m)	Predicted Conductivity (S/m)	Residuals (S/m)
[11]	623.66	8928.00	18633.41	-9705.41
[3]	10224.77	181.82	427.01	-245.20
[3]	9362.44	28.57	480.95	-452.38
[11]	580.15	883.00	20544.41	-19661.41

**Table 3.S4.** Literature values for conductive membrane hydraulic permeability and surface conductivity used to develop the upper limit line for conductive polymers excluding composite materials in the Robeson-like plot (Fig. 3.1c). Conductivities predicted using the upper limit equation  $C = 1.29 \times 10^6 \cdot L_p^{-2.17}$  are included below along with their corresponding residuals.

Reference	Permeability (LHM/bar)	Conductivity (S/m)	Predicted Conductivity (S/m)	Residuals (S/m)
[12]	30.60	770.50	770.50	0.00
[12]	257.00	7.61	7.61	0.00

### References

- [1] S. Wang, S. Liang, P. Liang, X. Zhang, J. Sun, S. Wu, X. Huang, In-situ combined dual-layer CNT/PVDF membrane for electrically-enhanced fouling resistance, *J. Memb. Sci.* 491 (2015) 37–44. <https://doi.org/10.1016/j.memsci.2015.05.014>.
- [2] X. Fan, H. Zhao, X. Quan, Y. Liu, S. Chen, Nanocarbon-based membrane filtration integrated with electric field driving for effective membrane fouling mitigation, *Water Res.* 88 (2016) 285–292. <https://doi.org/10.1016/j.watres.2015.10.043>.
- [3] Y. Liao, D.G. Yu, X. Wang, W. Chain, X.G. Li, E.M.V. Hoek, R.B. Kaner, Carbon nanotube-templated polyaniline nanofibers: Synthesis, flash welding and ultrafiltration membranes, *Nanoscale.* 5 (2013) 3856–3862. <https://doi.org/10.1039/c3nr00441d>.
- [4] L. Du, X. Quan, X. Fan, G. Wei, S. Chen, Conductive CNT/nanofiber composite hollow fiber membranes with electrospun support layer for water purification, *J. Memb. Sci.* 596 (2020) 117613. <https://doi.org/10.1016/j.memsci.2019.117613>.
- [5] C. Otto, U.A. Handge, P. Georgopoulos, O. Aschenbrenner, J. Kerwitz, C. Abetz, A.L. Metze, V. Abetz, Porous UHMWPE Membranes and Composites Filled with Carbon Nanotubes: Permeability, Mechanical, and Electrical Properties, *Macromol. Mater. Eng.* 302 (2017) 1–14. <https://doi.org/10.1002/mame.201600405>.
- [6] M.J. Larocque, D.R. Latulippe, C.F. de Lannoy, Formation of electrically conductive hollow fiber membranes via crossflow deposition of carbon nanotubes – addressing the conductivity/permeability trade-off, 2020.
- [7] A.J. Sutherland, M.X. Ruiz-Caldas, C.F. de Lannoy, Electro-catalytic microfiltration membranes electrochemically degrade azo dyes in solution, *J. Memb. Sci.* 611 (2020) 118335. <https://doi.org/10.1016/j.memsci.2020.118335>.
- [8] D. Liu, X. Chen, B. Bian, Z. Lai, Y. Situ, Dual-Function Conductive Copper Hollow Fibers for Microfiltration and Anti-biofouling in Electrochemical Membrane Bioreactors, *Front. Chem.* 6 (2018) 1–10. <https://doi.org/10.3389/fchem.2018.00445>.
- [9] M.C. Santos, Y.A. Elabd, Y. Jing, B.P. Chaplin, L. Fang, Highly Porous Ti4O7 Reactive Electrochemical Water Filtration Membranes Fabricated via Electrospinning/Electrospraying, *AIChE J.* 62 (2015) 508–524. <https://doi.org/10.1002/aic>.

[10] W. Yang, M. Son, R. Rossi, J.S. Vrouwenvelder, B.E. Logan, Adapting Aluminum-Doped Zinc Oxide for Electrically Conductive Membranes Fabricated by Atomic Layer Deposition, *ACS Appl. Mater. Interfaces*. 12 (2020) 963–969. <https://doi.org/10.1021/acsami.9b20385>.

[11] W. Duan, A. Ronen, S. Walker, D. Jassby, Polyaniline-Coated Carbon Nanotube Ultrafiltration Membranes: Enhanced Anodic Stability for in Situ Cleaning and Electro-Oxidation Processes, *ACS Appl. Mater. Interfaces*. 8 (2016) 22574–22584. <https://doi.org/10.1021/acsami.6b07196>.

[12] R. Rohani, I.I. Yusoff, Towards electrically tunable nanofiltration membranes: polyaniline-coated polyvinylidene fluoride membranes with tunable permeation properties, *Iran. Polym. J. (English Ed.)* 28 (2019) 789–800. <https://doi.org/10.1007/s13726-019-00744-0>.

## **Chapter 4: Evaluating conductive hollow fiber membrane performance in redox and adsorptive removal of methyl orange**

### **4.1 Abstract**

Efficient, industrial-scale processes are needed to treat textile industry effluents with toxic azo dyes. Electrically conductive membranes (ECMs) have demonstrated successful (>98%) removal of surrogate azo dyes in previous works; however, these have all been limited to the flat sheet membrane format. Hollow fiber format is preferred for large industrial applications due to its high packing density. In our previous work, we demonstrated a “crossflow deposition” approach for fabricating inside-out carbon nanotube (CNT)-based conductive hollow fiber membranes as a method for balancing surface conductivity and hydraulic permeability. The goal of this work was to evaluate the effectiveness these CNT-coated hollow fiber membranes in the removal of methyl orange as a surrogate azo dye. The adsorptive removal capacity of the CNTs used in this fabrication method were evaluated in a batch suspension experiment and while equilibrium methyl orange concentration stabilized quickly (~30 min), error between duplicate experiments made it difficult to fit an adsorption isotherm model. Electrochemical removal was assessed in a batch and continuous filtration configuration. Up to 40% MO removal was achieved with a stainless steel needle as a working electrode in a 500 mL batch, but no removal was detected with the CNT-coated HF membranes. Similarly, in the continuous removal experiments, no MO removal was detected after 6 h of recycled operation. Further optimization of the experimental system is required to determine the necessary combination of parameters for continuous MO removal, including counter electrode material, electrode spacing, surface conductivity, and contact time.

## 4.2 Introduction

Membrane separations have become increasingly prevalent in wastewater treatment; however, there are several limitations inhibiting their further widespread use including susceptibility to fouling and an inability to degrade contaminants. Microfiltration (MF) and ultrafiltration (UF) membranes are common in tertiary treatment processes for removing bacteria and large particles by size exclusion but are incapable of removing small organic contaminants that can have detrimental health and environmental effects. Azo dyes, for example, are widespread contaminants in textile process effluents and are a significant concern due to their known toxicity and carcinogenic potential [1]. Dense membranes such as nanofiltration (NF) and reverse osmosis (RO) can effectively reject these small organic molecules [2,3] but can be costly for large scale implementation due to their high pressure requirements and low flux [4]. In addition, pre-treatment unit operations are often required before NF/RO processes to prevent damage to the membrane surface from particulates or chemicals (e.g. chlorinated disinfectants or oxidants) in the feed [3–5]. Conventional processes for azo dye removal include advanced oxidation and adsorption; however, these methods incur large operating costs for consumption of strong oxidizing agents and adsorbent regeneration, respectively [6,7]. Electrochemical cells offer an economical alternative to advanced oxidation processes by generating oxidizing agents, or directly oxidizing contaminants to achieve degradation [7]. Electrically conductive membranes (ECMs) combine this electrochemical approach with MF/UF membrane filtration in a process intensification effort.

ECMs are an emerging strategy for addressing several of these concerns by combining membrane filtration and electrochemical mechanisms for removal. The application of a potential on a conductive membrane surface has been shown to induce electrostatic repulsion [8], reactive oxygen species generation (e.g. hydroxyl radicals) [9], and electrochemical redox reactions [10]

in the feed water. These mechanisms have been exploited in membrane processes to mitigate fouling (biofouling [11,12], organic fouling [12,13], scaling [14]) and degrade model contaminants such as dyes (e.g. methyl orange (MO) [12,15,16], methyl blue [15]), and organic compounds (e.g. phenol, oxalate, tetracycline [10]) that cannot be rejected by traditional MF/UF membranes. ECM fabrication methods are widely varied but typically consist of a conductive material in combination with a support membrane. Conductive materials include graphitic nanomaterials (e.g. CNTs [9,11–17], graphene [10]), metals (e.g. titanium oxide [18], copper [19]) or conductive polymers (e.g. polypyrrole [20], polyaniline [21]).

Graphitic nanomaterials are of particular interest for contaminant degradation applications as these materials exhibit both adsorptive and electrochemical removal effects. In suspension, carbon nanotubes (CNTs) have shown high adsorption capacities for model azo dye contaminants, with up to ~60 mg/g for methyl orange (MO) [22–24]. Similar adsorptive capacities have been observed for CNT-based ECMs, around 30 mg/g for MO [15]. In addition to the adsorptive effect, under an applied potential electrochemical degradation has achieved up to 98% removal of MO [12,15,16]. MO is a useful surrogate compound for azo dye removal as it contains the characteristic azo ( $N \equiv N$ ) bond and can be monitored using a simple spectroscopy measurement.

A major limitation in ECM development has been its near exclusive focus on flat sheet membranes. Other membrane formats, such as hollow fiber (HF), are preferred in many industrial applications due to their high packing density which can maximize throughput [25]. Fabrication methods for conductive HF membranes are emerging in literature and these membranes have been successfully demonstrated in antifouling applications (e.g. biofouling [26], organic fouling [27]), charged particle rejection [17], and electrochemical contaminant degradation (e.g. ferrocyanide [18]).

In our previous work, we developed a crossflow deposition method for fabricating CNT-based conductive HF membranes and demonstrated the advantages of this technique in balancing the trade-off between surface conductivity and composite membrane hydraulic permeability [28]. The goal of this work was to evaluate the capability of these CNT-coated HF membranes for electrochemical degradation. To accomplish this, we selected methyl orange (MO) as a model azo dye due to the previous success of similar CNT-based membrane materials in flat sheet format [12,15,16]. We aim to quantify MO removal efficiency with the CNT-coated HF membranes in terms of both adsorptive and electrochemical removal mechanisms.

## 4.3 Experimental

### 4.3.1 Materials

Polyether sulfone (PES) MF membranes with a nominal pore size of 0.2  $\mu\text{m}$  were purchased from Repligen; the inner and outer diameters were measured to be 1.0 and 1.1 mm respectively via scanning electron microscopy (SEM) [28]. Carboxyl functionalized single walled/double walled carbon nanotubes (SW/DWCNTs) were purchased from Cheap Tubes; the properties reported by the manufacturer include outer diameter of 1–4 nm, length of 5–30  $\mu\text{m}$ , purity greater than 90% (by weight), functional content of 2.73% (by weight), and ash content less than 1.5% (by weight). Sodium dodecyl sulfate (SDS, MW: 288.38 Da) was purchased from Anachemia. Polyvinyl alcohol (PVA, MW: 13–23 kDa, 98-99% hydrolyzed) and methyl orange powder (MO, MW: 327.33 Da, dye content 85%) were purchased from Sigma Aldrich. The following chemicals were purchased at >98% purity: sodium phosphate dibasic, heptahydrate and sodium phosphate monobasic, monohydrate from Fisher Scientific and sodium chloride from Sigma Aldrich.

#### 4.3.2 Adsorption Kinetics & Isotherms

Batch experiments were performed with CNT suspensions to study the MO adsorptive capacity of the SW/DWCNTs used in the fabrication of the CNT-coated HF membranes. All solutions were prepared in a sodium phosphate buffer solution containing 11.6 mM of the dibasic, heptahydrate form and 8.4 mM of the monobasic, monohydrate form in de-ionized (DI) water to control solution pH to 7.0. The desired mass of SW/DWCNTs was stirred in the sodium phosphate buffer solution for 10 min (600 RPM, room temperature), then ultrasonicated (QSonica Model Q500 with a ¼” microtip and 80 µm amplitude) for 30 min with intervals of 2 seconds on and 2 seconds off (i.e. an effective time of 15 min). Excessive heating was limited by placing the suspension in an ice bath during sonication. MO was dissolved in the same sodium phosphate buffer solution via stirring for 1 h (600 RPM, room temperature). The dispersed SW/DWCNT suspensions were combined with the MO solution in equal volumes for a total of 100 mL (i.e. 50 mL of each) and stirred at 200 RPM for a set contact time.

An adsorption kinetics study was completed to determine the required contact time for adsorption. A fixed mass of 1 mg SW/DWCNTs was combined with two target MO concentrations: 0.15 mM and 0.025 mM, each studied in triplicate. A 1 mL sample was collected from each beaker every 30 min for 3 h, then every 1 h up to 6 h, then every 24 h up to 48 h. The samples were filtered using a 0.45 µm polyethylene syringe filter (Sun-Sri, SunFlow dissolution filter) to remove suspended SW/DWCNT particles. The UV-Vis absorbance for these samples was measured at 464 nm using a Tecan Spark 10M UV-Vis Spectrophotometer and correlated to MO concentration using the calibration curve provided in Fig. 4.S1a.

To develop the adsorption isotherms, a fixed concentration of MO at 0.025 mM was combined with various masses of CNTs: 10, 5, 2.5, 1, 0.5, 0.1 mg, each studied in duplicate.

SW/DWCNTs were dispersed at a stock concentration of 20 mg/L via sonication, then diluted in sodium phosphate buffer to obtain the desired SW/DWCNT mass before combining with the MO solution. A contact time of 24 h was used, after which the stirrer was turned off and the CNTs were allowed to settle for 24 h. A 1 mL sample was collected from the supernatant at this time and absorbance was measured to estimate equilibrium MO concentration ( $C_E$ , mg/L). The amount of MO adsorbed at equilibrium  $q_E$ (mg/g) was calculated using Equation 1:

$$q_E = \frac{V(C_0 - C_E)}{m} \quad (1)$$

where  $C_0$  is the initial MO concentration (mg/L),  $V$  is the volume (L) and  $m$  (g) is the mass of SW/DWCNT adsorbent used.

#### 4.3.3 CNT-coated Hollow Fiber Membrane Preparation & Characterization

The protocol for preparing the CNT-coated HF membranes is outlined in our previous work [28]. Briefly, a SW/DWCNT suspension was prepared by stirring the desired mass of SW/DWCNTs in DI water for 10 min (600 RPM), then ultrasonicated for an effective time of 15 min using the same settings from Section 4.3.2. A solution of SDS in DI water prepared by stirring for 30 min (600 RPM). The SDS and sonicated SW/DWCNT suspension were stirred together for 15 min (600 RPM) then ultrasonicated for an effective time of 30 min. A solution of PVA in DI water was prepared by stirring for 30 min (600 RPM, 90°C), cooled to room temperature, then combined with the SW/DWCNT-SDS suspension and ultrasonicated for an effective time of 15 min. The mass ratios of SW/DWCNT to SDS and to PVA were maintained at 1:1.5 and 1:10, respectively. The SW/DWCNT-SDS-PVA suspension was filtered in crossflow along the interior, active surface of the PES HF membranes which were sealed individually in a custom crossflow module using epoxy resin (LePage Speed Set Epoxy), giving an effective membrane length of 16

cm. The experimental set-up could accommodate up to three HF membranes, each sealed within a separate module, to be coated in parallel. Feed was supplied using a peristaltic pump (Masterflex Model 7523-20), with feed pressure measured every 3 seconds via a USB transducer (Omega PX409). Crossflow rate was throttled using a needle valve on the retentate line, and further verified via a rotameter (Omega FL3635G, 65 mm). Permeate was collected onto a digital scale where mass was recorded every 30 seconds to measure flow rate for one HF membrane at a time; in parallel operation, permeates for the other HF membranes were manually collected and weighed every 15 min to verify flow rates.

The six-stage process for coating and testing the HF membranes is outlined in our previous work [28]. These stages consisted of: 1) wetting HF membranes in DI water; 2) measuring pure water permeability in dead-end operation with DI water; 3) depositing CNTs in crossflow; 4) curing HF membranes within their individual modules at 100°C for 1h; 5) rewetting HFs in 50/50 isopropanol/DI water then in DI water; 6) measuring CNT-coated HF membrane pure water permeability. CNT-coated HF membranes were prepared at the following conditions: SW/DWCNT feed concentration of 18.8 mg/L, crossflow velocity of 1.06 cm/s (0.5 mL/min) and feed pressure of 0.2 bar. Surface conductivity was measured via a four-point probe (Ossila T2001A3) conductivity meter for the interior coated surface, after CNT-coated HF membranes had been cut and folded open (thin rectangular slice:  $l \times w \times t = 10 \text{ mm} \times 3 \text{ mm} \times 1 \text{ }\mu\text{m}$ ).

#### 4.3.4 *Electrochemical Batch Removal of Methyl Orange*

A batch electrochemical cell was used to verify the electrochemical removal capability of the CNT-coated HF membranes (see Fig. 4.1). A 500 mL solution of 0.025 mM MO in sodium phosphate buffer was prepared (pH = 7.0). Sodium chloride was then added to the solution to achieve a conductivity of 3 mS/cm. In the batch electrochemical cell, a CNT-coated HF membrane

(cut and folded open to expose interior surface,  $5\text{ cm} \times 3\text{ mm}$ ) or stainless steel (SS) needle (20G, 304 SS, 6" length) served as the working electrode, oriented parallel to either a graphite or SS counter electrode (VWR,  $l \times w \times t = 6.5\text{ cm} \times 5\text{ cm} \times 0.5\text{ mm}$ ). The electrodes were spaced  $\sim 0.5\text{ mm}$  apart and the solution was stirred at 200 RPM. Voltage was supplied between the working and counter electrodes using a DC power supply (Letour Variable DC Power Supply Lab 30V 5 A). Electrodes were connected to the circuit via flat SS alligator clips. A Ag/AgCl reference electrode was submerged in the MO solution and connected to the ground port of the DC power supply. A 300  $\mu\text{L}$  sample was taken in 10-min intervals, with UV-Vis absorbance measured and correlated to MO concentration via the calibration curve provided in Fig. 4.S1a. A second calibration curve (see Fig. 4.S1b) was prepared for the batch experiment with the CNT-coated HF membrane working electrode and SS counter electrode using the same MO solution prepared for the batch experiment. The purpose of this was to eliminate any errors due to batch-to-batch differences in concentration, pH, or conductivity.

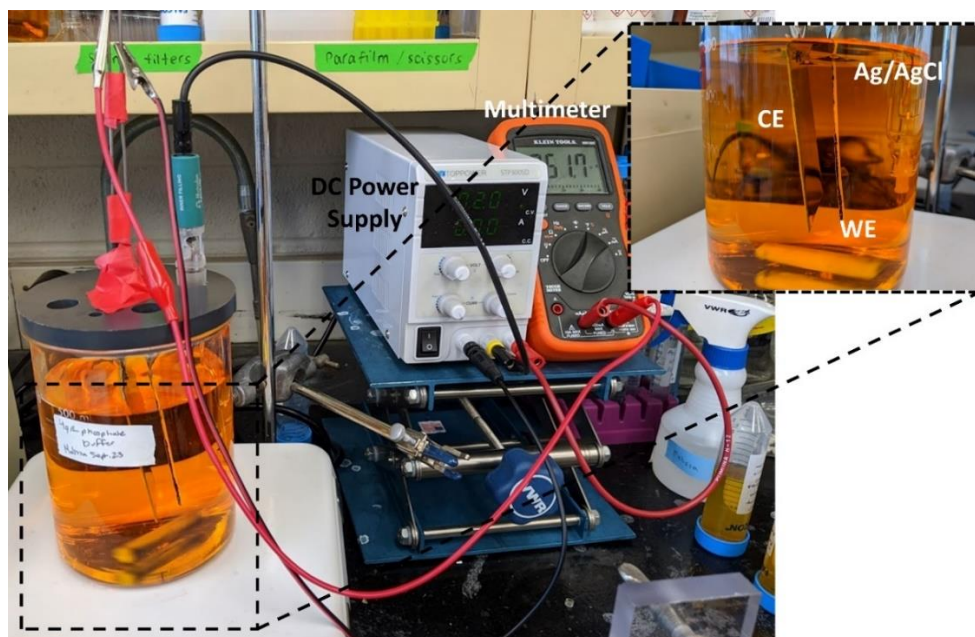


**Figure 4.1.** Photograph of the electrochemical batch removal experimental set-up. Working Electrode (WE), Counter Electrode (CE) and Reference Electrode (Ag/AgCl) are identified in the inset.

#### 4.3.5 *Continuous Electrochemical Removal of Methyl Orange in Crossflow Filtration*

A custom conductive crossflow module was designed to evaluate CNT-coated HF membrane performance in a continuous removal system. A schematic of the continuous flow experimental set-up is shown in Fig. 4.2a. The SS modules are shown in a detailed schematic in Fig. 4.2b and in a digital photograph in Fig. 4.2c. The conductive module served as an electrochemical cell, with the interior coated surface of the HF membrane as the working electrode and the module itself as the counter electrode. Voltage was provided using the same DC power supply described in Section 4.3.4. A 500 mL solution of 0.025 mM MO in sodium phosphate buffer corrected to a pH of 7.0 and conductivity of 3 mS/cm using sodium chloride was provided as the feed source, stirred at 300 RPM. A Ag/AgCl reference electrode was submerged in the feed solution throughout the filtration experiment and connected to the ground port on the DC power supply. The same peristaltic pump and pressure transducers from Section 4.3.3 were used to supply feed and monitor feed pressure. Crossflow velocity was modulated using the same retentate line needle valve and rotameter set-up in Section 4.3.3. The crossflow modules were arranged in parallel to allow for two HF membranes, each sealed within a separate module, to be tested with the same feed solution. Both permeate and retentate lines could be recycled back to the feed reservoir. Three-way stopcock valves were used to redirect flow on the retentate lines such that the crossflow velocity could be independently verified for each HF membrane via the rotameter. These valves were also provided on the permeate line to allow for sampling. Permeate samples were collected every 10 min into 1.7 mL plastic centrifuge tubes. Flow rates were recorded via timed collection and weighing of the centrifuge tubes; MO permeate concentrations were measured by correlating with UV-Vis absorbance measurements using the calibration curve in Fig. 4.S1a.

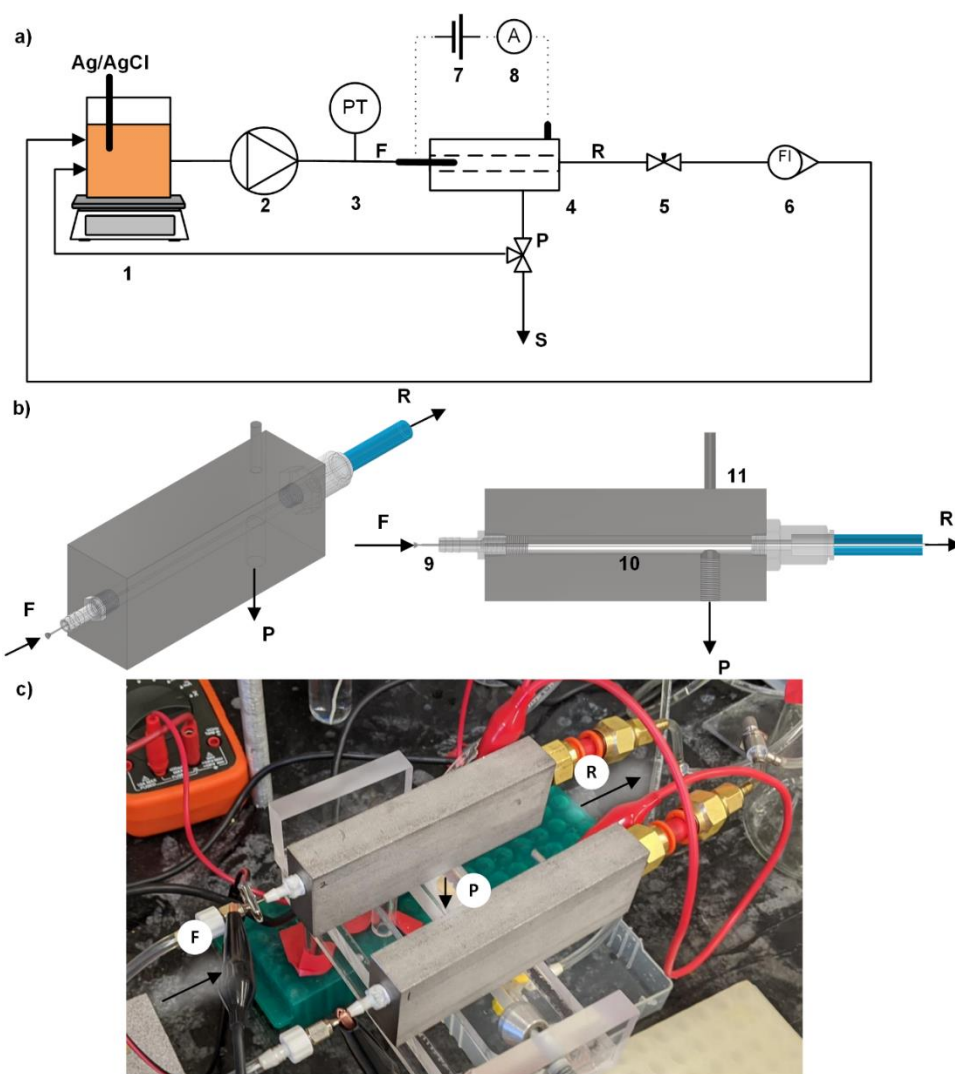


**Figure 4.2.** **a)** Schematic of the continuous electrochemical removal experimental set-up. Numbered items include: (1) Feed reservoir and stir plate; (2) Peristaltic pump; (3) Pressure transducer; (4) Stainless steel conductive membrane module; (5) Needle valve; (6) Rotameter; (7) DC power supply; (8) Ammeter. Feed (F), Retentate (R) and Permeate (P) lines are identified along with the sample point (S) for the permeate line. **b)** Model of the conductive membrane module (Item (4) in (a)). Further identified components include: (9) Metal needle working electrode; (10) CNT-coated HF membrane; (11) Metal connection point to module (counter electrode). **c)** Photograph of the conductive membrane module (Item (4) in (a)).

An alternative sealing technique was used to connect the electric circuit to the interior surface of the CNT-coated HF membranes, as shown in Fig. 4.2b. A 12 cm length of HF membrane was loaded into the module, giving an effective membrane length of 10 cm. The feed end of the HF was sealed using a series of o-rings and washers, similar to the sealing method developed by Kazemi et al. [29], while the retentate end was sealed in epoxy resin as in Section 4.3.3. To contact

the interior surface of the HF membrane, a short metal needle (2", 304 SS) was first inserted into a small piece of rubber, then into the lumen of the HF at the feed end. The feed was then plugged using an NPT fitting. A portion of the metal needle was not sealed within the module; this was used to connect to a piece of tubing to provide feed into the module as well as a contact point for the DC power supply. To connect two modules, two additional wires were attached to: 1) the metal needles, and 2) the SS modules to create a parallel circuit.

#### **4.4 Results & Discussion**

The adsorptive and electrochemical removal capacities of the CNT-coated hollow fiber (HF) membranes were evaluated using methyl orange (MO) as a model azo dye contaminant. Both the HF configuration and internal surface coatings present a novel approach to conductive membrane synthesis, as such the design of a batch and continuous flow module were non-trivial. Several challenges associated with the development of these methods are addressed herein.

##### *4.4.1 SW/DWCNT Adsorptive Removal of Methyl Orange in a Batch System*

To isolate the effect of adsorptive MO removal, a batch study was conducted with the SW/DWCNTs in suspension rather than a surface coating. This simplistic study eliminated several complicating factors from membrane synthesis, including exposed surface area and variations in CNT mass deposited, and assessed the material limitations on adsorptive removal. MO adsorption kinetics were first evaluated to determine the optimal contact time by monitoring the change in MO concentration with contact time for two different initial concentrations: 0.025 and 0.15 mM (see Fig. 4.3a). Both concentration levels showed a reduction in MO concentration which appeared to stabilize within the first 30 min, with minor fluctuation over the next 48 h. This is in agreement with literature data where MO adsorption to MWCNTs has been shown to stabilize within 2 h [22]. However, to ensure good contact for the adsorption isotherm experiments, we used a contact time

of 24 h. At 0.15 mM, MO concentration stabilized around 85-90% of its initial value while at 0.025 mM, this was closer to 60-65%. The lower initial MO concentration was selected for developing the adsorption isotherms due to this more dramatic reduction in MO concentration.

In the adsorption kinetics experimental protocol, suspended CNT particles were removed via a syringe filter; however, a potential bias was noted due to MO adsorption to the polymeric filter material. Initial MO concentration, prior to addition of CNTs, was measured to be ~0.028 mM, but decreased to ~0.026 mM after filtration of this solution using the syringe filter (~7% difference). To eliminate this bias from the adsorption isotherm experiments, the SW/DWCNTs were given 24 h to settle out of solution and MO concentration was measured from the supernatant.

Various masses of SW/DWCNTs (10, 5, 2.5, 1, 0.5, 0.1 mg) were combined with 0.025 mM MO solution to develop the isotherms in Fig. 4.3b. The two lower masses (0.5, 0.1 mg) were excluded due to erroneous behaviour inconsistent with the other data points (see Fig. 4.S2). Interestingly, the data appeared to split into two separate trends. It is unclear what caused this error but may have arisen due to the poor CNT suspension dispersibility in the time delay between preparing each sample. Maintaining CNT suspension homogeneity is notoriously challenging [30], thus CNT dispersibility may have diminished from preparing the first to the last sample. Recommendations to mitigate this in the future include sonicating for a longer time, or in between subsequent sample preparation. Rather than fitting an adsorption model through the average alone, we fit a “maximum” and “minimum” model following the steepest and lowest trends evident in the data. The Temkin isotherm was used to describe the data, expressed in its linear form as:

$$q_E = B \log K_t + B \log C_E \quad (2)$$

Model parameter  $K_t$  represents the equilibrium binding constant (L/mg), and  $B$  is related to the heat of adsorption (J/mol) and in gas systems, can be further described as  $B = RT/b$  where  $R$  is the universal gas constant (8.314 J/K/mol),  $T$  is the temperature (K), and  $b$  is a dimensionless constant related to the adsorption heat [22,31]. The Temkin model assumes the heat of adsorption decreases linearly with increasing adsorbent surface coverage to partially account for indirect adsorbent/adsorbate interactions [31]. Model parameters ( $B, K_t$ ) and  $R^2$  statistics are provided in Table 4.1. The Temkin model has been used to describe a MO/ MWCNT adsorption system previously with a similar quality of model fit ( $R^2 > 0.90$ ); however, the model parameters in this previous work were significantly different than those reported herein with  $B \approx 7 - 12 \text{ J/mol}$  and  $K_t > 1 \text{ L/mg}$  [22]. Langmuir and Freundlich isotherms have also been used to describe similar MO/ CNT adsorption systems [22–24]; however, these models were not representative of the data presented herein (see Fig. 4.3c). The Langmuir model was physically unrealizable with a negative maximum adsorption capacity of  $-77.3 \text{ mg/g}$ . Similarly, the Freundlich model resulted in an inverse trend with a positive exponent of 1.75. Given the range of error in the data and the inconsistency with literature, it is possible these experiments do not truly describe the adsorption behaviour of the SW/DWCNTs and should be repeated in the future to verify.

**Table 4.1.** Isotherm parameters for adsorptive removal of MO by SW/DWCNTs

Models Parameters	Maximum	Average	Minimum
$B$	371.55	277.25	180.43
$K_t$	0.28	0.29	0.34
$R^2$	0.96	0.98	0.99

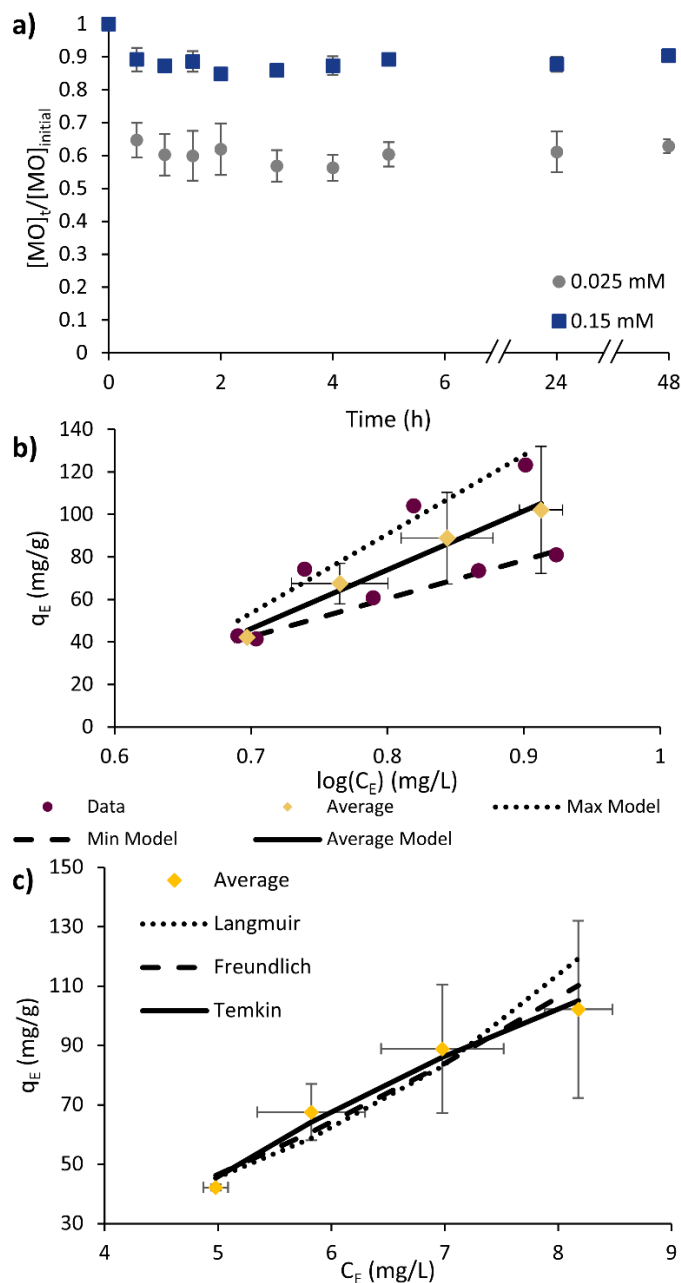


**Fig. 4.3 a)** Normalized methyl orange (MO) concentration as a function of contact time with 1 mg of SW/DWCNTs at two concentration levels of MO: 0.025 mM and 0.15 mM. Error bars represent the standard deviation between triplicate experiments. **b)** Temkin adsorption isotherms for a fixed 0.025 mM solution of MO after 24 h contact time with varying masses of SW/DWCNTs (10, 5, 2.5, and 1 mg). Raw data is shown as the maroon circles while the average of duplicate experiments at each SW/DWCNT mass is shown as the yellow diamonds. Error bars on the x-axis represent the standard deviation in equilibrium MO concentration and error bars on the y-axis represent the standard deviation in calculated amount of MO adsorbed for the duplicate experiments. **c)** Langmuir, Freundlich and Temkin adsorption isotherm models for the same adsorption data in b. Fitted models: Langmuir  $q_E = (-0.074 \times -77.3 \times C_E)/(1 + (-0.074) \times C_E)$ , Freundlich  $q_E = 2.80 \times C_E^{1.75}$ , Temkin  $q_E = 277.25 \times \log(0.29) + 277.25 \times \log(C_E)$ .

#### 4.4.2 *Electrochemical Batch Removal of Methyl Orange*

To verify the electrochemical activity of the CNT-coated HF membranes, a batch experiment was conducted by suspending the working (i.e. membrane) and counter electrode in a beaker with 500 mL of a 0.025 mM MO solution. A negative potential was applied across the working electrode, thus it served as a cathode to induce electrochemical reduction of MO. While this simple batch study was not a true representation of a continuous flow membrane filtration system, it allowed the electrochemical removal capability of the CNT-coated HF membranes to be isolated from further complicating factors such as contact time or shear rates, and for independent assessment of electrochemical variables including applied potentials, type of counter electrode, and electrode spacing.

The change in bulk MO concentration over time for two different working electrodes are shown in Fig. 4.4: 1) a control experiment with a stainless steel (SS) needle working electrode; and 2) CNT-coated HF membrane, cut and folded open to expose the interior coated surface to the MO solution. The applied potential for the control experiment was -2V for 2h, then -5V for another 1h. For the CNT-coated HF membrane, -2V was applied for 2h, then 2V for another 2h. The working electrode in the control experiment was the same needle material used to form the contact point with the CNT-coated HF membrane in the conductive crossflow module (Fig. 4.1). The purpose of this control was to isolate the electrochemical removal effects of the needle from the CNT-coated HF membrane which could become confounded in the final design. Under an applied potential of -2V, the electrochemical cell achieved ~28% MO removal with the SS needle working electrode after 2 h which increased to ~40% after another 1 h at -5V. As the SS needle appeared to have a strong effect on MO degradation, it may prove difficult to separate electrochemical removal due to the CNT-coated HF membrane from the needle contact point.

In the batch configuration with the CNT-coated HF membrane as a working electrode, no effective MO removal was observed after 2 h at -2V, nor after another 2 h at 2V. This observation was surprising due to the high expected surface conductivity for membranes coated under the same crossflow conditions ( $\sim 300$  S/m) and the successful MO degradation in other works with CNT-coated membranes. Previous research with similar CNT-coated membranes in flat sheet has achieved MO removal rates of 76% [16] and 98% [15] at -2V in under 2 h. Increasing potential may have improved removal, for instance Omi et al. achieved 98% removal at -3V [12]; however, this trend is not consistent in literature as Vecitis et al. found removal began to diminish beyond -2V (93% at -3V, compared to 98% at -2V [15]). The CNT-based membranes in these previous works contained high masses or densities of CNTs (10 mg SW/DWCNTs [16], MWCNT sheet [15]) with conductivities several orders of magnitude higher than those expected from our crossflow deposition process ( $\sim 100,000$  S/m [16],  $\sim 4000$  S/m [12] compared to  $\sim 300$  S/m herein). Depositing a thicker, more conductive film of CNTs may have improved electrochemical removal, however other works have also shown effective electrochemically induced antifouling [11] and charged particle removal [17] at much lower conductivities ( $\sim 400$  S/m [11];  $\sim 1.2$  S/m [17]). The surface area available for electrochemical removal was smaller than those typical for flat sheet membranes (1.5 vs 3.8 cm<sup>2</sup> [16]) but not so significant to cause this dramatic difference in removal efficiency. Another potential issue is that by cutting and folding open the HF membrane, the deposited CNT layer may have cracked and inhibited propagation of an electric current.

A direct comparison between the control and the CNT-coated HF membrane tests can be made within the first 2 h as both were exposed to a -2V potential; however, removal was only achieved with the SS needle control. Another notable difference between these experiments was the selection of counter electrode. The counter electrode used in the control was a graphite sheet;

this was changed to a SS sheet in the CNT-coated HF membrane experiment to simulate the conductive crossflow module design more closely. It is unlikely this impacted electrochemical removal, as SS counter electrodes have been used in similar CNT membrane based electrochemical systems previously with successful MO removal [16].

A similar batch study was completed in a horizontal orientation (see Fig. 4.S3a) for a batch volume of 50 mL (stirred at 900 RPM) to determine if MO removal with the CNT-coated HF membrane could be detected in a smaller volume. MO concentration over time is shown in Fig. 4.S3b for two types of connections to the working and counter electrodes: SS and copper alligator clips. Final MO concentration did not change significantly with the SS clips after 3 h and appeared to increase over time with the copper clips, likely due to oxidation of the alligator clips themselves as they were submerged in MO solution. A similar effect was not observed in the vertical orientation as the confounding effect from the submerged clips could be eliminated.

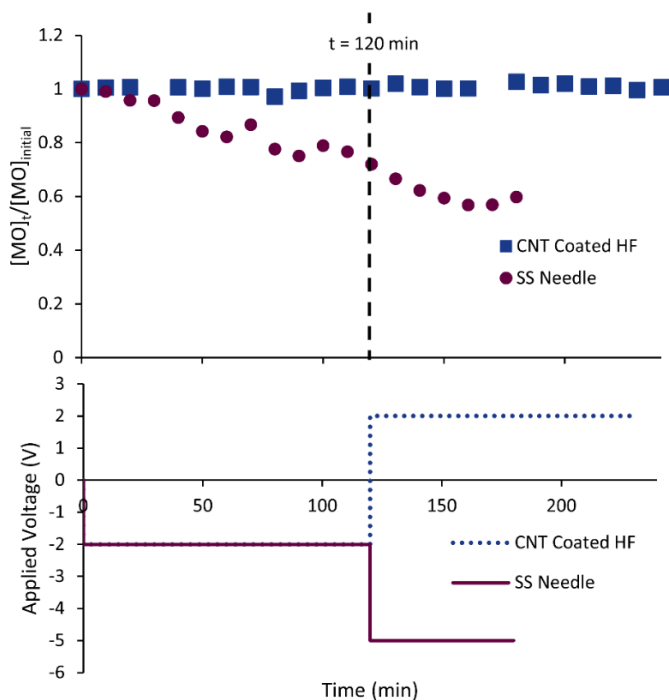


**Figure 4.4.** Normalized bulk methyl orange (MO) concentrations over time for 500 mL batch tests with two types of working electrodes: CNT-coated HF (blue squares) and stainless steel needle control (maroon circles). Step changes in applied are reported in the bottom panel.

#### 4.4.3 *Continuous Removal*

Using the conductive crossflow module shown in Fig. 4.2b, MO removal in continuous filtration operation was evaluated for the CNT-coated HF membranes and the unmodified PES HF membranes as a control. The control experiments were repeated for two separate PES HF membranes in dead-end operation, under both no applied voltage and a -2V potential (i.e. four HF membranes in total). No MO removal was detected at either condition (see Fig. 4.S4) as expected due to the large pore size of the support PES HF membranes (0.2  $\mu\text{m}$ ) and the insulating polymeric surface. MO removal efficiency was then evaluated for two CNT-coated HF membranes, with properties summarized in Table 4.2. Two 6-h experiments were completed sequentially for these CNT-coated HF membranes, both at a feed rate of 0.5 mL/min and crossflow rate of 0.1 mL/min: 1) retentate recycle (see Fig. 4.5a) and 2) permeate and retentate recycle (see Fig. 4.5b). An applied potential of -5V was supplied after 30 min. Both conditions showed no significant MO removal over the 6 h filtration period. Permeate flow rates were different between the two HF membranes, likely due to the significant difference in permeabilities as shown in Table 4.2.

The lack of MO removal in the CNT-coated HF membrane crossflow experiments was consistent with the batch experiments (Section 4.4.2), but not expected based on the high removal efficiency observed for similar CNT-coated membranes in flat sheet [12,15,16]. Due to the consistency of this poor performance, the major limiting factor for MO removal was likely the CNT-coated HF membranes themselves. As mentioned in Section 4.4.2, this may be due to the lower conductivity observed in these membranes over those used in previous literature for MO removal. For the continuous removal experiments in particular, the small diameter of the HF membranes (1 mm) limited the volume of feed exposed to the membrane surface ( $\sim 0.1$  mL internal HF volume), therefore longer recycle times may be required to optimize contact time.

**Table 4.2.** Properties for the CNT-coated HF membranes used in the continuous removal experiments. Error ranges for surface conductivities represent the standard deviation between triplicate four-point probe measurements. Error ranges for permeabilities represent the 95% confidence intervals for the slopes of the flux/pressure curves.

HF Membrane	Surface Conductivity (S/m)	Permeability (LMH/bar)
CNT-HF-1	$268 \pm 106$	$357 \pm 42$
CNT-HF-2	$338 \pm 46$	$1348 \pm 160$

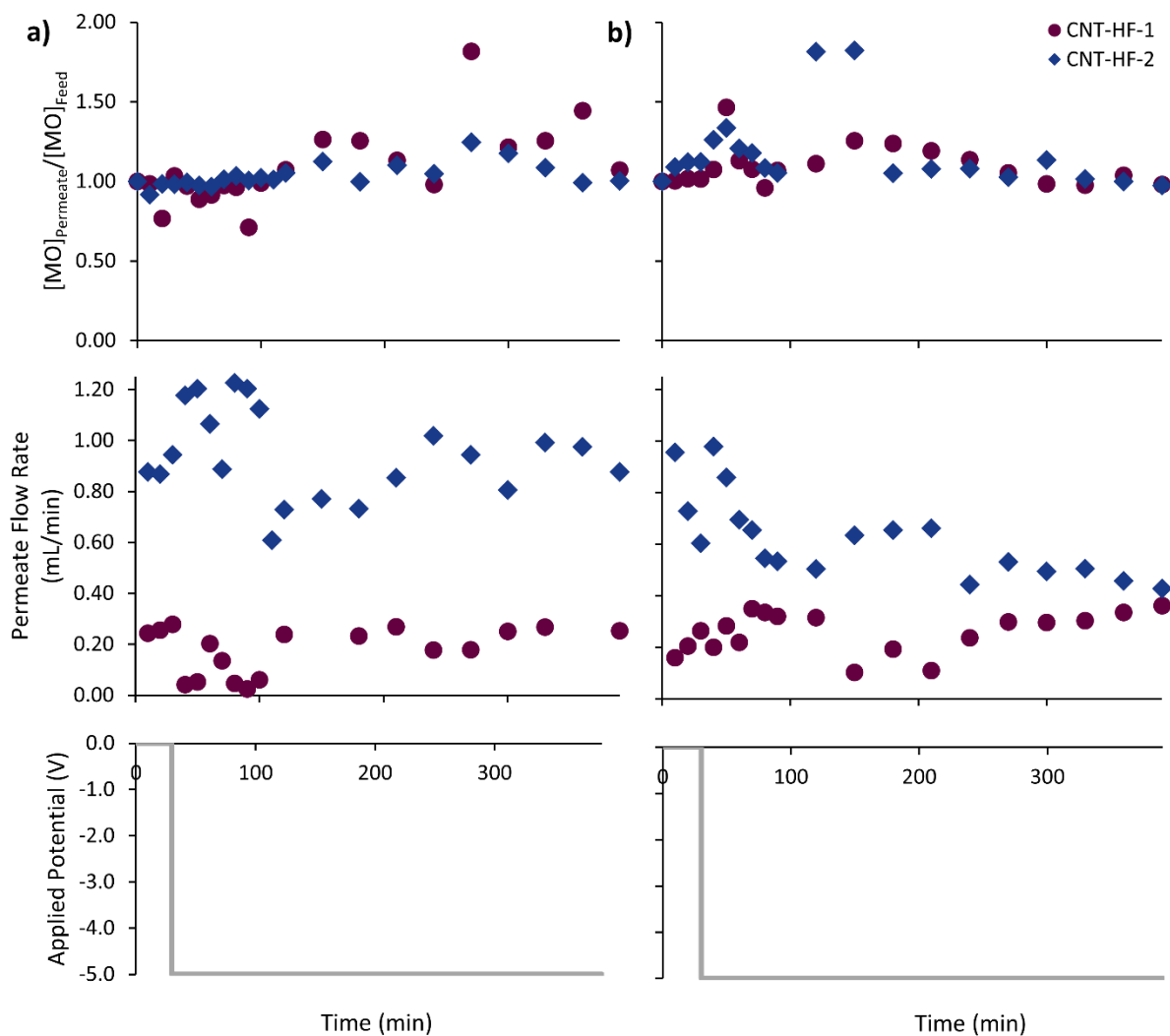


**Figure 4.5.** Normalized permeate methyl orange (MO) concentration and permeate flow rate over time for crossflow continuous removal experiments with two CNT-coated HF membranes at a feed flow rate of 0.5 mL/min and crossflow rate of 0.1 mL/min under two recycle modes of operation: a) retentate recycle; b) permeate and retentate recycle. A potential of -5V was applied after 30 min.

In the batch experiments, a potential confounding effect was discovered as the SS needle used to contact the conductive membrane surface showed ~40% MO removal on its own. Theoretically, this effect should have compounded with MO removal associated with the CNT-coated HF membrane in the continuous removal experiments, however no MO removal was detected. It is possible the removal associated with the SS needle was eliminated in this set-up due to its smaller surface area (2" in continuous test vs 6" in batch test) and poor proximity to the counter electrode. However, this may also indicate that the current configuration is not conducive for electrochemical effects. In this configuration, the primary mechanism for electrochemical removal would be capacitive surface charge. The feed is only exposed to the working electrode while an insulating polymer layer and the permeate separate the working and counter electrodes; this system resembles a capacitor with the polymer support and permeate serving as the dielectric material. An alternative configuration where the feed solution contacts both the working and counter electrodes would allow for both electric field and surface charge effects. In a study by Zhang et al., both configurations were evaluated for organic fouling mitigation and while some flux recovery was evident under the capacitive surface charge configuration, the greatest performance was observed with the combination of both electric field (i.e. electrophoresis) and charged (i.e. electrostatic repulsion) effects [13]. This alternative configuration has been used in evaluation of similar flat sheet membranes [15][16] but poses an interesting design challenge with the HF membranes due to the small diameter (ID: 1 mm) and interior surface coating. Implementation of this alternative configuration, for example with a different counter electrode or an exterior HF membrane surface coating, would be a useful subject for future research.

## 4.5 Conclusions

In this work, we have developed experimental methods for evaluating the adsorptive and electrochemical removal capabilities of conductive CNT-coated membranes in a hollow fiber (HF) format using methyl orange (MO) as a model contaminant. Batch adsorption isotherm studies were conducted to evaluate the adsorptive capacity of the SW/DWCNTs used to fabricate these CNT-coated HF membranes. Despite the good equilibrium concentration stability over time, the error in the adsorption isotherm plot resulted in poor fitting for the Langmuir and Freundlich models typically used to describe MO/ CNT adsorption systems. More data is required to conclusively state whether the Temkin isotherm models developed herein truly describe adsorption of MO to the SW/DWCNTs. No significant electrochemical removal was apparent for the CNT-coated HF membranes in both batch and continuous configurations, despite the confirmed surface conductivity  $\sim 300$  S/m. In the batch experiments, up to 40% MO removal was achieved with the stainless steel needle working electrode and graphite counter electrode at a  $-5V$  potential, indicating a potential confounding effect from the needle used to contact the conductive membrane surface in the crossflow modules. This effect was not apparent however in the continuous removal tests where no significant MO removal was detected after 6 h filtration in two modes of recycle operation: 1) retentate only and 2) permeate and retentate. Further optimization of experimental parameters in both configurations is required to determine the effective combination for MO removal, including choice of counter electrode, electrode spacing, target surface conductivity and contact time. Alternative designs for the continuous removal tests should also be considered to take advantage of both capacitive charge and electric field effects for more efficient electrochemical removal and antifouling performance.

## 4.6 References

- [1] H. Ben Mansour, R. Mosrati, D. Corroler, K. Ghedira, D. Barillier, L. Chekir, In vitro mutagenicity of Acid Violet 7 and its degradation products by *Pseudomonas putida* mt-2: Correlation with chemical structures, *Environ. Toxicol. Pharmacol.* 27 (2009) 231–236. <https://doi.org/10.1016/j.etap.2008.10.008>.
- [2] N. Al-Bastaki, Removal of methyl orange dye and Na<sub>2</sub>SO<sub>4</sub> salt from synthetic waste water using reverse osmosis, *Chem. Eng. Process. Process Intensif.* 43 (2004) 1561–1567. <https://doi.org/10.1016/j.cep.2004.03.001>.
- [3] D. De Jager, M.S. Sheldon, W. Edwards, Colour removal from textile wastewater using a pilot-scale dual-stage MBR and subsequent RO system, *Sep. Purif. Technol.* 135 (2014) 135–144. <https://doi.org/10.1016/j.seppur.2014.08.008>.
- [4] B. Van Der Bruggen, C. Vandecasteele, T. Van Gestel, W. Doyenb, R. Leysenb, A Review of Pressure-Driven Membrane Processes, *Environ. Prog.* 22 (2003) 46–56.
- [5] S. Surawanvijit, A. Rahardianto, Y. Cohen, An Integrated approach for characterization of polyamide reverse osmosis membrane degradation due to exposure to free chlorine, *J. Memb. Sci.* 510 (2016) 164–173. <https://doi.org/10.1016/j.memsci.2016.02.044>.
- [6] T. Robinson, G. McMullan, R. Marchant, P. Nigam, Remediation of dyes in textile effluent: a critical review on current treatment technologies with a proposed alternative, *Bioresour. Technol.* (2001) 247–255. <https://doi.org/10.1504/IJEP.2004.004190>.
- [7] C.A. Martínez-Huitle, E. Brillas, Decontamination of wastewaters containing synthetic organic dyes by electrochemical methods: A general review, *Appl. Catal. B Environ.* 87 (2009) 105–145. <https://doi.org/10.1016/j.apcatb.2008.09.017>.
- [8] J. Huang, Z. Wang, J. Zhang, X. Zhang, J. Ma, Z. Wu, A novel composite conductive microfiltration membrane and its anti-fouling performance with an external electric field in membrane bioreactors, *Sci. Rep.* 5 (2015) 1–9. <https://doi.org/10.1038/srep09268>.
- [9] S.Y. Yang, C.D. Vecitis, H. Park, Electrocatalytic water treatment using carbon nanotube filters modified with metal oxides, *Environ. Sci. Pollut. Res.* 26 (2019) 1036–1043. <https://doi.org/10.1007/s11356-017-8495-6>.
- [10] Y. Liu, J.H. Dustin Lee, Q. Xia, Y. Ma, Y. Yu, L.Y. Lanry Yung, J. Xie, C.N. Ong, C.D. Vecitis, Z. Zhou, A graphene-based electrochemical filter for water purification, *J. Mater. Chem. A.* 2 (2014) 16554–16562. <https://doi.org/10.1039/c4ta04006f>.
- [11] C.F. de Lannoy, D. Jassby, K. Gloe, A.D. Gordon, M.R. Wiesner, Aquatic biofouling prevention by electrically charged nanocomposite polymer thin film membranes, *Environ. Sci. Technol.* 47 (2013) 2760–2768. <https://doi.org/10.1021/es3045168>.
- [12] F.R. Omi, M.R. Choudhury, N. Anwar, A.R. Bakr, M.S. Rahaman, Highly Conductive Ultrafiltration Membrane via Vacuum Filtration Assisted Layer-by-Layer Deposition of Functionalized Carbon Nanotubes, *Ind. Eng. Chem. Res.* 56 (2017) 8474–8484. <https://doi.org/10.1021/acs.iecr.7b00847>.

- [13] Q. Zhang, C.D. Vecitis, Conductive CNT-PVDF membrane for capacitive organic fouling reduction, *J. Memb. Sci.* 459 (2014) 143–156. <https://doi.org/10.1016/j.memsci.2014.02.017>.
- [14] W. Duan, A. Dudchenko, E. Mende, C. Flyer, X. Zhu, D. Jassby, Electrochemical mineral scale prevention and removal on electrically conducting carbon nanotube-polyamide reverse osmosis membranes, *Environ. Sci. Process. Impacts*. 16 (2014) 1300–1308. <https://doi.org/10.1039/c3em00635b>.
- [15] C.D. Vecitis, G. Gao, H. Liu, Electrochemical carbon nanotube filter for adsorption, desorption, and oxidation of aqueous dyes and anions, *J. Phys. Chem. C*. 115 (2011) 3621–3629. <https://doi.org/10.1021/jp111844j>.
- [16] A.J. Sutherland, M.X. Ruiz-Caldas, C.F. de Lannoy, Electro-catalytic microfiltration membranes electrochemically degrade azo dyes in solution, *J. Memb. Sci.* 611 (2020) 118335. <https://doi.org/10.1016/j.memsci.2020.118335>.
- [17] G. Wei, S. Chen, X. Fan, X. Quan, H. Yu, Carbon nanotube hollow fiber membranes: High-throughput fabrication, structural control and electrochemically improved selectivity, *J. Memb. Sci.* 493 (2015) 97–105. <https://doi.org/10.1016/j.memsci.2015.05.073>.
- [18] L. Guo, Y. Jing, B.P. Chaplin, Development and Characterization of Ultrafiltration TiO<sub>2</sub> Magnéli Phase Reactive Electrochemical Membranes, *Environ. Sci. Technol.* 50 (2016) 1428–1436. <https://doi.org/10.1021/acs.est.5b04366>.
- [19] D. Liu, X. Chen, B. Bian, Z. Lai, Y. Situ, Dual-Function Conductive Copper Hollow Fibers for Microfiltration and Anti-biofouling in Electrochemical Membrane Bioreactors, *Front. Chem.* 6 (2018) 1–10. <https://doi.org/10.3389/fchem.2018.00445>.
- [20] J. Liu, C. Tian, J. Xiong, B. Gao, S. Dong, L. Wang, Polypyrrole vapor phase polymerization on PVDF membrane surface for conductive membrane preparation and fouling mitigation, *J. Chem. Technol. Biotechnol.* 93 (2018) 683–689. <https://doi.org/10.1002/jctb.5416>.
- [21] L.L. Xu, Y. Xu, L. Liu, K.P. Wang, D.A. Patterson, J. Wang, Electrically responsive ultrafiltration polyaniline membrane to solve fouling under applied potential, *J. Memb. Sci.* 572 (2019) 442–452. <https://doi.org/10.1016/j.memsci.2018.11.026>.
- [22] Y. Yao, H. Bing, X. Feifei, C. Xiaofeng, Equilibrium and kinetic studies of methyl orange adsorption on multiwalled carbon nanotubes, *Chem. Eng. J.* 170 (2011) 82–89. <https://doi.org/10.1016/j.cej.2011.03.031>.
- [23] D. Zhao, Y. Ding, S. Chen, M. Wang, X. Zhang, Adsorption Isotherms and Thermodynamics Studies for the Removal Methyl Orange from Wastewaters Using Multiwalled Carbon Nanotubes, *Asian J. Chem.* 26 (2014) 1440–1442.
- [24] L. Wang, M. Zhang, C. Zhao, S. Yang, Adsorption behavior of ferromagnetic carbon nanotubes for methyl orange from aqueous solution, *J. Nanosci. Nanotechnol.* 16 (2016) 2804–2810. <https://doi.org/10.1166/jnn.2016.11602>.
- [25] J.D. Seader, E.J. Henley, D.K. Roper, *Separation Process Principles*, 3rd ed., John Wiley & Sons, Inc., 2011.

- [26] C.M. Werner, K.P. Katuri, A.R. Hari, W. Chen, Z. Lai, B.E. Logan, G.L. Amy, P.E. Saikaly, Graphene-Coated Hollow Fiber Membrane as the Cathode in Anaerobic Electrochemical Membrane Bioreactors - Effect of Configuration and Applied Voltage on Performance and Membrane Fouling, *Environ. Sci. Technol.* 50 (2016) 4439–4447. <https://doi.org/10.1021/acs.est.5b02833>.
- [27] G. Wei, J. Dong, J. Bai, Y. Zhao, Y. Li, Structurally Stable, Antifouling, and Easily Renewable Reduced Graphene Oxide Membrane with a Carbon Nanotube Protective Layer, *Environ. Sci. Technol.* 53 (2019) 11896–11903. <https://doi.org/10.1021/acs.est.9b03129>.
- [28] M.J. Larocque, D.R. Latulippe, C.F. de Lannoy, Formation of electrically conductive hollow fiber membranes via crossflow deposition of carbon nanotubes – addressing the conductivity/permeability trade-off, *J. Memb. Sci.* (2020). <https://doi.org/10.1016/j.memsci.2020.118859>.
- [29] A.S. Kazemi, L. Boivin, S. Mi Yoo, R. Ghosh, D.R. Latulippe, Elucidation of filtration performance of hollow-fiber membranes via a high-throughput screening platform, *J. Memb. Sci.* 533 (2017) 241–249. <https://doi.org/10.1016/j.memsci.2017.03.042>.
- [30] K.G. Dassios, P. Alafogianni, S.K. Antiohos, C. Leptokaridis, N.M. Barkoula, T.E. Matikas, Optimization of sonication parameters for homogeneous surfactant assisted dispersion of multiwalled carbon nanotubes in aqueous solutions, *J. Phys. Chem. C.* 119 (2015) 7506–7516. <https://doi.org/10.1021/acs.jpcc.5b01349>.
- [31] N. Can, B.C. Ömür, A. Altındal, Modeling of heavy metal ion adsorption isotherms onto metallophthalocyanine film, *Sensors Actuators, B Chem.* 237 (2016) 953–961. <https://doi.org/10.1016/j.snb.2016.07.026>.
- [32] C.F. De Lannoy, D. Jassby, K. Gloe, A.D. Gordon, M.R. Wiesner, Aquatic biofouling prevention by electrically charged nanocomposite polymer thin film membranes, *Environ. Sci. Technol.* (2013) 1304–1319.

## 4.7 Supplementary Information

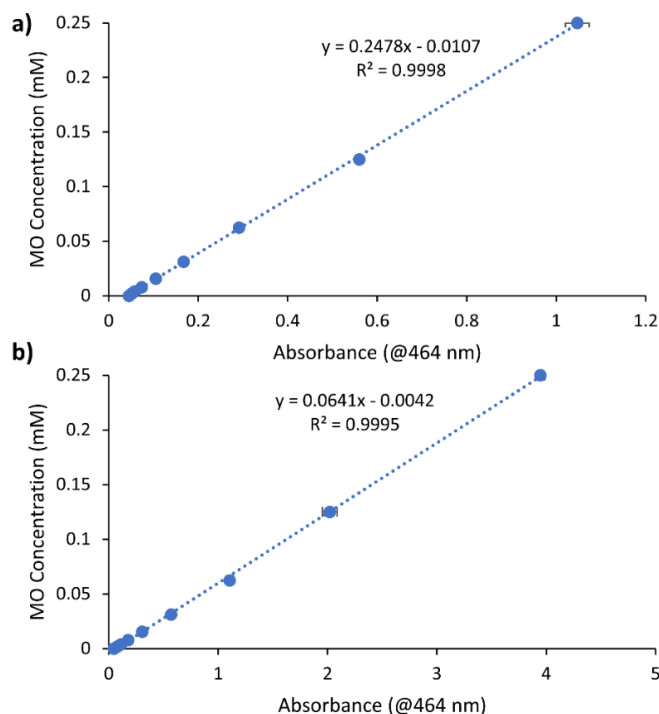


**Figure 4.S1.** UV-Vis calibration curves relating methyl orange (MO) concentration to absorbance at 454 nm. **a)** Curve developed for use with 48-well plates, used for majority of experiments. **b)** Curve developed for use with 96-well plates, used for electrochemical batch removal test in vertical orientation with the CNT-coated HF membranes.

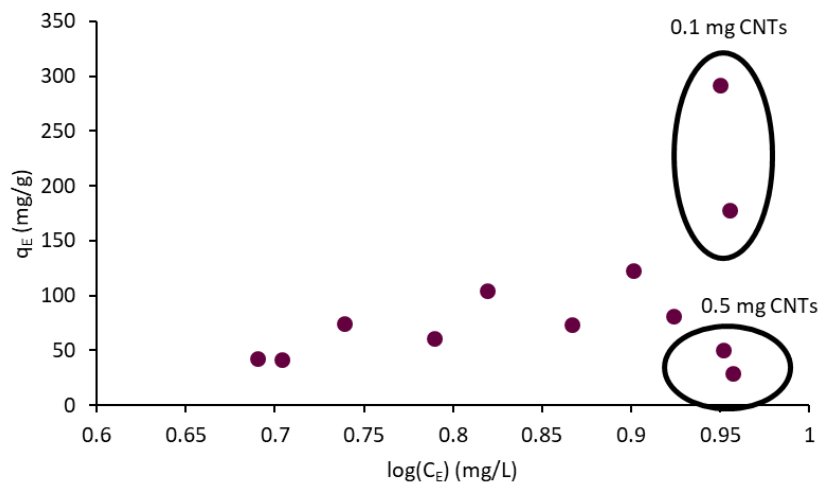


**Figure 4.S2.** Raw adsorption data for a fixed 0.025 mM solution of MO after 24 h contact time with varying masses of SW/DWCNTs (10, 5, 2.5, 1, 0.5, 0.1 mg). Data at 0.5 and 0.1 mg CNTs shown in circles due to their erroneous behaviour.

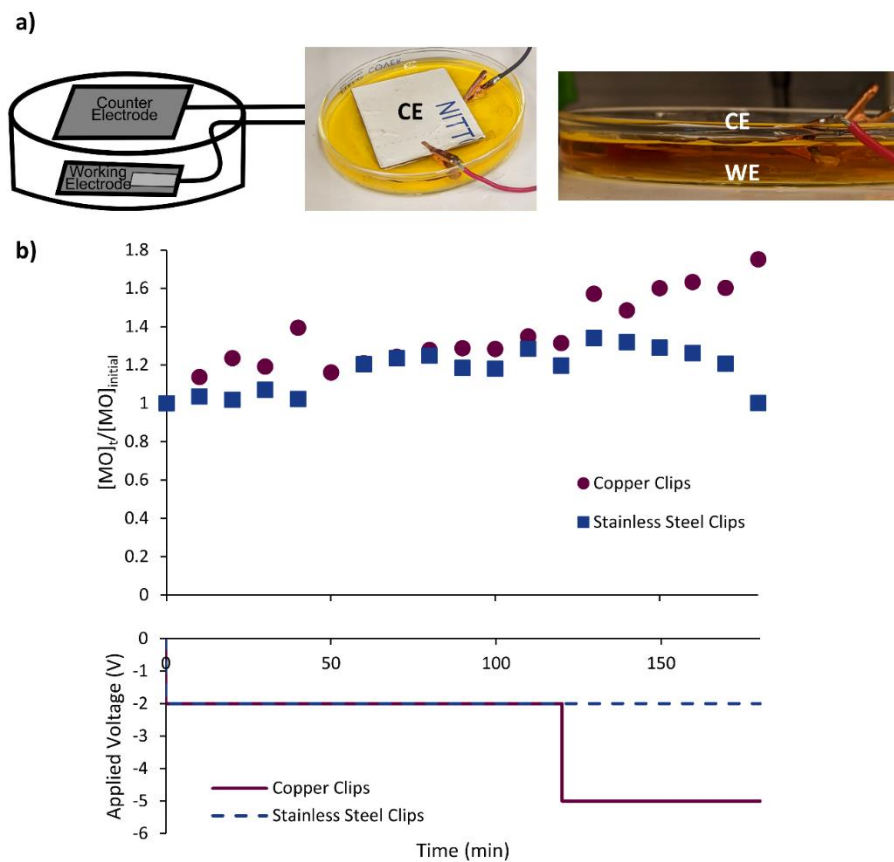


**Figure 4.S3.** a) Schematic and photographs of the 50 mL horizontal configuration for the electrochemical batch removal experiments with the working (WE) and counter electrodes (CE) identified. b) Normalized bulk methyl orange (MO) concentrations over time for the 50 mL batch tests in horizontal configuration with two types of electrode connections: copper (maroon circles) and stainless steel (blue squares) alligator clips. Step changes in applied are reported in the bottom panel.

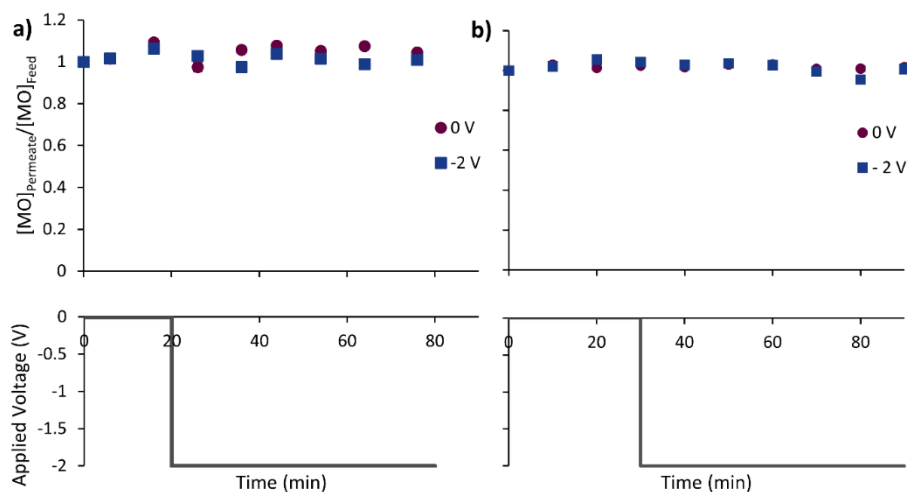


**Figure 4.S4.** Unmodified PES HF membrane control filtration experiments with the continuous removal experimental set-up. Tests a & b are identical, each with two different HF membranes (four membranes in total).

## Chapter 5: Conclusions & Future Work

### 5.1 Conclusions

The goal of this project was to fabricate an electrically conductive membrane (ECM) in an industrially relevant hollow fiber (HF) format and ensure equal performance along the HF. Previous works have demonstrated ECM success in mitigating fouling, enhancing separations, and inducing electrochemical degradation of contaminants largely in flat sheet format; however, there had been limited research into alternative formats like HF and specifically how deposition-based fabrication processes can be optimized. To this end, we deposited single walled/ double walled carbon nanotubes (SW/DWCNTs) onto the interior surface of commercial polyether sulfone (PES) HF membranes in a “crossflow deposition” technique. Scanning electron microscopy (SEM) images confirmed successful surface localization of the CNT layer. Flow properties (feed pressure, crossflow velocity) and CNT feed concentration were adjusted to optimize surface conductivity and hydraulic permeability, the two metrics that define ECM electro-functional capability and process throughput, respectively. We established a trade-off between surface conductivity and hydraulic permeability by plotting these metrics against each other for 29 different CNT-coated HF membranes. This method was extended by obtaining literature data from 38 papers, covering a variety of conductive materials, separation types, membrane configurations, and intended applications in the ECM field. A similar trade-off was evident for each class of conductive material used in ECM fabrication (graphitic nanomaterials, metals, and conductive polymers). Finally, we developed batch and continuous tests for evaluating the capability of the CNT-coated HF membranes for electrochemical degradation of methyl orange (MO) as a model contaminant.

A parallelized crossflow deposition experimental set-up allowed for testing of 50 different HF membranes in a robust statistical study. The effects of feed pressure and crossflow velocity were analyzed in a  $2^2$  full factorial design-of-experiments study where both were found to significant impact surface conductivity, and only crossflow velocity significantly impacted permeability. These observations were consistent with particle deposition theory where the impact of these parameters on permeation drag and inertial lift forces determine whether deposition occurs. Interestingly, the highest permeability (~2900 LMH/bar) and conductivity (~670 S/m) values were both obtained at the high pressure and high crossflow velocity condition. A “drying-out” effect was evident for poorly coated membranes resulting in permeabilities up to ~10 times lower than well-coated membranes. We suspect the surface coatings protected the internal pore structure from collapse during the curing process. Increasing the CNT feed concentration resulted in higher conductivities likely due to greater particle loading. Membranes coated at this higher CNT feed concentration exhibited greater variation in surface conductivity along the length of the fiber which we attributed to variations in the permeation driving force due to a substantial increase in feed pressure over time. These experiments clearly showed that the selection of flow parameters during deposition have a significant impact on ECM properties.

In the gas separation membrane field, Robeson first described the permeability/ selectivity trade-off by plotting these metrics against each other and fitting a model to describe the upper achievable limit [1]. We used an analogous method to establish the inverse relationship between measured surface conductivity and permeability using the results for 29 different membranes from the crossflow deposition experiments. Feed pressure, crossflow velocity and CNT feed concentration all significantly impacted the magnitude of this trade-off. An upper limit line was established to describe this inverse relationship as:  $C = 1.27 \times 10^{10} \cdot L_p^{-2.00}$ .

The conductivity/ permeability trade-off was further extended to ECM literature where conductivity and permeability data for 80 membranes from 38 different papers was reviewed. A series of conductivity/ permeability plots was created for each major class of conductive material used in ECM fabrication: graphitic nanomaterials, metals, and conductive polymers. Metallic-based ECMs out-performed the other classes achieving conductivities up to three orders of magnitude greater, while permeabilities were more comparable across all three classes. Collected data was further analyzed in terms of distribution of separation type (i.e. MF/UF/NF/RO/FO), membrane configuration (i.e. flat sheet, HF, tubular), and application (i.e. antifouling, redox, enhanced separation). This analysis revealed that although metallic-based ECMs performed best, they were also largely intended for high flux MF applications (~68%) which partially explains their ability to maintain both high conductivity and permeability. Furthermore, a wide diversity in performance testing was evident with 35 different pollutants or tests in 63 total experiments. This variety indicated a lack of standardization for evaluating ECM performance, making it difficult to compare different fabrication methods, and revealed limited testing with realistic water sources.

Finally, we developed a series of experimental methods for evaluating the adsorptive and electrochemical removal capabilities of the CNT-coated HF membranes using methyl orange (MO) as a model azo dye contaminant. Adsorption of MO was studied in batch experiments with dispersed SW/DWCNTs to determine their maximum adsorptive capacity. Equilibrium MO concentration was stable with time but had poor repeatability likely due to challenges with maintaining CNT dispersion homogeneity. Electrochemical removal with the CNT-coated HF was evaluated in a 500 mL batch and continuous recycled operation using a custom crossflow module where the interior coated surface of the HF membrane served as the working electrode and the stainless steel module served as the counter electrode. No significant MO removal was achieved

with the CNT-coated HF membranes in both batch and continuous configurations, indicating a potential issue with the CNT-coated HF membranes themselves. Higher conductivities in the range of previous works may be required to achieve electrochemical removal of MO (~100,000 S/m [2], ~4000 S/m [3] compared to 300 S/m herein). Although relatively long-term 6-h recycle experiments were conducted, a longer contact time may be needed due to the small diameter of the HF membranes (~0.1 mL internal volume).

## 5.2 Future Work

Further testing is required to verify the electro-functional capability of the CNT-coated HF membranes developed via crossflow deposition. The successful MO oxidation achieved with similar CNT-based ECMs in previous works [2–4] indicates it should be possible to achieve MO removal with the CNT-coated HF membranes. However, several parameters should be optimized including surface conductivity, applied voltage, counter electrode material, electrode spacing, and contact time. Alternative configurations for the continuous module, with the feed solution exposed to both working (i.e. membrane surface) and counter electrodes, should be considered to take advantage of capacitive charge and electric field effects. To further evaluate adsorption, isotherms should be developed with the CNT-coated HF membranes instead of CNTs in suspension; the reduction in surface area due to surface deposited CNTs should decrease adsorptive removal.

As MO only served as a model contaminant, more complicated compounds with multi-staged oxidation/ reduction pathways should be studied to further evaluate electrochemical degradation capabilities. Example compounds include phenol or tetracycline which require 28 and 106 electrons respectively for complete oxidation [5]. High performance liquid chromatography and mass spectrometry analysis on permeate samples could reveal more information on degradation products and whether full or partial redox degradation can be achieved [5,6].

Additional ECM applications such as antifouling should also be investigated and with more realistic feed sources (e.g. municipal wastewater). ECMs have had prior success with mitigating biofouling, even in the lower surface conductivity ranges (e.g. ~400 S/m [7]) which is more consistent with the optimal conductivity/ permeability achieved in our crossflow deposition technique. Fouling is one of the largest operating challenges for long-term membrane processes, thus this application would be more far-reaching across several industries (e.g. wastewater, petrochemical, bioprocessing).

Developing ECMs in a HF format presents a significant opportunity for scale-up as HF membranes tend to be preferred in industrial applications for their high packing density. There are further opportunities for optimizing the crossflow deposition process developed herein, such as for an exterior surface coating for outside-in HF membranes. To further improve surface conductivity without sacrificing permeability, we recommend investigating the impacts of using higher quality CNTs in the feed source. Sample CNT options and suppliers are included in Table 5.1; under the optimized flow conditions and concentrations reported herein, manipulating the CNT feed source should allow for independent optimization of surface conductivity.

**Table 5.1.** Carbon nanotube suppliers and purchasing options. The CNTs used in this study are included for reference.

Product	Purity (wt%)	Supplier	Cost (USD, 2020)
SW/DWCNTs COOH (used herein)	>90	Cheap Tubes	\$125/g
SW/DWCNTs 99 COOH	>99	Cheap Tubes	\$300/g
High Purified SWCNTs	98	US Research Nanomaterials, Inc.	\$298/g
P3-SWNT (Purified, high functionality)	>90	Carbon Solutions	\$280/g
Metallic SWNTs	>95	AdNano	\$500/100 mg
Metallic SWCNTs	90	Raymor	\$299/1 mg

The scalability of the crossflow deposition process is limited however as it uses prefabricated HF membranes. HF membranes are typically fabricated via a fiber spinning phase inversion process where a polymer dope and coagulant are co-extruded through a spinneret. The spinneret consists of a central tube and an annular space; the polymer dope is extruded through the annular space while the coagulant flows through the central tube to form the hollow opening [8]. Extension of this process to ECMs, where the CNT conductive layer could be co-extruded with the support HF membrane, would be the best approach for a cost-effective, scalable process. This would require re-design of the standard spinneret, as well as investigation into appropriate chemistries for forming the CNT layer. It is unclear if the PVA stabilization method employed in this work would translate well to a HF spinning process. Cross-linkers can be applied to stabilize the CNT-PVA layer, however forming direct chemical crosslinks with the polymeric support would provide the greatest physical stability.

Finally, design considerations for a full-scale conductive HF membrane module include choice of counter electrode, logistics for connecting the electrochemical circuit, and necessary insulation for safe operation. In Fig. 5.1, we present potential designs for a full-scale HF ECM module in two configurations: a) internal and b) external surface coated HF membranes. The module casing itself would serve as a counter electrode with necessary insulation to prevent discharging with the HF membranes. A wire puncturing the membrane conductive layer would carry charge to the membrane surface. The purpose of these designs is to serve as an initial design point and to present a goal for ultimate HF ECM development.

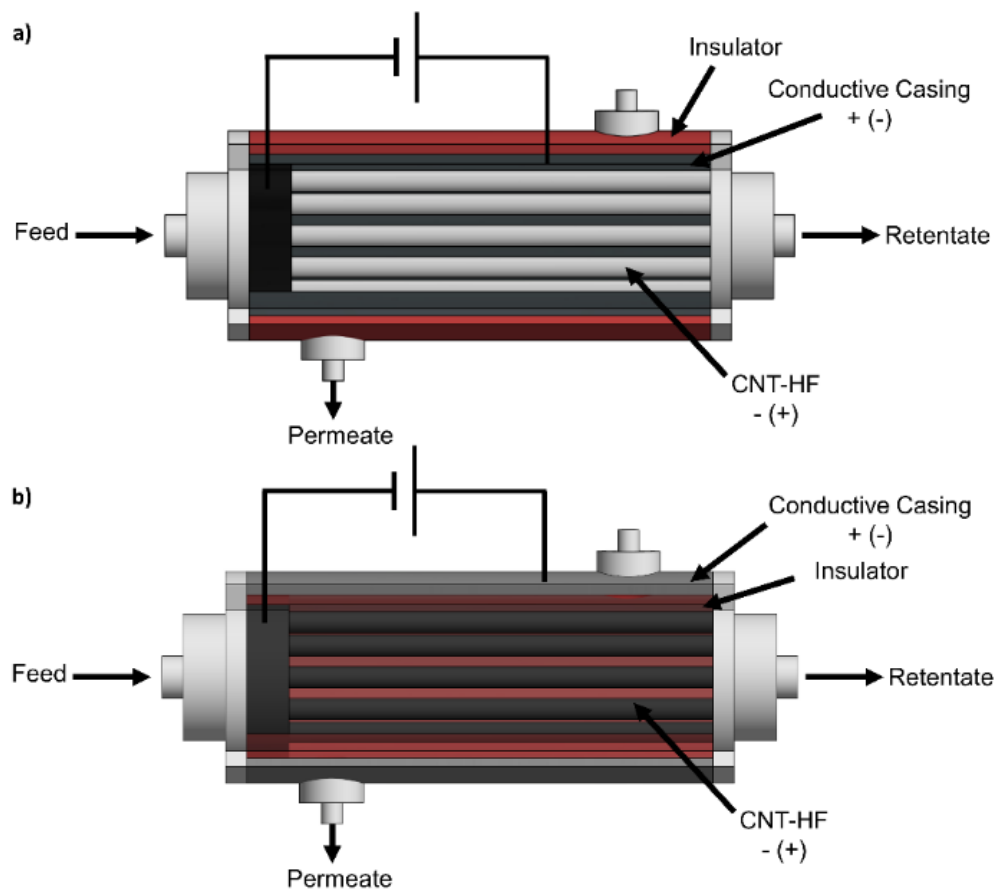


**Figure 5.1.** Proposed conductive hollow fiber membrane module designs for an a) inside-out and b) outside-in hollow fiber configuration.

### 5.3 References

- [1] L.M. Robeson, Correlation of separation factor versus permeability for polymeric membranes, *J. Memb. Sci.* 62 (1991) 165–185. [https://doi.org/10.1016/0376-7388\(91\)80060-J](https://doi.org/10.1016/0376-7388(91)80060-J).
- [2] A.J. Sutherland, M.X. Ruiz-Caldas, C.F. de Lannoy, Electro-catalytic microfiltration membranes electrochemically degrade azo dyes in solution, *J. Memb. Sci.* 611 (2020) 118335. <https://doi.org/10.1016/j.memsci.2020.118335>.
- [3] F.R. Omi, M.R. Choudhury, N. Anwar, A.R. Bakr, M.S. Rahaman, Highly Conductive Ultrafiltration Membrane via Vacuum Filtration Assisted Layer-by-Layer Deposition of Functionalized Carbon Nanotubes, *Ind. Eng. Chem. Res.* 56 (2017) 8474–8484. <https://doi.org/10.1021/acs.iecr.7b00847>.
- [4] C.D. Vecitis, G. Gao, H. Liu, Electrochemical carbon nanotube filter for adsorption, desorption, and oxidation of aqueous dyes and anions, *J. Phys. Chem. C* 115 (2011) 3621–3629. <https://doi.org/10.1021/jp111844j>.
- [5] Y. Liu, J.H. Dustin Lee, Q. Xia, Y. Ma, Y. Yu, L.Y. Lanry Yung, J. Xie, C.N. Ong, C.D. Vecitis, Z. Zhou, A graphene-based electrochemical filter for water purification, *J. Mater. Chem. A* 2 (2014) 16554–16562. <https://doi.org/10.1039/c4ta04006f>.
- [6] S.Y. Yang, C.D. Vecitis, H. Park, Electrocatalytic water treatment using carbon nanotube filters modified with metal oxides, *Environ. Sci. Pollut. Res.* 26 (2019) 1036–1043. <https://doi.org/10.1007/s11356-017-8495-6>.
- [7] C.F. De Lannoy, D. Jassby, K. Gloe, A.D. Gordon, M.R. Wiesner, Aquatic biofouling prevention by electrically charged nanocomposite polymer thin film membranes, *Environ. Sci. Technol.* (2013) 1304–1319.
- [8] T. Matsuura, *Synthetic Membranes and Membrane Separation Processes*, in: *Synth. Membr. Membr. Sep. Process.*, CRC Press, Inc., Boca Raton, 1994: pp. 305–341.

## **Appendix A. Supporting Information**

### **A.1 Impact of Membrane Support Material on Conductive Hollow Fiber**

#### **Membrane Properties**

##### *A.1.1 Introduction*

Preliminary experiments for developing conductive hollow fiber (HF) membranes based on a dead-end carbon nanotube (CNT) deposition technique are summarized in the following section. A systematic comparison was conducted between two types of support membranes: polyether sulfone (PES) and polyvinylidene fluoride (PVDF). Coating success was evaluated based on scanning electron microscopy (SEM) and surface conductivity measurements. The results in this section motivate the crossflow deposition approach developed in Chapter 2.

##### *A.1.2 Experimental*

Two HF support membranes were used: 1) PES “inside-out” membranes from Repligen (0.2  $\mu\text{m}$  pore size, ID: 1 mm, OD: 1.1 mm); 2) PVDF “outside-in” membranes adhered to a polyester support braid from SUEZ Water Technologies (ZeeWeed 500D, 0.04  $\mu\text{m}$  pore size, ID: 0.8 mm, OD: 1.9 mm). PES membranes were supplied dry in an epoxy sealed module with two fibers (length 20 cm, surface area 13  $\text{cm}^2$ ) and were conditioned by filtering DI water as per the manufacturer’s protocol (i.e. 2  $\text{mL}/\text{cm}^2$ ). PVDF membranes were supplied in a glycerin preservative and conditioned by heating in water at 40°C for 3 h, then in 1:10 bleach/ water solution for 3 h at 50°C. PVDF membranes were rinsed and stored in DI water at ambient temperature.

CNT suspensions were prepared similarly to Chapter 2 with the same carboxyl functionalized single walled/double walled CNTs (SW/DWCNTs), and sodium dodecyl sulfate (SDS). Polyvinyl alcohol (PVA, MW: 31,000 – 50,000, 98-99% hydrolyzed) was purchased from

Sigma Aldrich. Briefly, SW/DWCNTs were stirred in DI water for 10 min (600 RPM) then ultrasonicated (QSonica ModelQ500 with a ¼” microtip and 80 µm amplitude) for 1 h with intervals of 2 seconds on/ 2 seconds off (i.e. an effective time of 30 min). SDS was dissolved in DI water by stirring for 30 min (600 RPM) then combined with the sonicated SW/DWCNTs for 15 min (600 RPM) and ultrasonicated for an effective time of 1 h. PVA was dissolved in DI water by stirring for 24 h (800 RPM, 120°C). After cooling to room temperature, the PVA solution was mixed with the CNT/SDS suspension and ultrasonicated for an effective time of 1 h. Suspensions were prepared with 7.5 mg/L SW/DWCNTs, 11.2 mg/L SDS, 75 mg/L PVA.

The active surface of the inside-out PES and outside-in PVDF HF membranes were coated in a dead-end deposition technique. The PVDF HF membranes were sealed in a loop using epoxy (LePage Speed Set Epoxy) and submerged in a 150 mL CNT suspension. Using a PHD multi-rack syringe pump (Harvard Apparatus), vacuum pressure was applied to filter 60 mL of the CNT suspension at 5 mL/min, leaving CNTs deposited on the outer surface (see Fig. A.1a). The membranes were then cured at 100°C for 1 h and stored in DI water at 4°C. The PES HF membranes were left within their module and the syringe pump was used to feed the CNT suspension along the interior surface in dead-end flow at 5 mL/min (see Fig. A.1b). First, 60 mL of CNT suspension was filtered in one direction; then the module was flipped around, and another 60 mL was filtered in the opposite direction. These membranes were cured inside their module for 2.5 h at 100°C and left to dry at ambient temperature over 48 h. The PES HF membranes were removed from the module and stored in DI water at 4°C.

The CNT composite PES and PVDF HF membranes were analyzed using a four-point conductivity measurement technique shown in Fig. A.2. Flat copper alligator clips, spaced 1 cm

apart, were used to contact the active membrane surface. Scanning Electron Microscopy (SEM) analysis was also completed, following the same sample preparation as outlined in Chapter 2.

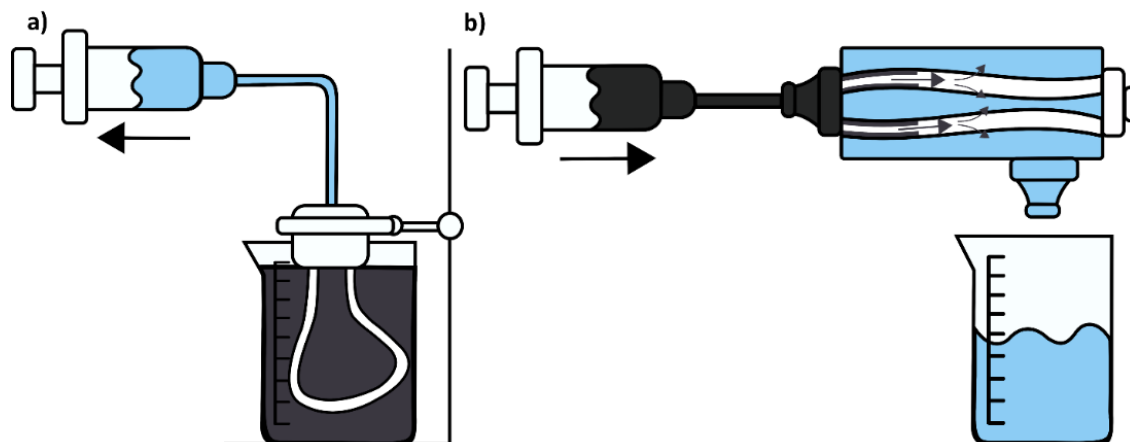


**Figure A.1.** Schematics for dead-end CNT deposition coating experimental set-ups. **a)** Outside-in surface deposition via vacuum filtration **b)** Inside-out surface pressure deposition.

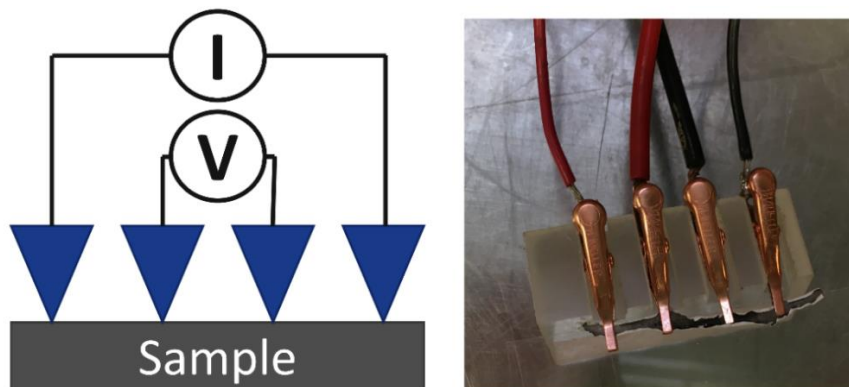


**Figure A.2.** Schematic of the four-probe conductivity test (left) and photo of the copper alligator clip probes in the experimental set-up (right). Clip spacing: 1 cm.

### A.1.3 Results & Discussion

CNT surface deposition was first confirmed visually, as indicated by the dark grey exterior PVDF and interior PES HF membrane surfaces in Fig. A.3. A few random white patches along the surface of the CNT coated PVDF HF membranes are a visual indication of the relatively poor physical stability in comparison to the PES HF membranes. The dark grey deposited layer was confirmed to contain carbon nanotubes under scanning electron microscopy (SEM) for both the PVDF and PES membranes (Fig. A.4). The active surface images (Fig. A.4a, b) showed a random porous network of the fibrous CNT structures. Globular structures, likely representing adhered PVA or SDS molecules, were present on both surfaces as well. In the cross-sectional images (Fig. A.4c, d), the deposited CNTs formed a distinct surface layer on top of the support PVDF and PES polymer membranes. Surface thickness appeared to be greater for the PES membranes but was difficult to estimate at the angle shown. These images indicate successful surface deposition of CNTs both in an outside-in (PVDF HF membranes) and inside-out format (PES HF membranes); however, the interior surface coatings on the PES HF membranes were more physically stable.

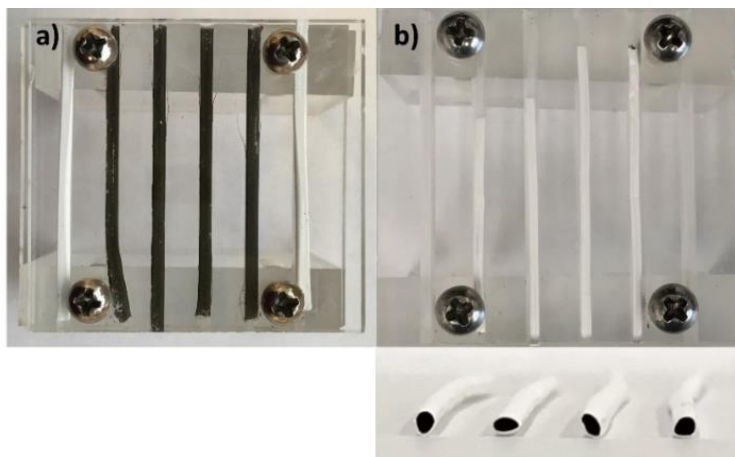


**Figure A.3.** Digital photographs of CNT-coated HF membranes with **a)** outside-in PVDF and **b)** inside-out PES support membranes. Uncoated PVDF membranes shown on the far sides in (a).

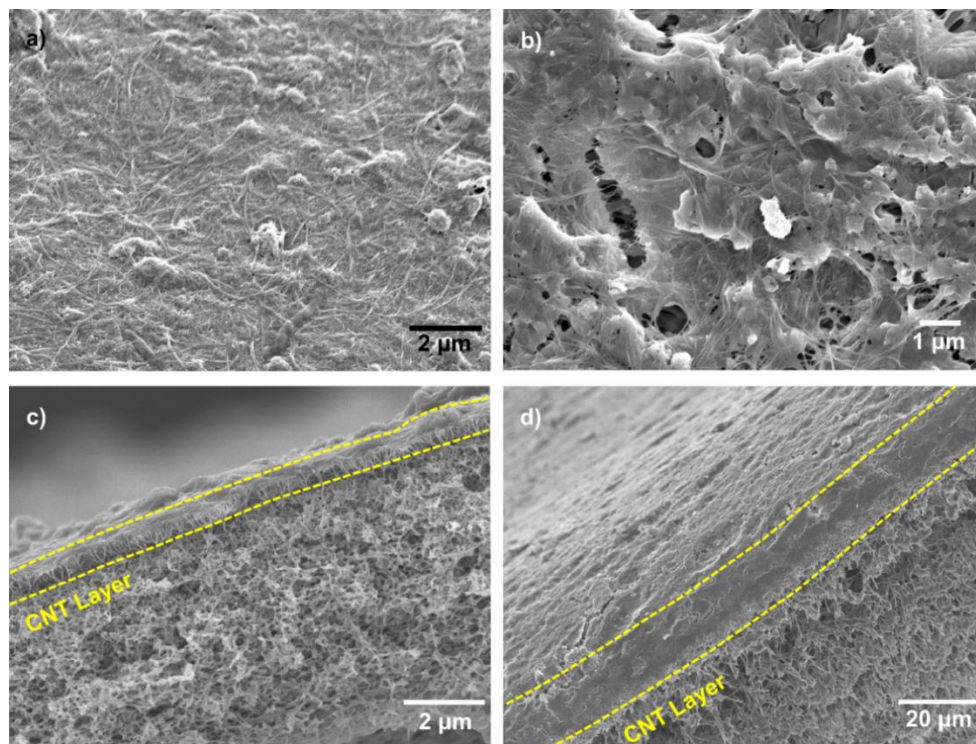


**Figure A.4.** Scanning Electron Microscopy (SEM) images of the CNT-coated PVDF HF membrane exterior surface (a) and in cross-section (c) and of the CNT-coated PES HF membrane interior surface (b) and in cross-section (d).

Surface conductivity measurements confirmed the deposited CNT layer conferred electrical functionality to the membrane surface. Results for several fragments from the PVDF and PES HF membranes are shown in Fig. A.5 in no particular order, normalized for a probe spacing of 1 cm. Average surface conductivity for the CNT-coated PES HF membranes was  $6000 \pm 3700$  S/m, compared to  $655 \pm 164$  S/m for the CNT-coated PVDF HF membranes. This significant increase in conductivity for the PES membranes agreed with the visibly thicker CNT layer in the cross-sectional SEM images (Fig. A.4c, d). However, the PES HF membranes had a larger range of error than the PVDF membranes. We suspect this was due to non-uniformity in the coating layer; variation in degree of deposition along the fiber length would affect the measured surface conductivities. This was the prime motivation for studying a crossflow deposition technique – in dead-end deposition, there is a large pressure gradient from inlet to outlet along the fiber. In crossflow filtration, we hypothesized pressure could be modulated to control coating uniformity.

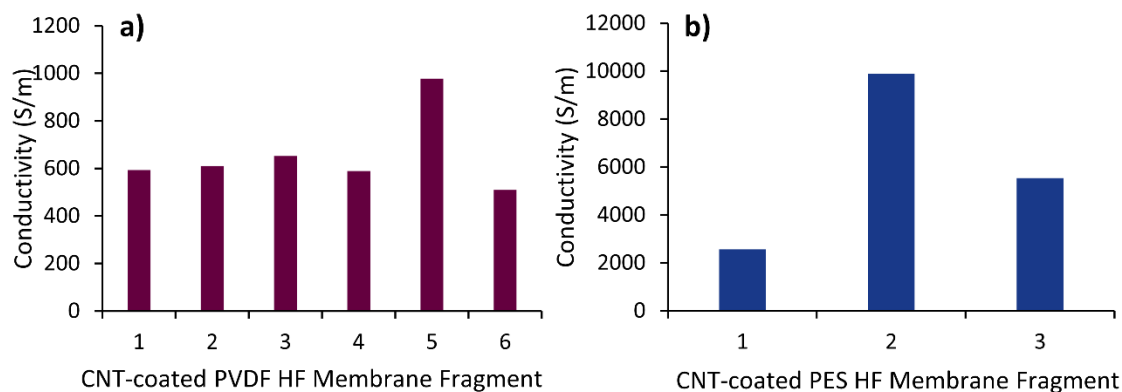


**Figure A.5.** Surface conductivity measurements for the **a)** exterior surface of CNT-coated PVDF HF membranes and **b)** interior surface of CNT-coated PES HF membranes.

Several modifications to the CNT suspension protocol were made prior to the experiments in Chapter 2. Firstly, the PVA molecular weight was decreased from 31-50 kDa to 13-23 kDa to facilitate dissolution of PVA in water, reducing the time for this step from 24 h to 30 min. Secondly, sonication times were reduced to the following effective times: SW/DWCNTs 15 min, CNT/SDS 30 min, CNT/SDS/PVA 15 min, as this was found to have no significant qualitative impact on dispersibility.

#### A.1.4 Conclusions

Conductive CNT-coated HF membranes were fabricated using PVDF outside-in and PES inside-out support membranes in a dead-end deposition technique. While high surface conductivities were measured for each type of membrane (PVDF: ~600 S/m, PES: ~6000 S/m), significant variation was detected along the length of the fibers, especially for the CNT-coated PES HF membranes. Additionally, the CNT-coated PVDF HF membranes had relatively poor physical stability and were deemed infeasible for further experimentation. Crossflow deposition was proposed as a potential solution to the observed lack of uniformity in the CNT-coated PES HF membranes and is explored in detail in Chapter 2.

## **A.2 Challenges with establishing a metric to quantify carbon nanotube deposition**

### *A.2.1 Introduction*

In the crossflow deposition process in Chapter 2, it is difficult to estimate the mass of carbon nanotubes (CNTs) deposited on the hollow fiber (HF) membranes as not all of the CNTs in the feed will end up in the membrane composite. To have a clear understanding of how crossflow parameters affect deposition, it is important to use a reliable and accurate technique for measuring this deposited mass. Quantification of CNTs in environmental matrices is a growing field; however, there is currently no standard technique [1]. We evaluated the applicability of several methods used in previous works [1] in both aqueous (e.g. total organic carbon (TOC), UV-Vis-NIR) and solid (e.g. thermogravimetric analysis) matrices. Aqueous techniques measured CNT concentration in suspension while solid techniques measured CNT mass directly from a membrane sample. Surface conductivity was also evaluated as a surrogate metric for estimating CNT mass.

### *A.2.2 Total Organic Carbon*

CNT suspensions, prepared using the protocol in Section A.1 with sequential addition and sonication of CNTs, sodium dodecyl sulfate (SDS), and polyvinyl alcohol (PVA), were analyzed using a TOC-L total organic carbon (TOC) analyzer (Shimadzu) and correlated to a known concentration. Samples were analyzed in 9 mL glass test tubes, filled with 8 mL of sample. As the TOC analyzer uses a non-specific combustion catalytic oxidation method, all sources of carbon in the liquid sample would be detected, including both CNTs and PVA in these suspensions. To avoid interference from PVA, the standard CNT suspensions prepared for calibration were diluted in a solution of 11.2 mg/L SDS and 75 mg/L PVA in DI water, the same concentrations used for preparing the initial concentrated sample from which the dilution series was derived (7.5 mg/L CNTs to match the feed concentration in the crossflow deposition experiments).

The dilution series was completed twice, giving two consistent linear trends in the resulting calibration curve (see Fig. A.6). Two key limitations with this approach were the shallow slope covering a range of ~100 units on the TOC analyzer and the poor resolution in the lower concentration range (< 1 mg/L). The shallow slope means a large change in CNT concentration could correspond to a relatively small change in signal from the TOC, therefore small changes in CNT concentration may not be detected. As the CNTs are much larger than the membrane pore size, permeate samples were expected to have very low CNT concentrations, thus the low resolution in this range would give poor confidence whether CNTs were truly absent in the permeate samples. The points for the three lowest concentrations (0.23, 0.12, 0.06 mg/L) were excluded from the linear regression models due to this poor resolution.

The accuracy of these calibration curves in predicting CNT mass deposited were demonstrated for three dead-end coating procedures for the PVDF HF membranes described in Section A.1. Three different initial suspension concentrations were studied: 7.5 mg/L, 3.8 mg/L and 1.9 mg/L; all were prepared with 1:1.5 CNT:SDS and 1:10 CNT:PVA ratios by mass. CNT concentrations estimated by the calibration curve in Fig. A.6 (parameters from Model #2) for the initial, final, and permeate samples are included in Fig. A.7 along with a control of a 75 mg/L PVA and 11.2 mg/L SDS solution in DI water. No significant difference was detected between the initial and final concentrations as expected. However, permeate sample CNT concentrations were much higher than expected. In the CNT concentration ranges reported, the permeate should have had a visible dark grey colour; however, these solutions had no visible CNTs. We suspect potential interference from the PVA as it is likely PVA was filtered into the permeate while the CNTs were captured on the membrane surface.

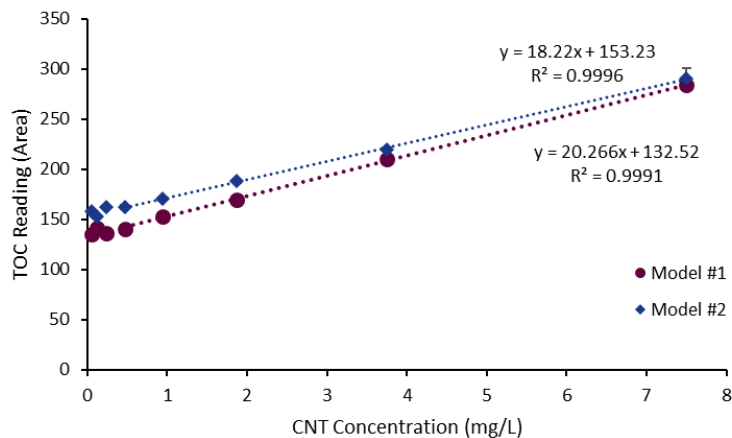


**Figure A.6.** Calibration curve relating total organic carbon (TOC) reading to known carbon nanotube (CNT) concentrations. Same dilution series was created twice to generate two models.

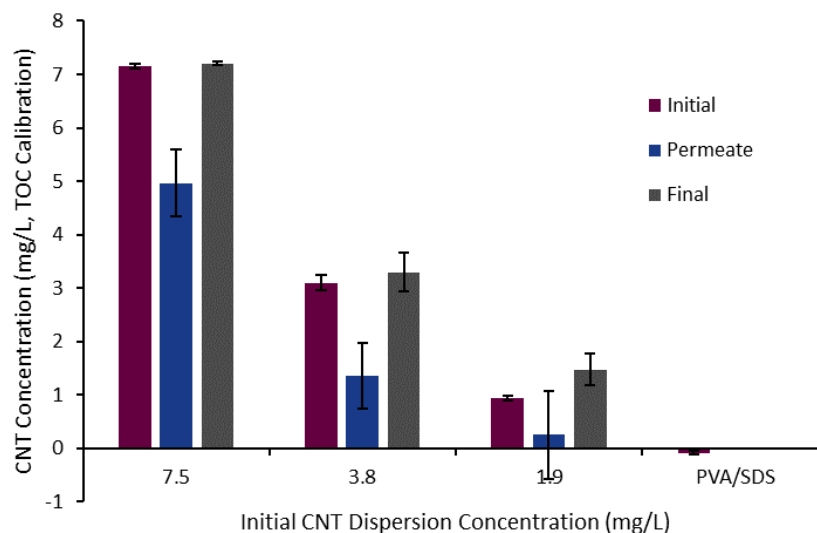


**Figure A.7.** CNT concentrations measured via TOC measurement (calibration parameters from Model #2) for the initial, final and permeate samples collected during dead-end deposition onto the PVDF HF support membranes.

### A.2.3 UV-Vis-NIR Spectroscopy

CNT suspensions were prepared according to the protocol in Section A.1 and analyzed using a UV-Vis-NIR spectrophotometer (Cary 5000). Samples were analyzed in 10 mm quartz cuvettes in dual beam mode. Two types of suspensions were prepared: 1) CNTs dispersed with SDS in a 1:1.5 mass ratio in DI water; 2) CNTs dispersed with SDS and PVA in a 1:1.5 CNT:SDS and 1:10 CNT:PVA mass ratio in DI water. These two types of suspensions were prepared at three CNT concentration levels: 75, 7.5 and 0.75 mg/L.

The absorbance spectra for these suspensions are included in Fig. A.8 with (a) representing the CNT/SDS suspensions and (b) representing the CNT/SDS/PVA suspensions. The absorbance values measured for both the CNT/SDS and CNT/SDS/PVA suspensions were similar in magnitude, which indicates that PVA was not a significant interferent. For all spectra, the maximum absorbance occurred  $\sim 260$  nm. Although previous works have reported peaks for CNT absorbance in a similar wavelength range [2], these peaks have been attributed to non-CNT impurities in the suspension such as ash [3]. Apart from this peak, the remainder of the spectra show a featureless curve with some noise in the lowest CNT concentration curves that can partially be attributed to aperture shift between wavelength ranges ( $\sim 800$  nm). Purified, pristine SW/DWCNTs typically produce a spectrum with more characteristic features, notably a peak in the  $\sim 1000$  nm range [3][4]. Several factors can cause these features to be diminished, specifically presence of impurities [4] and surface functionalization [5]. The SW/DWCNTs used in this work were susceptible to both challenges due to their carboxyl functionalization and impurities.

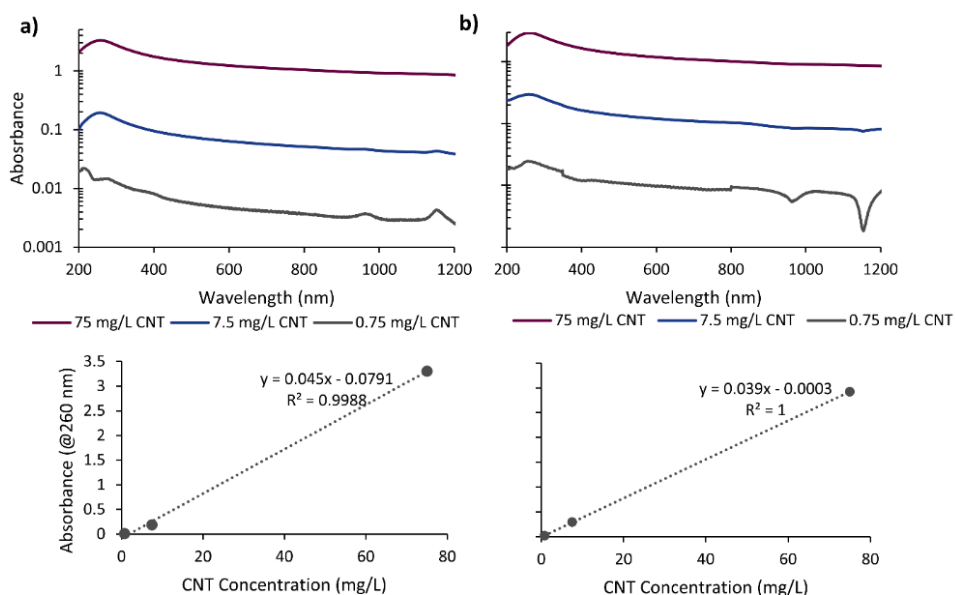


**Figure A.8.** UV-Vis-NIR spectra (top row) and calibration with CNT concentration at 260 nm (bottom row) for two types of CNT suspensions: **a)** CNTs and SDS dispersed in a 1:1.5 mass ratio in DI water; **b)** CNTs, SDS and PVA dispersed in a 1:1.5 CNT:SDS and 1:10 CNT:PVA mass ratio in DI water. Reported absorbances have been normalized by subtracting the absorbance of a sample of DI water.

Despite the lack of characteristic features in the UV-Vis-NIR spectra, we fit a linear calibration curve to relate the absorbance at 260 nm to CNT concentration (see Fig. A.8). Previous works have developed calibration curves based on absorbance in this range [2]. More data points are needed to ensure accuracy of this calibration curve. Additionally, accuracy was poor in the low CNT concentration range relevant to this study ( $< 7.5$  mg/L) due to the low absorbance values.

#### A.2.4 Thermogravimetric Analysis

Powder and membrane samples were analyzed using a thermogravimetric analyzer (Mettler Toledo TGA-DSC 3+). Samples were loaded into a 70  $\mu$ L alumina crucible and heated using the following protocol: heat from 25 to 100°C at 5°C/min, hold at 100°C for 5 min to remove residual water, then heat from 100°C to 1000°C at 10°C/min. Powder samples included the single walled/double walled carbon nanotubes (SW/DWCNTs), polyvinyl alcohol (PVA), and sodium dodecyl sulfate (SDS) used to fabricate the CNT-coated HF membranes. Membrane samples included PES HF membranes (0.2  $\mu$ m pore size; ID: 1 mm; OD: 1.1 mm) from Repligen as well as flat sheet PES membranes (0.03  $\mu$ m pore size) from Sterlitech. The protocol for fabricating CNT-coated flat sheet membranes has been developed previously [6]. Briefly, the CNT/SDS/PVA suspensions were prepared according to the protocol in Section A.1 at a concentration of 75 mg/L CNTs (with 1:1.5 CNT:SDS and 1:10 CNT:PVA by mass). PES flat sheet membranes were cut into 3.5 cm discs and soaked in DI water for 24 h. A wetted PES membrane was placed in a glass flask and a certain volume of CNT suspension was vacuum filtered onto the membrane surface to achieve the following deposited CNT masses: 1.5, 0.15, 0.015 mg. A control membrane was prepared via vacuum filtration of 20 mL of a PVA/SDS solution (no CNTs; same volume as 1.5 mg coating). CNT-coated flat sheet membranes were then cured for 1 h at 100°C. For TGA measurements, a ¼” disc was cut out of the flat sheet membrane samples using a hole punch.

Each of the material components in the CNT-coated PES HF membranes was first analyzed to determine the feasibility of this technique for estimating CNT mass. Results shown in Fig. A.9a indicate significant degradation of PVA, SDS and the PES HF membranes while CNT mass remained largely unchanged beyond an initial drop to ~85% around 100°C. Typical TGA thermographs for CNTs show a similar result with minimal change in mass when heated up to 600°C [7]. The decrease at the beginning could be due to evaporation of remaining moisture in the sample and could be mitigated by incorporating a pre-drying step. The thermographs for SDS and PVA were generally in agreement with accepted literature in terms of inflection point (~200°C for SDS; ~300°C for PVA) and the characteristic local peak ~400°C for PVA [8][9]. The PES HF membrane sample also behaved as expected with an inflection point ~550°C [10]. The small decrease observed ~200°C for the PES HF membrane samples was likely due to glass transition at 220°C [11]. In these experiments, TGA showed promise as a CNT quantification technique as the polymer and surfactant in the composite membranes could be degraded, leaving behind the CNTs.

TGA applicability was further tested using a series of PES flat sheet membranes coated with known masses of CNTs. Thermographs for the unmodified PES flat sheet membranes, as well as the PES membranes coated with PVA/SDS solution and three known masses of CNTs are shown in Fig. A.9b. The unmodified PES membrane behaved similarly to the PES membrane coated with PVA/SDS solution and the final masses for both were well below that of the CNT-coated membranes. This was expected as the control experiments indicated only PVA, SDS and PES should degrade. However, these two control samples showed a similar decrease to ~85% around 100°C that was observed with the CNT powder in Fig. A.9a. This may also be attributed to moisture present in the sample but is an interesting finding as in all three cases, the weight lost was roughly the same. The thermographs for the CNT-coated membranes at 1.5 and 0.15 mg were

indistinguishable from each other above 600°C, although the 0.015 mg CNT membrane appeared to fall somewhere between these higher masses and the controls. This experiment was repeated with another set of three CNT-coated HF membranes (not shown) giving the following ranges for the final mass percentage: 40-41% for 1.5 mg CNT, 40-43% for 0.15 mg CNT, 37-41% for 0.015 mg CNT. The significant overlap in final mass percentage indicates the infeasibility of this technique for measuring the mass of CNTs present.

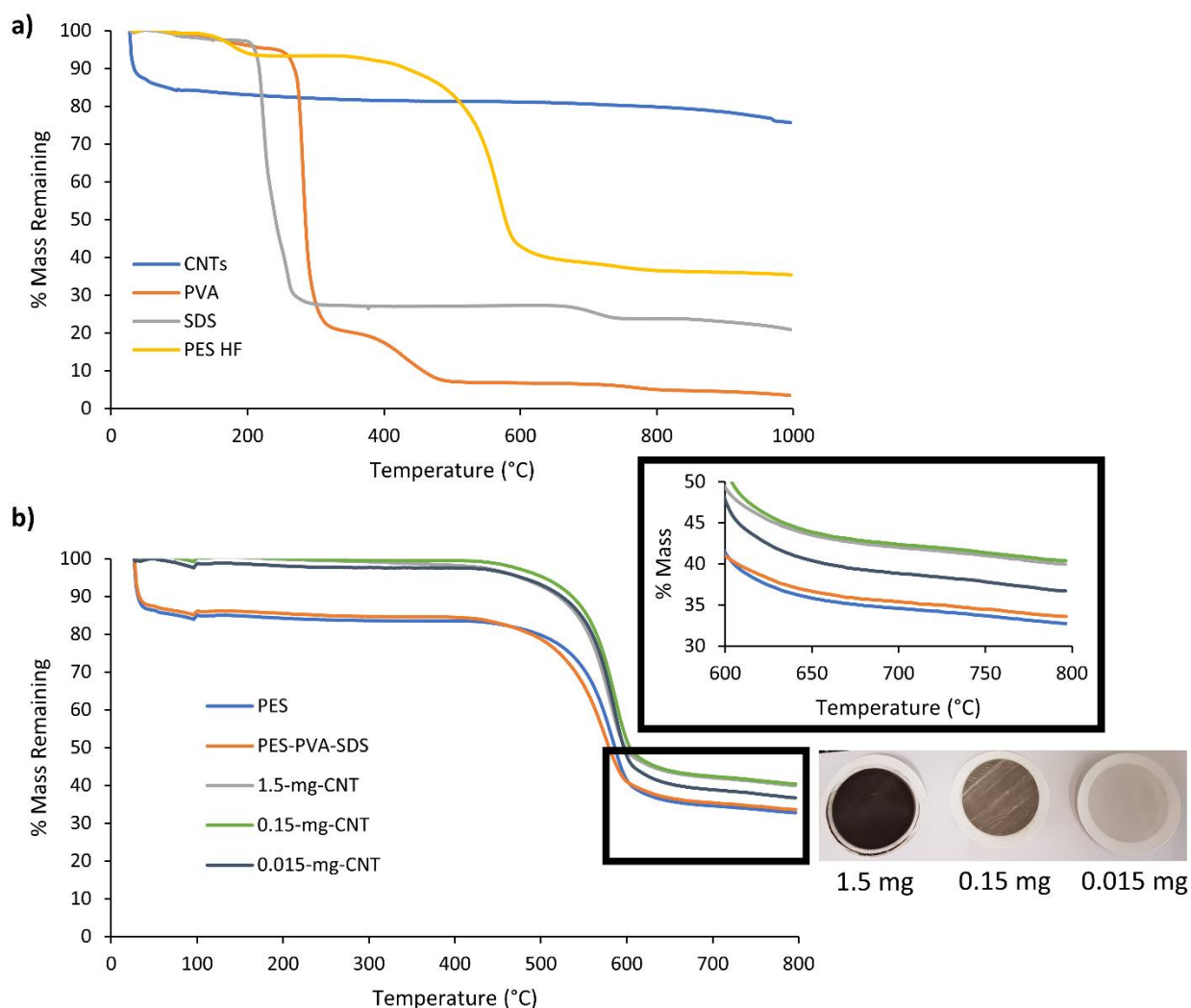


**Figure A.9.** TGA thermographs for **a)** powdered CNT, PVA and SDS samples as well as the Repligen PES HF membrane and **b)** PES flat sheet membrane control and coated with PVA/SDS solution as well as three masses of CNTs: 1.5, 0.15, 0.015 mg. Inset shows weight percentages towards the end of the heating process. Photograph inset shows PES flat sheet membranes coated with the three masses of CNTs.

### A.2.5 *Surface Conductivity Correlation*

Surface conductivity was used as a surrogate metric to estimate CNT mass deposited on the composite membranes. CNT-coated PES flat sheet membranes were prepared in the same manner outlined in Section A.2.4 for a final deposited mass of 3, 1.5, 0.5, 0.15, 0.015, 0.0015 mg. Each membrane was prepared in duplicate. Surface conductivity was measured using the four-point probe technique (Ossila T2001A3) outlined in Chapter 2.

A calibration curve was created to relate the measured surface conductivity to the mass deposited shown in Fig. A.10. To calculate surface conductivity, a thin film layer thickness of 1  $\mu\text{m}$  was assumed. No current was detected for the lowest mass deposited (0.0015 mg) and was therefore excluded from the calibration curve. The curve was linear in shape, confirmed by randomness in model residuals. Model resolution was good between 0.015 to 3 mg, with masses distinguishable from each other within error. The error ranges were not insignificant however, particularly at 0.5 mg ( $\sim 0.14 \text{ mg/cm}^2$ ) with a standard deviation of 740 S/m between two membrane samples. This technique is limited as surface conductivity is not dependent on CNT mass alone; CNT density, curing time, cross-linkers and the ratios of surfactant and polymer in the suspension could have a significant impact [6][12]. Additionally, the “known” mass of CNTs was based on the CNT “powder” from the supplier which also contained impurities such as ash. This technique shows promise if the same membrane fabrication protocol is followed for developing the calibration curve as with running the experiments and if higher purity CNTs are used.

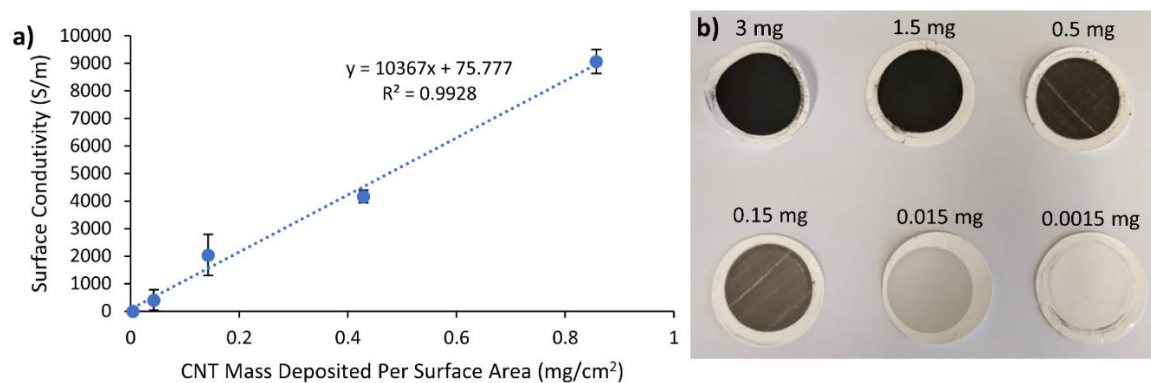


**Figure A.10.** a) Calibration curve relating surface conductivity measurements to known CNT masses deposited on the surface of PES flat sheet membranes. Error bars represent the standard deviation between two membrane samples. b) Photographs of the CNT-coated flat sheet membranes used to generate the calibration curve.

### A.2.6 Conclusions

Several CNT quantification techniques were evaluated for their accuracy in aqueous and solid matrices. CNT suspensions were analyzed via total organic carbon (TOC) and UV-Vis-NIR spectroscopy. TOC readings were linearly correlated with CNT concentration; however, resolution was limited by interference from polyvinyl alcohol (PVA). The UV-Vis-NIR spectra were featureless curves with one prominent peak  $\sim 260$  nm; the lack of characteristic features was indicative of the functionalized, impure nature of the CNTs. Solid membrane samples were analyzed via thermogravimetric analysis (TGA). Although the control experiments indicated potential usefulness of TGA due to CNT thermal stability, this method was not able to distinguish between a three-order of magnitude difference in CNT mass deposited on PES flat sheet membranes. As a surrogate measurement, surface conductivity was linearly correlated with CNT mass, resulting in masses distinguishable as low as 0.015 mg. This analysis demonstrates the need for a standardized method of CNT quantification. Many techniques, such as TGA and UV-Vis-NIR, are limited in their applicability for only pure, non-functionalized CNTs. As applications for functionalized CNTs become more widespread, such as for developing electrically conductive membranes, surrogate techniques (e.g. surface conductivity) may be of significant interest.

### A.3 References

- [1] E.J. Petersen, D.X. Flores-Cervantes, T.D. Bucheli, L.C.C. Elliott, J.A. Fagan, A. Gogos, S. Hanna, R. Kägi, E. Mansfield, A.R.M. Bustos, D.L. Plata, V. Reipa, P. Westerhoff, M.R. Winchester, Quantification of Carbon Nanotubes in Environmental Matrices: Current Capabilities, Case Studies, and Future Prospects, *Environ. Sci. Technol.* 50 (2016) 4587–4605. <https://doi.org/10.1021/acs.est.5b05647>.
- [2] Y. Shi, L. Ren, D. Li, H. Gao, B. Yang, Optimization Conditions for Single-Walled Carbon Nanotubes Dispersion, *J. Surf. Eng. Mater. Adv. Technol.* 03 (2013) 6–12. <https://doi.org/10.4236/jsemat.2013.31002>.
- [3] X. Huang, R.S. Mclean, M. Zheng, High-resolution length sorting and purification of DNA-wrapped carbon nanotubes by size-exclusion chromatography, *Anal. Chem.* 77 (2005) 6225–6228. <https://doi.org/10.1021/ac0508954>.
- [4] A.G. Ryabenko, T. V. Dorofeeva, G.I. Zvereva, UV-VIS-NIR spectroscopy study of sensitivity of single-wall carbon nanotubes to chemical processing and Van-der-Waals SWNT/SWNT interaction. Verification of the SWNT content measurements by absorption spectroscopy, *Carbon N. Y.* 42 (2004) 1523–1535. <https://doi.org/10.1016/j.carbon.2004.02.005>.
- [5] S. Goyanes, G.R. Rubiolo, A. Salazar, A. Jimeno, M.A. Corcuera, I. Mondragon, Carboxylation treatment of multiwalled carbon nanotubes monitored by infrared and ultraviolet spectroscopies and scanning probe microscopy, *Diam. Relat. Mater.* 16 (2007) 412–417. <https://doi.org/10.1016/j.diamond.2006.08.021>.
- [6] M.A. Halali, C.F. De Lannoy, The Effect of Cross-Linkers on the Permeability of Electrically Conductive Membranes, *Ind. Eng. Chem. Res.* 58 (2019) 3832–3844. <https://doi.org/10.1021/acs.iecr.8b05691>.
- [7] D. Fong, G.M. Andrews, A. Adronov, Preparation of stimulus-responsive, polyfluorene-wrapped carbon nanotubes via palladium cross coupling, *J. Polym. Sci. Part A Polym. Chem.* 56 (2018) 2723–2729. <https://doi.org/10.1002/pola.29256>.
- [8] H.K.F. Cheng, Y. Pan, N.G. Sahoo, K. Chong, L. Li, S.H. Chan, J. Zhao, Improvement in Properties of Multiwalled Carbon Nanotube/Polypropylene Nanocomposites Through Homogeneous Dispersion with the Aid of Surfactants Henry, *J. Appl. Polym. Sci.* 124 (2012) 1117–1127. <https://doi.org/10.1002/app>.
- [9] B.M.S.P. Shaffer, A.H. Windle, Fabrication and Characterization of Carbon Nanotube / Poly ( vinyl alcohol ) Composites \*\*, (1999) 937–941.
- [10] N. Ghaemi, S.S. Madaeni, A. Alizadeh, H. Rajabi, P. Daraei, Preparation, characterization and performance of polyethersulfone/organically modified montmorillonite nanocomposite membranes in removal of pesticides, *J. Memb. Sci.* 382 (2011) 135–147. <https://doi.org/10.1016/j.memsci.2011.08.004>.
- [11] N. Juangvanich, K.A. Mauritz, Polyethersulfone-[silicon oxide] hybrid materials via in Situ sol-gel reactions for tetra-alkoxysilanes, *J. Appl. Polym. Sci.* 67 (1998) 1799–1810. [https://doi.org/10.1002/\(sici\)1097-4628\(19980307\)67:10<1799::aid-app13>3.0.co;2-s](https://doi.org/10.1002/(sici)1097-4628(19980307)67:10<1799::aid-app13>3.0.co;2-s).
- [12] C.F. de Lannoy, D. Jassby, D.D. Davis, M.R. Wiesner, A highly electrically conductive polymer-multiwalled carbon nanotube nanocomposite membrane, *J. Memb. Sci.* 415–416 (2012) 718–724. <https://doi.org/10.1016/j.memsci.2012.05.061>.